NASA Contractor Report 195033
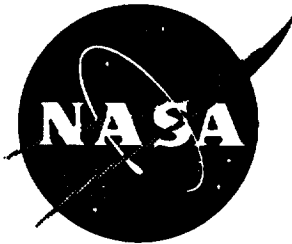
Experimental Study of the Effects of Reynolds Number on High Angle of Attack Aerodynamic Characteristics of Forebodies During Rotary Motion

H. Pauley, J. Ralston, and E. Dickes
Bihrle Applied Research, Hampton, Virginia

Contract NAS1-20228
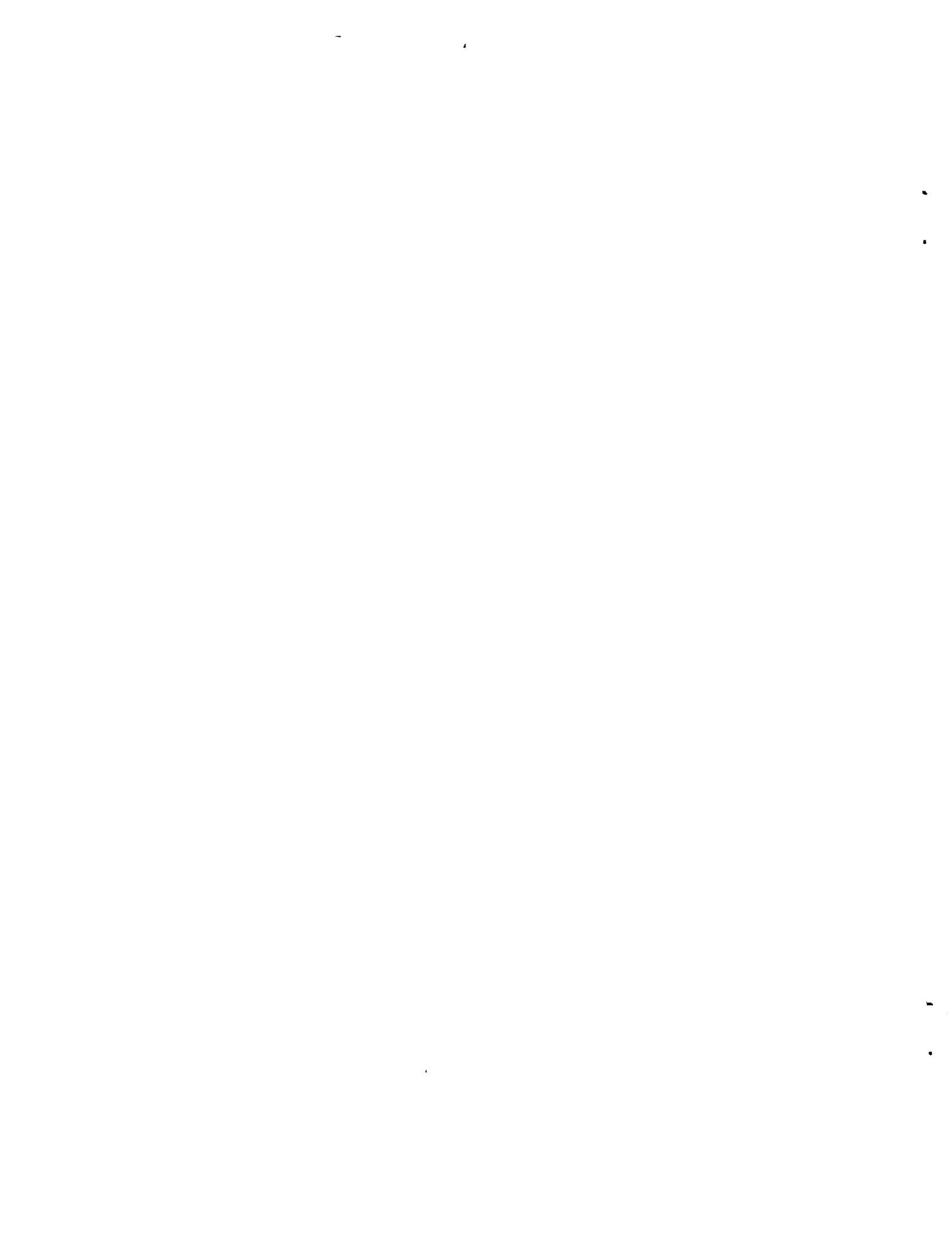
January 1995

N95-24443

Unclas

G3/02   0046008

(NASA-CR-195033) EXPERIMENTAL STUDY OF THE EFFECTS OF REYNOLDS NUMBER ON HIGH ANGLE OF ATTACK AERODYNAMIC CHARACTERISTICS OF FOREBODIES DURING ROTARY MOTION Final Report (Bihrle Applied Research) 97 p

ABSTRACT

The National Aeronautics and Space Administration in the United States and the Defense Research Agency in the United Kingdom have ongoing experimental research programs in rotary-flow aerodynamics. A cooperative effort between the two agencies is currently underway to collect an extensive database for the development of high angle of attack computational methods to predict the effect of Reynolds number on the forebody flowfield at dynamic conditions, as well as to study the use of low Reynolds number data for the evaluation of high Reynolds number characteristics. Rotary balance experiments, including force and moment and surface pressure measurements, were conducted on circular and rectangular aftbodies with hemispherical and ogive noses at the Bedford and Farnborough wind tunnel facilities in the United Kingdom. The bodies were tested at 60° and 90° angle of attack for a wide range of Reynolds numbers in order to observe the effects of laminar, transitional, and turbulent flow separation on the forebody characteristics when rolling about the velocity vector.

NOMENCLATURE

Symbols

The units for physical quantities used herein are presented in U.S. Customary Units with S.I. Units given in parentheses. All aerodynamic data are referenced to the body system of axes.

A_{ref}	reference area, πr_b^2, ft^2 (m^2)
b	reference body length, ft (m)
D	reference base diameter, ft (m)
C_Y	side-force coefficient, Side force/ $q_\infty A_{ref}$
C_n	body-axis yawing-moment coefficient, Yawing moment/ $q_\infty A_{ref} D$
C_p	pressure coefficient, $(p-p_\infty)/q_\infty$
p	pressure on model surface, lb/ft^2 (N/m^2)
p_∞	free-stream static pressure, lb/ft^2 (N/m^2)
q_∞	free-stream dynamic pressure, lb/ft^2 (N/m^2)
r_b	radius at the base of the body, ft (m)
Re_D	Reynolds number, based on body diameter, VD/ν
V	free-stream velocity, ft/sec (m/sec)
x	axial distance from the nose tip, ft (m)
α	angle of attack, deg
Ω	angular velocity about spin axis, rad/sec
$\Omega b/2V$	spin coefficient, positive for clockwise spin
ν	kinematic viscosity, ft^2/s (m^2/s)
Θ	azimuth angle around forebody cross-section, deg

INTRODUCTION

Recent tactical evaluations demonstrating the enhanced high angle of attack performance and nose-pointing agility with a number of U.S. and Russian military configurations have shown the utility of post-stall, velocity vector maneuvering. The relative interest in this technology has been stimulated by the introduction of these highly agile military aircraft which possess a substantially expanded flight envelope compared to previous aircraft. These advanced aircraft maneuver at high angles of attack, performing rapid, large-amplitude motions which are characterized by rotary, non-linear, and unsteady flows. Hence, an increased knowledge of aerodynamic characteristics at high angles of attack under dynamic conditions is now necessary for the successful design optimization of future fighter aircraft and has put a new emphasis on the use of rotary balance data in the analysis of these flight regimes.[1-4]

The quantification of the aerodynamic characteristics obtained at high angles of attack under dynamic conditions takes on increasing importance as emerging aircraft will continue to exploit this flight regime. This extends beyond a configuration's developmental evaluation of the damping terms to the incorporation of these terms in large-angle motion simulations. Accurate simulation representation permits the optimization of high angle of attack flight control laws as well as the exploration of a configuration's flight characteristics in a benign simulation environment. In addition to obtaining the aerodynamic force and moment coefficients for these dynamic motions, new vortex control applications also require familiarity with the flow in the form of flow visualization experiments and pressure measurements [5, 6] in order to fully understand and utilize the flow fields that develop under these conditions.

The flow about forebody geometries typical of most military aircraft at high angles of attack is highly complex. The results of previous research on fuselage-type forebodies at static test conditions showed that throughout much of the angle of attack

4

range, the flow is governed by separation-induced vortex flows. Studies of ogive-cylinder bodies have shown that at low angles of attack ($\alpha < 8^o$), as long as the flow remains attached, no vortices develop on the body. At moderate angles, ($\alpha < 25^o$) an adverse crossflow pressure gradient on the downwind side of the body causes the boundary layer to separate and roll up to form two symmetric vortices. The separation lines move toward the upwind side of the body with increasing angle of attack until the vortices completely dominate the flow over the leeward side. From between 25° to 40°, (depending on the configuration), the steady, symmetric vortices begin shedding asymmetrically and randomly. As the angle approaches 90° there is a transition to an unsteady wake-type flow resembling Karman vortex streets.[7,8] These vortex "streets" are characteristic of the regular pattern of counter-rotating vortices that occur on 2-D cylinders normal to the flow.

The research conducted to date has shown that in static conditions the forebody flow characteristics are influenced by factors such as forebody cross section, nose geometry and local Reynolds number. However, basic configurational data relating the effects of these physical characteristics during a velocity vector roll rate has been lacking.

Both the National Aeronautics and Space Administration (NASA) in the United States and the Defense Research Agency (DRA) in the United Kingdom have on-going experimental research programs in rotary-flow aerodynamics. A five-year cooperative effort is currently underway to further studies on this subject.

The objectives of this collaboration between NASA and DRA are as follows:
- To explore and develop computational fluid dynamics (CFD) methods for predicting Reynolds number effects on aircraft fuselage spin-damping characteristics.

- To conduct systematic wind-tunnel, rotary balance experiments and CFD calculations on a series of simple, generic bodies.

- To compare experimental and calculated results to assess/calibrate CFD methods.

This report describes the experiments conducted and an analysis of these data, presenting aerodynamic data and surface pressures for these generic bodies at high angle of attack as a function of Reynolds number and rotation from the first two wind-tunnel test entries.

EXPERIMENTAL SETUP

Test Facilities

Wind tunnel tests were conducted in the low-speed atmospheric wind tunnel (13 ft x 9 ft) at Bedford and in the high speed pressurized tunnel (8 ft x 6 ft) at Farnborough, utilizing the Defense Research Agency rotary balance apparatus. The Bedford and Farnborough facilities provided a Mach number range of 0.024 to 0.21 and a Reynolds number capability of 0.15 to 4.5 million per foot for these tests. Pressures of 0.5 to 3 atmospheres were achieved in the variable-pressure facility. A diagram of the rotary balance apparatus in the low-speed tunnel at Bedford is shown in Figure 1. A five-component strain gauge balance (axial force excluded) was attached to the end of the sting, which was then attached to the sting carrier. The carrier traversed along the machined steel rotor to vary angle of attack in one degree increments. The angle of attack could be varied between -12° and 90° with various sting carriers. When the angle of attack was set, the carrier was secured to the rotor with clamping bolts normal to the plane of the rotor and screwed wedges in the plane of the rotor. Weight carriers were bolted to the ends of the rotor, and a selection of weights were fixed to either carrier to

maintain static balance. A covered channel in the rotor accommodated the cable from the strain gauge balance and pressure transducers. Rotational speed, usually limited to 350 rpm, was controlled by a servo valve with feedback from a tachogenerator geared to the drive shaft. When testing at high air speeds and/or high air density, rotation speed was limited by damping loads on the rotating assembly which reach the limit of torque available from the hydraulic motor. Strain gauge balance and pressure measurement signals were brought out by a cable through a bore hole in the drive shaft and a slipring unit at the motor end of the shaft.

Models

The model shapes selected for these tests were circular and rectangular aftbodies, with detachable hemispherical and 2.0D ogive forebodies. A photograph of the rectangular ogive model installed on the rotary balance apparatus in the low-speed tunnel is shown in Figure 2. The models were tapped with six circumferential rows of taps on the forebody and two on the aftbody, as shown in Figure 3. All models were 36 inches long, with a diameter of 6 inches. Station zero represented the tip of the forebody, station 12 the forebody breaking point, and station 36 the overall length. Taps were located at stations 1, 2, 4, 6, 8, 11, 29, and 32.5. The total number of surface pressure ports was 254 for each configuration. There were 32 pressure taps at each body station except station 1, which only accommodated 30 taps. Trip strips and strakes were tested on the circular ogive configuration at 60 degrees angle of attack. A sketch of these devices is shown in Figure 4. The trip strips were narrow thin pieces of metal with small, raised holes punched in them. One strip was attached on each side of the nose of the circular ogive model, 80 degrees from the bottom centerline, and extended down the sides until about 3 inches from the aft end. The strakes were thin pieces of metal mounted perpendicular to

the model surface on either side of the nose, approximately 0.5 inches wide by 4 inches long and placed 135° from the bottom centerline.

Test Conditions

The tests were conducted over a range of Reynolds numbers (based on diameter) from about 0.08 to 2.25 million, a Mach number range of 0.024 to 0.21, and at angles of attack of 60 and 90 degrees. The rotation rate varied from 0.0 to 0.4 $\Omega b/2V$ in both positive (clockwise) and negative (counter-clockwise) directions. Pressure data were taken concurrently with force and moment data during each run. Due to data acquisition problems, surface pressures were not obtained on the aft end of some of the configurations tested at the Bedford facility. A summary of the configurations tested and test conditions is presented in Table 1.

Data Processing/Reduction/Accuracy

When the model is rotated at constant speed, each channel of the strain gauge balance measures components due to gravity, inertia, and aerodynamics. The component due to gravitational force is a cyclic, equal and opposite variation about zero, whereas the inertial force is a function of model mass distribution and proportional to the square of the rotational speed. The aerodynamic damping force is proportional to wind speed and air density, as well as rotational speed. The gravity component is eliminated from both wind-on and wind-off data by integrating and averaging the signal. The inertial component is assumed to be constant with wind on and wind off, so the aerodynamic component is the difference between wind-on and wind-off measurements at the same rotational speed, provided wind-off measurements are made in a vacuum. However, if wind-off tests are made at atmospheric pressure, as is usually the case, the wind-off damping is also subtracted from the wind-on measurement. To reduce the wind-off

measurement to the inertial component alone, it is necessary to average the forces and moments produced by rotating the model in both directions. This mean is then subtracted from the wind-on reading at the same rotational speed to yield the total aerodynamic damping.

To measure the pressures, a 780B Pressure Measurement System from Pressure Systems, Inc. (PSI) was used, along with eight electronic scanning pressure modules (ESP-32) containing 32 ports each for a total of 256 ports. The modules used for the low-speed tests at Bedford were rated at a maximum range of ±2.5 psi while those for the high speed tests at Farnborough were ±5.0 psi. The plastic tubes from each port on the model surface were connected to one side of the differential pressure transducers mounted inside the model. The transducers converted the pressures to voltages. The voltage level for each of the ports was sent through the rig sliprings to the Data Acquisition and Control Unit in the tunnel control room. The voltages for all ports were then passed to the tunnel computer for conversion to pressures and coefficients and storage.

The number of pressure readings averaged at each rotation rate to arrive at a final value for each port was determined by the available system memory and from experience gained in previous rotary balance pressure and force tests. Forty readings were taken at each port over a 4 second time interval. These readings were then averaged to determine the final pressure value.

The error specification of the PSI 780B System was ±0.10% of full scale in a worst case. Drift in the system was the largest single cause of error in these tests, primarily due to temperature variations in the tunnel that affected the transducers. Re-zeroing the system at the start of each rotational sweep kept drift errors to a minimum. System zero checks indicated a worst case drift error of ±0.08%. Repeat runs have shown additional accuracy errors within ±0.04%. The combination of these errors produced an

9

overall system accuracy for these tests of within ±0.12% of the full-scale value of the transducers.

Much of the data collected at the low-speed facility in Bedford was corrupted due to problems with the test equipment. The sliprings became contaminated and interfered with the signals from the pressure modules, adversely affecting the pressure data. In fact, aftbody pressure data were only obtained for the rectangular hemisphere at 90° because the number 7 and 8 modules (containing the aftbody ports) were disconnected for the remainder of the testing, due to the slipring contamination. Due to the problems encountered at the low-speed facility at Bedford, some supplemental force and moment testing was conducted in the Langley 20-Foot Vertical Wind Tunnel in order to obtain some low Reynolds number data.

Presentation of Data

The force and moment data is typically presented as a function of non-dimensionalized rotation rate, $\Omega b/2V$, for Reynolds numbers based on body diameter ranging from approximately 80,000 to 2,200,000. As referred to in the discussion, damped in yaw is defined as a body-axis yawing moment that opposes the wind axis rotation, or a negative slope of yaw versus rotation. Conversely, a positive slope is indicative of propelling yawing moments. Figure 5 illustrates the damped and propelling quadrants for rotational yawing moments. While a negative slope of side force is not necessarily an indication of damped yawing moments, this report will refer to side force as being damped when the slope is negative and propelling when the slope is positive.

Software tools to visualize experimental data in an expeditious fashion have been developed and were used in the analysis of the pressure data obtained at the Bedford and Farnborough facilities. The surface pressures were assigned color values and mapped

onto a three-dimensional surface model of the configuration. Since the model could be positioned at any attitude, the flow effects could be examined over the entire configuration. The software also has the capability to display pressure increments between two flow conditions and to highlight a desired range of pressure coefficients. In this manner, flow effects due to rotation rate, angle of attack, or Reynolds number were easily observed. This capability not only provided initial on-site analysis, but also permitted early identification of equipment problems that would not have been identifiable in the test environment otherwise. Another example of the software capability is shown in Figures 6 and 7. Figure 6 illustrates the tap locations by displaying the pressure data mapped onto a surface model of the rectangular ogive. In order to view the data in its entirety, the surface shading can be turned off, as shown in Figure 7. The data presented in this report will be displayed in this manner so that more of the flowfield can be viewed at once.

RESULTS AND DISCUSSION

Of the two model forebody plan shapes tested (hemispherical and ogive), the ogive configurations were the most representative of typical aircraft. Consequently, this report will focus on the effects of Reynolds number on the flowfields about the rectangular and circular cross section ogives and attempt to gain further insight into the observed behavior of the measured static and rotational yawing moment characteristics using the visualization of the surface pressure data.

Although past forebody studies have made assumptions about stability characteristics based on side force behavior, the NASA/DRA data showed that side forces, both statically and at rotation rate, are not necessarily indicative of the yawing moment behavior. The significance of the yaw characteristics at high angles of attack, particularly the slope of yawing moment curve versus rotation, is of critical importance in determining a configuration's behavior at these angles. Propelling yawing moments versus rotation are indicative of possible departure susceptibility and spin behavior, and in configuration terms is considered adverse. Conversely, damped yawing moments are desirable from both a spin as well as a controlled maneuver standpoint. While previous research efforts have assumed that yaw behavior parallels that seen in side force and have frequently presented only these data, these tests indicated that this was not the case. The assumption that yawing moment has the same characteristics as side force[9] is unsatisfactory for static test conditions and can lead to completely erroneous conclusions when evaluating rotational behavior. This is shown graphically in the comparison of aerodynamic characteristics for the rectangular ogive at both 60° and 90° angle of attack, presented in Figure 8. The rotational yawing moment curves for the rectangular ogive configuration at these two angles of attack exhibited very similar slopes (Figure 8a), while the slopes of the rotational side force curves for the two angles of attack were opposite (Figure 8b). As a result of the numerous differences between yawing moment

and side force trends, as well as the fact that side force variation (included here for completeness) has a relatively insignificant contribution to aircraft behavior at high angles of attack, the following discussion will focus primarily on the variation of yawing moment with rotation rate.

Rectangular Ogive - 60° Angle of Attack

Figure 9 shows the Reynolds-number sensitivity of the rotational side force and yawing-moment characteristics for the rectangular ogive at 60° angle of attack. Corresponding surface pressure plots are presented in Figures 10 through 13.

As seen in Figure 9, increasing Reynolds number had little effect on the yawing moment characteristics at rotation. Even as Re_D increased from laminar flow conditions, through transitional to fully turbulent Re_D, the basic behavior in yaw remained the same: a highly damped configuration with little asymmetric yaw at static conditions. The pressure data presented in Figure 10 further illustrates the relative insensitivity to Reynolds number this configuration exhibits. At static conditions, the flow was characterized by attached flow along the four corners of the forebody. The formation of relatively symmetric forebody vortex structures is evidenced by the symmetry of the suction peaks on the bodies' upper surface. The basic surface pressure features remained relatively unchanged as Reynolds number increased to the maximum tested. The most prominent difference being a slight increase in the peak suction values at the nose as Reynolds number was increased.

The imposition of a wind axis rate on the forebody, as shown in Figures 11 and 12 for -.1 and +.1 $\Omega b/2V$ respectively, resulted in a rotation of the surface pressure distribution commensurate with the movement of the local velocity vector. The net result was a reduction in the local suction on the lower windward and upper leeward corners,

and an increase in suction on the remaining corners. The increased crossflow on the advancing upper corner resulted in a more pronounced vortex effect on the upper surface. The mechanism responsible for the yaw damping characteristics was also evident, and are more clearly shown for the rotation sweep depicted in Figure 13 at a Reynolds number of 2,090,000. As rotation rate increased, the rotation of the relative velocity vector produced an increase in pressure on the advancing face of the forebody, with the leeward side surface pressure remaining essentially unchanged from the static case. The net difference in the surface pressure on either side yielded the increase in damped yawing moment as rotation rate increased. As with the static case, the basic surface pressure features were essentially unchanged as Reynolds number increased, although the distinction between the separation of the upper corner vortex sheet and its re-impingement on the upper surface was more distinct for the highest Reynolds number case. Because these differences lie primarily in the longitudinal plane, their effect on the directional characteristics are minimal. The upper surface differences contributed to a static shift in the rotational pitching moment data as shown in Figure 14. The general rotational behavior remained similar, however.

For this configuration, increasing Reynolds number generally made the flowfield features more distinct, yet the basic structures, including the low pressure regions and separation lines, were relatively unaffected by Reynolds number. This apparently is a result of the fact that the key surface pressure features are defined by the corners of the rectangular body.

Circular Ogive - 60° Angle of Attack

The effects of rotation on the aerodynamic characteristics for the circular ogive at 60° angle of attack are presented in Figure 15 for selected Reynolds numbers. Pressure distributions at static and dynamic conditions are presented in Figures 16 through 20.

The force and moment data collected during these tests, in correlation with the pressure data, show that the separated vortex flow had a significant influence on the circular ogive at 60° angle of attack. Past experimental as well as empirical experience with circular forebody configurations have shown a considerable sensitivity of this shape to both geometric and flowfield variations that persist up to full scale flight Reynolds numbers.[9-12]

As expected, the rotational yawing moment and side force characteristics of the circular ogive at 60° angle of attack exhibited significant effects due to Reynolds number. At low Reynolds number, yawing moments remained well damped at all rotation rates, as shown in Figure 15a. However, an increase in Reynolds number resulted in significant changes to the rotational yawing moment (and side force) characteristics. Yaw damping was reduced in the transitional Reynolds number range, resulting in neutral to slightly propelling characteristics, and further increases in Reynolds number yielded very non-linear results. The rotational yawing moment characteristics were significantly different between Reynolds numbers of one and two million. As shown in Figure 15a, yawing moments were propelling at a Re_D of 1,400,000, but then became damped again at low rotation rates at a Re_D of 2,080,000. This behavior would indicate that either the flowfield was highly unstable at these high Reynolds numbers, or that Reynolds number dependent flowfield changes were still occurring as Re_D was increased through this region. It is worth noting, however, that at low rotation rates the very low Reynolds number test data did provide a better representation of the highest Reynolds number moment characteristics.

Distinct flow patterns were also observed for different ranges of Reynolds numbers. For Re_D less than 200,000, the vortex cores remained close to the forebody surface. Consequently, above the suction peaks associated with the attached cross-flow on

15

the forebody sides, a strong secondary suction peak was exhibited on the upper body, as shown in Figure 16a for a Reynolds number of 89,000 under static conditions. As mentioned previously, the very low Reynolds number data obtained from Bedford was subject to equipment sensitivity as well as slipring problems that introduced errors on individual ports. The basic flow structure is still evident, however. As Reynolds numbers increased into the transitional range between 200,000 and 500,000, the vortex flow became highly asymmetric as the individual vortices began detaching from the surface independently. This asymmetric separation is illustrated in Figure 16b, at a Reynolds number of 350,000 and zero rotation. The separation lines along the upper portion of the forebody indicated that the right-side vortex detached from the surface ahead of the left-side vortex. Note that the flow exhibited greater attachment along the entire left side of the body (Figure 18a). This increased attachment on the left-hand side of the body was especially evident on the aftbody. The flow asymmetry on the aftbody was apparently responsible for the positive yaw offset that occurred at this Reynolds number (Figure 15a). As the Reynolds number increased above 500,000 the vortex flow became more symmetric, with both vortices lifting away from the body at the apex of the ogive. The pressure data in Figure 16c shows that at a Reynolds number of 703,000 the vortices had almost completely detached from the forebody surface. At a Reynolds number of 1,080,000 the vortices remained fully detached, but as Reynolds number increased further, they appeared to move progressively closer to the surface again, as evidenced by the more pronounced upper surface suction peaks shown in Figures 16d and 16e for Reynolds numbers of 1,400,000 and 2,080,000, respectively.

Figure 17 shows the re-orientation of the vortex structure on the forebody, with the suction peaks highlighted, induced by a rotation rate of -0.2 $\Omega b/2V$ at low Reynolds number. The vortex structure migrated around towards the right side of the forebody due to rotation, and the increase in the downwind suction as well as realignment of the lower

16

surface positive pressure was responsible for the high level of yaw damping exhibited under these conditions. For transitional Reynolds numbers, where yaw damping was reduced, there was much less variation in the forebody flowfield due to rotation (see Figure 18 for a Reynolds number of 350,000). The relative change in the aftbody flow characteristics was perhaps more influential at this Reynolds number. As shown in the moment data, significant changes in the rotational characteristics occurred as Reynolds number increased from one to two million. Figure 19a presents a comparison of the flowfield for Reynolds numbers of 1,400,000 and 2,080,000 and rotation rates of -0.1 and -0.2 $\Omega b/2V$. For both Reynolds number conditions, the pressure field was rotated due to the orientation of the velocity vector at rotation, with the positive pressure region on the lower surface rotated toward the relative wind and the upper surface vorticies rotated away from the relative wind. While initial inspection of the pressure data indicated the flowfields were similar, the force and moment data revealed distinct differences at a rotation rate of -0.1 $\Omega b/2V$. At this rotation rate, yaw was damped at the higher Reynolds number and propelling at the slightly lower Reynolds number (Figure 15a). As a result, closer examination of these flowfields was performed by subtracting the pressure coefficients for Re_D=1,400,000 from those obtained at Re_D=2,080,000, displaying the effect of Reynolds number on the forebody pressures (Figure 19a). The differences in the moment characteristics became evident in the incremental data, where the Re_D=2,080,000 configuration exhibited more downwind suction and less upwind suction than the Re_D=1,400,000 configuration, both concurrent with the differences observed in the yaw damping. Closer inspection of the attachment lines and separation lines revealed subtle differences in the two Reynolds number conditions. It should be noted that the two Reynolds numbers were tested consecutively, following an increase in tunnel pressurization (the model was not handled between these two runs). When the rotation rate was increased to -0.2 $\Omega b/2V$, the moment data showed very similar results for both Reynolds numbers. Correspondingly, the pressure data were also similar, as shown by

both the complete and incremental surface pressure plots in Figure 19b. The full effect of rotation on the pressure distribution for the highest Reynolds number tested is shown in Figure 20.

Despite the different pressure distributions about the circular ogive at 60° angle of attack for laminar and fully turbulent separation, the resulting rotational yawing moment characteristics at low rotation rates were found to be very similar. The flow separation states influencing ogive aerodynamics (i.e. laminar, transitional and turbulent boundary layer separation) were also responsible for the variation in rotational behavior. The transitional Reynolds number effects, wherein the boundary layer states varied from the left to the right side of the body, were further exacerbated with the imposition of rotary flow. These effects apparently occur at high Reynolds numbers when the local Reynolds number on a tapered body such as an ogive is still within the transitional range. The relative instability of the flowfield at transitional flow conditions was also observed during repeat runs of equivalent test conditions. In general, the repeatability of the test data at transitional Reynolds numbers was not as good as the repeatability at fully laminar or fully turbulent flow conditions.

Rectangular Ogive - 90° Angle of Attack

The effects of Reynolds number on the rotational yawing moment and side force characteristics for the rectangular ogive at 90° angle of attack are shown in Figure 21. Corresponding surface pressure plots are presented in Figures 22 through 28.

At 90° angle of attack, the yawing moment characteristics and the flowfield about the rectangular ogive were strongly influenced by Reynolds number effects and rotation rate. At low Reynolds numbers ($Re_D < 200,000$) the rectangular ogive was typically propelling in yaw, with substantial static offset values occurring as Re_D approached 200,000. The offsets were reduced as Reynolds number was further increased, and

18

transition from propelling to damped yaw occurred at increasing rotation rates until yaw was fully damped for Reynolds numbers above 500,000 (Figure 21a). The effect of Reynolds number on the rectangular ogive flowfield at static conditions is shown in Figure 22.

For very low Reynolds numbers ($Re_D < 100,000$), the flow was separated over the entire configuration. Large static yaw offsets occurred on the rectangular ogive at slightly higher Reynolds numbers due to asymmetric flow attachment on the aftbody, as the flow was completely detached from the forebody at these Reynolds numbers. This flow separation is illustrated in Figure 22a for a Reynolds number of 178,000. The flow was completely detached from the forebody, with reattachment occurring along the left-hand side of the aftbody, resulting in a positive yaw offset (Figure 21a). This offset was greatly reduced as Reynolds number increased, due to symmetric flow attachment along both sides of the body. Figure 22b shows that the flow began to attach along the lower corners of the forebody as Reynolds number increased to 401,000. As Reynolds number further increased, the flow attachment lines continued to move forward on the forebody until the flow was fully attached at the very front of the ogive nose, as shown in Figure 22c for a Reynolds number of 2,237,000.

As the angle of attack increased to 90° at static conditions, the three-dimensional cross-flow around the forebody configuration diminished and became more analagous to two-dimensional cylinder type flow.[13] The forebody flow attachment was highly dependent on Reynolds number, because the local Reynolds number varied with the diameter of the ogive nose. Therefore, as Re_D increased, the local Reynolds numbers on the nose increased as well. Figure 22 showed the forward progression of flow attachment on the forebody as a result of increasing the Reynolds number. By evaluating the pressure data obtained at various cross-sections along the forebody under static conditions, it was

determined that a minimum local sectional Reynolds number (based on local diameter) of at least 200,000 was necessary in order to enable flow attachment on the forebody. Figure 23 illustrates the effect of Reynolds number on local flow attachment about the forebody at a distance of 0.67x/D from the nose tip (forebody station 3). The cross-sectional pressure distribution for a Reynolds number (Re_D) of 401,000 at this forebody station is shown in Figure 23a. Note the development of low pressure regions at the lower corners, an indication of flow attachment on the forebody. The local Reynolds number at this cross-section was approximately 220,000. The pressure distribution at the same body station is shown in Figure 23b for a lower Re_D of 178,000. The constant pressure around the sides and top of the body are indicative of the laminar separation that occurs at such low Reynolds numbers. Head-on views of the forebody flowfield for the same Re_D of Figure 23 are shown in Figure 24 for reference.

As noted above, the rectangular ogive at 90° was propelling in yaw for Reynolds numbers below 200,000. Surface pressure data measured at rotation, shown in Figure 25, indicated that the flow around the aftbody contributed heavily to the overall yawing moment characteristics measured for a Reynolds number of 178,000. At high rates of rotation the flow became attached on the windward corners of the forebody and the aftbody, as shown in Figure 25a for -0.4 $\Omega b/2V$. The reduction in surface pressure at the windward corners, due to the attaching flow, resulted in propelling yawing moments. The local velocity vector was reduced with decreasing rotation rates, resulting in decreased suction on the forebody until the flow was completely separated from the forebody at rotation rates of ±0.1 $\Omega b/2V$. As the rotation rate decreased to zero, a region of strong suction developed along the left-hand side of the aftbody while the forebody flow remained separated, generating positive yawing moments. At low rotation rates, the flowfield around the configuration seemed to be independent of the direction of rotation, as shown in Figures 25b and 25c for rotation rates of -0.05 and +0.05 $\Omega b/2V$,

respectively. This corresponds with the moment data of Figure 21a, where the yawing moments were fairly constant between rotation rates of -0.1 $\Omega b/2V$ and +0.1 $\Omega b/2V$. As $\Omega b/2V$ increased, the flow effects on the aftbody were reduced while the flow became attached along the lower windward corner of the forebody, due to an increase in the local velocity vector (Figure 25a). This suction on the forebody was responsible for the propelling yawing moments measured at low Reynolds numbers.

A transitional region was observed between Reynolds numbers of 200,000 and 500,000, where transition from propelling to damped yaw occurred with increasing rotation rate. This transition is characterized by a discontinuity in the slopes of the yawing moment curves. The propelling moments observed at these Reynolds numbers were a result of a region of attached flow along the windward corner of the forebody nose, as shown in Figures 26a and 27a for $Re_D=209,000$ (-0.2 $\Omega b/2V$) and $Re_D=401,000$ (-0.4 $\Omega b/2V$), respectively. These figures show the pressure field just before transition to damped yaw had taken place. For a Reynolds number of 209,000, the rectangular ogive was propelling between rotation rates of about 0.4 and 0.2 $\Omega b/2V$, but as Reynolds number increased to 401,000 yaw was only propelling at very high rotation rates (Figure 21a). As Reynolds number increased, transition occurred at higher rates of rotation until yaw was fully damped for Re_D above 500,000. Damping moments were generated when the cross-flow over the forebody was separated and reattached along the leeward side of the aftbody, as shown in Figures 27c and 27d for $Re_D=401,000$ and -0.3 $\Omega b/2V$. A full view of the configuration is included in Figures 27b and 27d to more clearly illustrate the influence of the aftbody at transitional Reynolds numbers. Correlation between the yawing moments and forebody pressures suggested that transition occurred similarly for $Re_D=209,000$ at a lower rotation rate of -0.15 $\Omega b/2V$, although no surface pressures were obtained on the aft end due to the problems encountered at the Bedford facility. However, the front view of the forebody pressures for $Re_D=209,000$, shown in Figure 26b,

illustrates a similar pattern of flow separation over the forebody when yaw transitioned from propelling to damped. As rotation rate decreased the flow was less likely to remain attached at the nose tip due to a reduction in the local velocity.

As Reynolds number increased beyond 500,000 and out of the transitional range, the flow became fully attached on the forebody with damped yawing moments resulting. Figure 21a shows that yaw was similarly damped for post-transitional Reynolds numbers. Correspondingly, the flowfield was relatively independent of Reynolds number once the flow was no longer transitional. For example, Figure 28 illustrates the similarities in the rotational flowfield at Reynolds numbers of 1,142,000 and 2,237,000 for an $\Omega b/2V$ value of -0.2. Note the more prominent suction lobe along the leeward corner of the forebody, contributing to the damped moment. Additionally, the strong flow attachment along the leeward side of the aftbody increased the magnitude of the yawing moment.

Although yaw was clearly propelling at low Reynolds numbers before gradually transitioning to fully damped at higher Reynolds numbers, visualization of the surface pressures indicated that the flow around the aftbody greatly influenced the overall yaw characteristics measured on the rectangular ogive. The flow was separated over the forebody for low Reynolds numbers and low rotation rates. As rotation rate increased, the flow became attached along the windward side of the forebody due to the increased local velocity. The propelling moments were generated by flow reattachment on the aftbody at low rotation or attached flow along the windward corner of the forebody at higher rates of rotation. As Re_D increased, strong suction on the leeward side of the aftbody produced significant damping moments.

Since the aftbody flowfield so heavily influenced the total yawing moment results for the rectangular ogive, an effort was made to quantify the yawing moments generated by the aft end in order to isolate the characteristics of the forebody alone. This was done

by comparing the rectangular ogive and the rectangular hemisphere data, since the aftbodies were identical and the overall yaw characteristics were similar. As was the case with the rectangular ogive, the rectangular hemisphere was propelling in yaw at low Reynolds numbers before transitioning to fully damped in yaw at high Reynolds numbers (Figure 29a). Visualization of the pressures showed that the difference in forebody geometry for the two configurations had little effect on the downstream flow characteristics. The effect of forebody geometry on the aftbody flowfield for the two rectangular cross-section bodies is shown in Figure 30 at low Reynolds number, and in Figure 31 for a Reynolds number of approximately two million. Note the similarity in the location and relative strengths of the suction lobes on the aftbodies at both flow conditions. This indicated that the differences in forebody geometry had little effect on the flow downstream. Therefore, the influence of the aftbody on the yawing moment characteristics should be equivalent for both configurations. Since the forebody and aftbody are identical on the rectangular hemisphere, it can be assumed that half of the total yawing moment obtained at each rotation rate for this shape were generated by the flow about the aftbody.

At moderate to high values of Re_D, the rectangular ogive yawing moments appeared to have been strongly influenced by the flowfield about the aftbody. Therefore, in order to isolate the effects of the ogive forebody for a given Reynolds number, one half of the magnitude of the yawing moments obtained for the hemisphere were subtracted from the rectangular ogive yawing moments at an equivalent Reynolds number. The result was an estimate of the yawing moment characteristics of the rectangular ogive due to the forebody alone (Figure 32). The results in Figure 32 indicate that the level of yaw damping on a rectangular ogive forebody at 90° angle of attack may be somewhat reduced from what was shown in Figure 21a.

Circular Ogive - 90° Angle of Attack

The rotational side-force and yawing-moment characteristics at several Reynolds numbers are presented in Figure 33 for the circular ogive at 90° angle of attack. Note that yawing moments were damped for all Reynolds numbers. Supporting pressure distribution plots are presented in Figures 34 through 37.

The circular ogive was damped in yaw for all Reynolds numbers (Figure 33a), with large static offsets occurring in the transitional Reynolds number region. Note that the offsets were reduced for both low and high Reynolds numbers. However, an increase in the offset occurred at the highest Reynolds number tested (Re_D=2,080,000), indicating that fully turbulent flow conditions had not yet been attained.

As with the rectangular ogive at 90° angle of attack, the flow about the circular ogive forebody at static conditions was two-dimensional and highly dependent on the local Reynolds number. Figure 34 illustrates the forward progression of flow attachment on the forebody as Reynolds number increased from 350,000 to over two million. Asymmetric flow attachment was evident over the aft portion of the body at transitional Reynolds numbers, as shown in Figure 34a for Re_D=350,000, the lowest Reynolds number for which pressures were obtained for this configuration. The flow was detached over much of the forebody, with strong suction developing on the left-hand side of the aftbody. This suction on the aftbody, in combination with the long moment arm, generated a substantial static offset in yaw (Figure 33a). As Reynolds number increased, the flow began attaching farther forward on the forebody until the flow was finally attached at the tip of the ogive nose. For a Reynolds number of 690,000, the flow was attached just aft of the nose tip and was symmetric along both sides of the body (Figure 34b). For Re_D=1,380,000 (Figure 34c), the flow had become attached at the very front of the ogive nose and remained relatively symmetric along both sides of the body. As

Reynolds number increased to two million the flow became asymmetric again as the vortex pair began to migrate bcak towards the forebody surface (Figure 34d). The right-hand vortex appeared to generate greater suction along that side of the forebody. This vortex asymmetry could explain the static yaw offset seen in Figure 33a for Re_D=2,080,000. The moment and pressure data for the circular ogive at both 60° and 90° angles of attack indicated that there were still some remaining instabilities in the flow as Reynolds number increased from one to two million. Thus, additional testing at higher Reynolds numbers may be necessary in order to obtain data at fully turbulent flow conditions. Higher Reynolds number testing may help determine if this flow asymmetry exists at fully turbulent conditions as well, or if it is merely an effect of transition.

The yaw damping on the circular ogive at 90° angle of attack was a result of a reorientation of the pressure field about the forebody with rotation. The positive pressure (stagnation) region became skewed around towards the windward side of the forebody as rotation was induced, resulting in an opposing moment at the nose. This effect is more clearly illustrated by viewing the pressures cross-sectionally. Figure 35 illustrates the static and rotational effects on the pressure field about the circular ogive at forebody station 2 (x/D=0.333) for Re_D=350,000. Under static conditions the positive pressure region was centered along the bottom of the forebody (Figure 35a). The effect of a rotation rate of 0.2 $\Omega b/2V$ on the same cross-section is shown in Figure 35b for counter-clockwise rotation and in Figure 35c for clockwise rotation. Although the flow was fully separated at these conditions, damping moments were generated by the reorientation of the positive pressure region about the forebody with rotation. Note that the pressure field on the forebody was pulled in the direction of rotation. For example, the stagnation point rotated counter-clockwise on the forebody when the model was rotated in the counter-clockwise direction (Figure 35b). Similarly for clockwise rotation, the stagnation point was pulled clockwise about the forebody (Figure 35c).

The rotational flow effects on the forebody are shown in Figure 36 for increasing Reynolds number at a rotation rate of -0.2 Ωb/2V. The effects were noticeable at low Reynolds number in the orientation of the positive pressure region around the bottom of the forebody (Figure 36a). As Reynolds number increased, the rotational effects became more evident in the reorientation of the low pressure lobes on the forebody. This is illustrated in Figures 36b and 36c as the right-hand suction lobe was situated lower on the forebody than the left-hand suction lobe. The vortex asymmetry observed for a Reynolds number of two million became exaggerated with rotation as the left-hand vortex was pulled over towards the right-hand side of the forebody (Figure 36d). For completeness, the entire flowfield is shown in Figure 37 for the same Reynolds numbers and rotation rate of Figure 36. Asymmetric flow attachment on the aftbody contributed to the large yawing moments that occurred at a Reynolds number of 350,000 (Figure 37a). As Reynolds number increased to 690,000 the aftbody flow became more evenly attached along both sides, thus reducing the magnitude of the yawing moments (Figure 37b). Also note the reorientation of the aftbody pressure field that occurred with rotation. This is most easily seen when the rotational flowfields in Figure 37 are compared with the static flowfields shown in Figure 34. As the body rotated in the counter-clockwise direction, the positive pressure region on the aftbody migrated towards the right-hand side of the body, which is equivalent to the windward side of the aftbody

The reorientation of the pressure along the bottom of the circular ogive generated damping moments at 90° angle of attack for all Reynolds numbers. This was particularly true at low Reynolds numbers where the flow was fully detached, and the pressures were constant over most of the body. In contrast, yaw was propelling for the rectangular ogive at 90° angle of attack at low Reynolds numbers. The flow was separated on the

rectangular ogive at low Reynolds numbers as well, but the positive pressure region along the bottom was constrained by the corners of the rectangular cross-section.

Effect of Flow Modifiers

Interest in the modification of the forebody flowfield at high angles of attack has ranged from the manipulation of the surface pressure distribution to permit the replication of high Reynolds number characteristics at low Reynolds number test conditions (e.g. Reference 14), to the outright modification of the flowfield to improve the basic airplane behavior and control characteristics (e.g., Reference 15). Because of these concerns, a limited attempt was made during the course of these tests to evaluate the influence of Reynolds number and rotation on a typical trip strip and a strake installation on the circular ogive configuration.

Effect of Trip Strips

The installation of flow tripping strips along the lower portion of the body was configured based on DRA experience with similar applications, as shown in Figure 4a. The flow tripping surfaces consisted of the raised edges of small holes punched in a thin metal strip with the dimensions shown. The effect of these devices on the circular forebody's yaw and sideforce characteristics at various Reynolds numbers is shown in Figure 38.

The typical purpose of adding devices such as these to a configuration's forebody is to attempt to stimulate the development of fully turbulent flow conditions at Reynolds numbers below where this flow condition would naturally occur. This technique has been used with some success in other static testing, but as seen in the force and moment data of Figure 38, the application of these devices can be problematic. When applied to this particular configuration, the yaw characteristics were significantly changed from the clean

27

forebody data, at both low and high Reynolds numbers. With the strips applied, very large asymmetries in yaw developed for all Reynolds numbers tested and the rotational characteristics varied widely with Reynolds number, ranging from highly asymmetric between positive and negative rotation rates, to invariant with rotation. While very carefully applied, some asymmetry in the attachment of the strips was apparently responsible for the pervasive offsets that exceeded the highest values observed with the clean forebody. The pressure data, as shown for various Reynolds numbers at static conditions in Figure 39, revealed the distortion on the forebody flowfield imposed by the addition of the strips. For the Re_D tested, the strips did provide a relatively invariant forebody surface pressure distribution. However, all cases exhibit the increased suction on the right hand side of the body corresponding to the positive yaw offsets seen in the moment data. This region of enhanced attached flow on the right side of the body also produced a more pronounced vortex suction peak on that side of the upper body. The effect of rotation rate is depicted in Figure 40 at a Re_D of 2.1 x 10^6 and shows how the surface pressure distribution was only slightly influenced by increasing rate. This observation further illustrates the difficulty of applying flow tripping devices to a configuration for any conditions other than static, zero sideslip conditions. As shown in the data of Figure 40, by not moving the strip location as a function of the movement of the local velocity vector, the flowfield was more or less fixed in a static alignment and was unable to match the natural re-orientation of the surface pressure distribution. As a result, the moment data was essentially unchanged with increasing rate (see Figure 38 at a Re_D of 2.1 x 10^6). While not tested in this particular test, it is likely that a similar situation would have arisen for non-zero sideslip conditions as well.

Effect of Forebody Strakes

Several recent high angle of attack aircraft have utilized the application of forebody strakes to improve their high angle of attack characteristics (e.g., the X-29 and the X-31, as described in References 16 and 2). In both cases the primary function of the strakes was to reduce the incidence of asymmetric yaw offsets that frequently occur on these types of forebodies. Other low Reynolds number test work has shown that when properly located, nose strakes can also have a beneficial influence on the rotational yaw damping.[17] For these reasons, test data was taken for the strake configuration shown in Figure 4b, with the strake mounted at a 45° angle above the maximum half breadth of the local cross section.

The effect of the addition of this strake on the circular forebody's side force and yawing moment characteristics at various Reynolds numbers is shown in Figure 41. As shown in this figure, the addition of the strake had a pronounced effect on the yaw damping characteristics, substantially increasing the damping for all rotation rates tested, as well as generally reducing the asymmetric yawing moments at static conditions. While there was a static moment displacement between the lower and the highest Re_D curves, the damping slopes remained very consistent throughout the range of Re_D tested. As was the case for the rectangular ogive, the geometric features presented by the strakes resulted in a consistent surface pressure distribution for all tested Re_D as well. At static conditions (e.g. Figure 42) the presence of the strake disrupted the formation of attached flow along the fuselage sides that is characteristic of circular ogive bodies until aft of the strake. Strong vorticity shed from the strake edges resulted in upper surface suction whose peak values decreased slightly with increasing Re_D. For all Re_D, the downstream attached flow regions were less pronounced than that seen on the clean forebody (e.g., Figure 43 comparing the clean forebody pressures with the strake configuration at a Re_D of 2.1 x 10^6).

The effect of rotation on the surface pressure distribution revealed the source of the Reynolds number independent yaw damping observed in the moment data. As seen in Figure 44, which shows the effect of rotation on the strake configuration at a Re_D of 2.1×10^6, increasing rotation rate skewed the lower surface transition point associated with the development of attached flow towards the windward strake and away from the leeward strake. This resulted in a further reduction of attached flow under the windward strake (and an increase in surface pressure), along with the development of limited attached flow under the leeward strake (a decrease in the surface pressure). This pressure differential between the forebody sides resulted in damped yawing moments with rotation. This reorientation of the surface pressures was essentially the same for all Re_D tested, as shown in Figures 45 and 46, which portrays the effect of rotation rates of -.1 and -.2 $\Omega b/2V$ at selected Re_D.

These test results revealed that the beneficial effects observed in earlier low Reynolds number testing for this particular strake configuration are relatively invariant with Reynolds number, and thus may have potential as a device to limit or avoid adverse propelling yaw characteristics. The strake test results also reiterated those observed with the rectangular ogive configuration, wherein geometric features that fix vortex development yield configurations that are relatively insensitive to the test Reynolds number.

CONCLUSIONS

Rotary balance experiments were conducted on rectangular and circular ogive forebodies at 60 and 90 degrees angle of attack over a wide range of Reynolds numbers to determine the effects of nose geometry, angle of attack, and rotation on the aerodynamic characteristics of fuselage-type forebodies. These tests successfully measured, for the first time, the surface pressure distribution of these configurations under dynamic conditions in a pressurized tunnel. The results of the tests were to provide an initial exploration of the effects of velocity vector roll rates and Reynolds numbers on simple geometries, as well as to provide a database for the development of high angle of attack computational methods. Analysis of a limited portion of this substantial database has led to the following conclusions.

The characteristics observed on the circular ogive at 60° angle of attack reflected those observed in previous studies of the same configuration. The pressure data clearly showed the influence of different boundary layer separation conditions on the forebody flowfield and how the onset of rotation rate further affected the separation characteristics. Although the surface pressure data showed significant structural differences in the flowfield between low and high Reynolds numbers, the yaw damping characteristics at low rotation rates were similar for both fully laminar and fully turbulent flow conditions. As would be expected, rotational yaw damping varied considerably for test data measured throughout a broad transitional Reynolds number region. The range of transitional Reynolds numbers was influenced by local sectional Reynolds numbers that remained transitional on the forward end of the body, well after the flow over the remainder of the body had become fully turbulent.

At 90° angle of attack, the effects of Reynolds number on the flowfield were very distinct. The flow was completely detached for both the rectangular and circular ogive

configurations at laminar flow conditions. As Reynolds number increased, flow attachment occurred on the forebodies where the local Reynolds number was at least 200,000.

As rotation was induced on the configurations at 90° angle of attack, significant geometric and Reynolds number sensitivities were revealed in the flowfields and yawing moment characteristics. For the rectangular ogive configuration at laminar separation conditions, the acceleration of the flow on the upwind corner induced flow attachment and propelling moments. The flow was attached on all corners of the forebody at fully turbulent conditions, with suction on the downwind corner increasing with rotation and resulting in damped yawing moments. Non-linear transition occurred between the low Reynolds number, propelling yaw characteristics and the damped yaw at fully turbulent conditions. The flow characteristics in this transitional range varied widely between the two extremes, depending on the local Reynolds number and rotation rate.

The circular ogive did not have the "sharp" configurational features such as the corners on the rectangular ogive. Consequently, as rotation was imposed at low Reynolds numbers, the predominant change in the flowfield was the realignment of the stagnation point with the velocity vector. This reorientation of the flow was sufficient to produce damped yawing moments with rotation. As with the rectangular ogive, the moment characteristics at transitional Reynolds numbers varied considerably as the local flow on the circular ogive was influenced by rotation rate and local Reynolds numbers.

Due to the high rotation rates required to test at high Reynolds numbers and the high structural loads imposed on the model and test rig, rotary balance testing is much more practical and cost-efficient when conducted at low Reynolds numbers. One of the objectives of these tests was to identify the capabilities and limitations of using low

Reynolds number data to emulate high Reynolds number characteristics. For the limited database examined herein it appears that with some restrictions, the data obtained at laminar separation conditions can be used to predict the turbulent Reynolds number characteristics. Obviously, continuation of these efforts would be highly beneficial, and would include an examination of other angles of attack and forebody geometries (i.e. elliptical and chined forebodies), as well as the influence of other flow modifiers and strake effects. The development of tools to isolate the forebody forces and moments (surface pressure integration or direct forebody force and moment measurements) would also be helpful in further isolating the effect of configuration changes on forebody characteristics.

REFERENCES

1. Ralston, J.N.; and Barnhart, B.P.: Application of Rotary Balance Data in the Analysis of High Angle-of-Attack Characteristics, NASA CP 3149, November 1990.

2. Dickes, E.; Kay, J. and Ralston, J.: Validation of the NASA Dryden X-31 Simulation Aerodynamic Math Model and Evaluation of Mechanization Techniques, Bihrle Applied Research Report No. 93-4, June 1993.

3. Kalviste, J.: Use of Rotary Balance and Forced Oscillation Test Data in a Six Degree of Freedom Simulation, AIAA Paper 82-1364, August 1982.

4. Advisory Group for Aerospace Research and Development, North Atlantic Treaty Organization, Rotary-Balance Testing for Aircraft Dynamics, AGARD-AR-265, December 1990.

5. Dickes, E.G.; Hultberg, R.S.; and Ralston, J.N.: Report of Rotary Balance Wind Tunnel Testing on Generic Forebody Configurations Consisting of Pressure Measurements and Force and Moment Data Conducted at the Defense Research Agency Bedford/Farnborough Facilities, Bihrle Applied Research Report No. 92-5, September 1992.

6. Mason, A.A.; Jordan, S.W., Jr.; and Hultberg, R.S.: Test Report of Pressure Measurement on the F-16 Airplane During Steady-State Rotational Motion, Bihrle Applied Research Report No. 90-7, April 1990.

7. Pick, George S.: Investigation of Side Forces on Ogive-Cylinder Bodies at High Angles of Attack in the M=0.5 to 1.1 Range, AIAA Paper 71-570, June 1971.

8. Polhamus, E.C.: A Review of Some Reynolds Number Effects Related to Bodies at High Angles of Attack, NASA CR-3809, August 1984.

9. Clark, W.H.; Peoples, J.R.; and Briggs, M.M.: Occurrence and Inhibition of Large Yawing Moments During High Incidence Flight of Slender Missile Configurations, AIAA Paper 72-968, September 1972.

10. Lamont, P.J.: Pressure Measurements on an Ogive-Cylinder at High Angles of Attack with Laminar, Transitional, or Turbulent Separation, AIAA Paper 80-1556, August 1980.

11. Keener, E.R. and Chapman, G.T.: Onset of Aerodynamic Side Forces at Zero Sideslip on Symmetric Forebodies at High Angles of Attack, AIAA Paper 74-770, August 1974.

12. Kegelman, J.T. and Roos, F.W.: Influence of Forebody Cross-Section Shape on Vortex Flowfield Structure at High Alpha, AIAA Paper 91-3250, September 1991.

REFERENCES (Concluded)

13. Bertin, John J. and Smith, Michael L.:Aerodynamics for Engineeers. Second Edition, 1989.

14. Hall, R.M. et al: A Status Report on High Alpha Technology Program (HATP) Ground Test to Flight Comparisons, NASA CP-10143 Vol. 1, July 1994.

15. Simon, James M.; LeMay, Scott and Brandon, Jay M.: Results of Exploratory Wind Tunnel Tests of F-16/Vista Forebody Vortex Control Devices, WL-TR-93-3013, January 1993.

16. Croom, Mark A.; Whipple, Raymond D.; Murri, Daniel G.; Grafton, Sue B., and Fratello, David J.: High-Alpha Flight Dynamics Research on the X-29 Configuration Using Dynamic Model Test Techniques, SAE Technical Paper Series 881420, October 1988.

17. Ralston, John N.: Rotary Balance Data and Analysis for the X-29A Airplane for an Angle-of-Attack Range of 0° to 90°, NASA CR-3747, August 1984.

LIST OF FIGURES

LIST OF FIGURES (Continued)

LIST OF FIGURES (Concluded)

TABLE I.- Wind Tunnel Tests In Ascending Order Of Reynolds Number
a) Rectangular Hemisphere (α=90°)

Run No.	Tunnel Serial No.	α deg	Mach No.	Reynolds No.	V ft/s (m/s)	q lb/ft² (N/m²)	Temp °F (°C)	p atm	Ωb/2V Schedule	Pressure File Name	Remarks
B12	197-208	90	.024	89,000	26 (8)	0.9 (42)	41 (5.1)	1	A* w/o +.10	RH_A90_V8	
F7	91-105	90	.105	165,000	115 (35)	7.9 (378)	72 (22.4)	.5	A	RH9035P5	
B4	68-81	90	.060	210,000	66 (20)	5.2 (247)	44 (6.5)	1	A	RH_A90_V20	
B9	148-162	90	.090	315,000	98 (30)	11.6 (555)	41 (5.1)	1	A	RH_A90_V30	
B11	180-194	90	.099	345,000	108 (33)	14.0 (668)	41 (5.1)	1	A	RH_A90_V33	
F8	107-121	90	.210	350,000	230 (70)	32.2 (1542)	76 (23.4)	.5	B	RH9070P5	
F3	29-43	90	.106	363,000	115 (35)	16.8 (804)	70 (21.1)	1	A	RH9035P1	
B10	164-178	90	.106	367,000	115 (35)	15.7 (753)	41 (5.1)	1	A	RH_A90_V35	
B8	132-146	90	.120	420,000	131 (40)	20.6 (986)	41 (5.1)	1	B*	RH_A90_V40	
B7	116-130	90	.150	521,000	164 (50)	32.0 (1530)	41 (5.1)	1	B*	RH_A90_V50	
B6	100-114	90	.180	628,000	197 (60)	46.2 (2210)	41 (5.1)	1	B**	RH_A90_V60	
F5	60-73	90	.105	712,000	115 (35)	32.3 (1546)	73 (22.6)	2	A	RH9035P2	
B5	84-98	90	.210	730,000	230 (70)	62.7 (3000)	42 (5.6)	1	B	RH_A90_V70	
F4	45-59	90	.210	731,000	230 (70)	66.2 (3170)	74 (23.4)	1	B	RH9070P1	
F20	296-310	90	.105	1,020,000	115 (35)	47.0 (2250)	82 (27.6)	3	A	RH9035P3	
F6	75-89	90	.210	1,391,000	230 (70)	127.2 (6090)	73 (22.6)	2	B w/o -.22	RH9070P2	
F19	280-293	90	.210	2,030,000	230 (70)	189.0 (9050)	84 (28.8)	3	B w/o ±.22	RH9070P3	No -.225 Ωb/2V Pressure Data

TABLE I.- Continued.
b) Rectangular Hemisphere (α=60°)

Run No.	Tunnel Serial No.	α deg	Mach No.	Reynolds No.	V ft/s (m/s)	q lb/ft² (N/m²)	Temp °F (°C)	p atm	Ωb/2V Schedule	Pressure File Name	Remarks
B24	389-401	60	.024	87,000	26 (8)	0.9 (41)	43 (6.0)	1	A* w/o +.10	RH_A60_V8	Station 1,8,29,32,5 Bad Pressure Data
F17	248-261	60	.105	175,000	115 (35)	8.4 (402)	76 (24.6)	.5	A w/o -.15	RH6035P5	No -.4 Ωb/2V Pressure Data
B23	373-387	60	.060	192,000	66 (20)	4.7 (225)	43 (6.0)	1	A	RH_A60_V20	Station 1,8,29,32,5 Bad Pressure Data
B22	357-371	60	.100	315,000	98 (30)	11.6 (555)	43 (6.0)	1	A Approx.	RH_A60_V30	Station 1,29,32,5 Bad Pressure Data
F18	264-278	60	.210	350,000	230 (70)	31.4 (1503)	78 (25.5)	.5	B	RH6070P5	
F15	216-230	60	.105	360,000	115 (35)	16.3 (780)	75 (24.0)	1	A	RH6035P1	Station 1,29,32,5 Bad Pressure Data
B15	241-255	60	.120	420,000	131 (40)	20.6 (986)	41 (5.1)	1	B*	RH_A60_V40	Station 1,29,32,5 Bad Pressure Data
B21	341-355	60	.150	521,000	164 (50)	32.0 (1530)	40 (4.6)	1	B*	RH_A60_V50	Station 1,29,32,5 Bad Pressure Data
B20	325-339	60	.180	628,000	197 (60)	46.1 (2210)	40 (4.6)	1	B**	RH_A60_V60	Station 1,29,32,5 Bad Pressure Data
F16	232-246	60	.210	700,000	230 (70)	63.0 (3017)	79 (26.1)	1	B	RH6070P1	
F13	184-198	60	.105	710,000	115 (35)	33.1 (1585)	75 (23.8)	2	A	RH6035P2	
B19	309-323	60	.210	730,000	230 (70)	62.7 (3000)	43 (5.9)	1	B	RH_A60V70R	Station 1,29,32,5 Bad Pressure Data
F12	168-182	60	.105	1,050,000	115 (35)	47.5 (2274)	78 (25.3)	3	A	RH6035P3	
F14	200-214	60	.210	1,400,000	230 (70)	130.8 (6263)	78 (25.8)	2	B	RH6070P2	
F11	152-166	60	.210	2,100,000	230 (70)	193.0 (9240)	78 (25.4)	3	B	RH6070P3	

TABLE I.- Continued.
c) Rectangular Ogive ($\alpha=90°$)

Run No.	Tunnel Serial No.	α deg	Mach No.	Reynolds No.	V ft/s (m/s)	q lb/ft² (N/m²)	Temp °F (°C)	p atm	$\Omega b/2V$ Schedule	Pressure File Name	Remarks
B40	649-661	90	.024	102,000	26 (8)	1.0 (48)	48 (8.9)	1	A* w/o +.10	RO_A90_V8	No #7 & #8 Pressure Modules
F29	434-448	90	.105	178,000	115 (35)	8.2 (393)	80 (26.8)	.5	A	RO9035P5	
B39	633-647	90	.060	209,000	66 (20)	5.1 (245)	45 (7.2)	1	A	RO_A90_V20	No #7 & #8 Pressure Modules
B38	617-631	90	.090	323,000	98 (30)	11.9 (569)	45 (7.2)	1	A	RO_A90_V30	No #7 & #8 Pressure Modules
F30	450-464	90	.210	350,000	230 (70)	32.6 (1561)	82 (27.7)	.5	B	RO9070P5	
F27	402-416	90	.105	401,000	115 (35)	17.2 (824)	80 (26.4)	1	A	RO9035P1	
B34	553-567	90	.120	419,000	131 (40)	20.5 (983)	48 (9.1)	1	B*	RO_A90_V40	No #7 & #8 Pressure Modules
B35	569-583	90	.151	521,000	164 (50)	32.0 (1530)	44 (6.7)	1	B*	RO_A90_V50	No #7 & #8 Pressure Modules
B37	601-615	90	.181	639,000	197 (60)	47.0 (2250)	46 (7.6)	1	B**	RO_A90_V60	No #7 & #8 Pressure Modules
F28	418-432	90	.210	700,000	230 (70)	64.6 (3093)	82 (27.5)	1	B	RO9070P1	
B36	585-599	90	.212	730,000	230 (70)	62.7 (3000)	46 (7.6)	1	B	RO_A90_V70	No #7 & #8 Pressure Modules
F25	370-384	90	.105	769,000	115 (35)	33.1 (1585)	80 (26.9)	2	A	RO9035P2	
F23	340-354	90	.105	1,142,000	115 (35)	49.1 (2351)	79 (26.1)	3	A	RO9035P3	$\Omega b/2V=\pm.22$ Bad Pressure Data
F26	386-400	90	.210	1,503,000	230 (70)	129.0 (6177)	82 (27.6)	2	B	RO9070P2	
F24	356-368	90	.210	2,237,000	230 (70)	191.3 (9159)	80 (26.9)	3	B w/o ±.22	RO9070P3	

TABLE I.- Continued.
d) Rectangular Ogive (α=60°)

Run No.	Tunnel Serial No.	α deg	Mach No.	Reynolds No.	V ft/s (m/s)	q lb/ft² (N/m²)	Temp °F (°C)	p atm	Ωb/2V Schedule	Pressure File Name	Remarks
B31	504-515	60	.025	87,000	26 (8)	0.9 (41)	47 (8.3)	1	A* w/o ±.10	RO_A60_V8	No #7 & #8 Pressure Modules
F39	590-604	60	.105	175,000	115 (35)	8.3 (397)	76 (24.4)	.5	A	RO6035P5	
B26	423-437	60	.060	209.000	66 (20)	5.1 (245)	47 (8.3)	1	A	RO_A60_V20	No #7 & #8 Pressure Modules
B27	439-453	60	.090	318,000	98 (30)	11.7 (560)	47 (8.3)	1	A	RO_A60_V30	No #7 & #8 Pressure Modules
F37	558-572	60	.105	350,000	115 (35)	16.0 (766)	76 (24.5)	1	A	RO6035P1	.
F40	606-620	60	.210	350,000	230 (70)	32.3 (1547)	76 (24.4)	.5	B	RO6070P5	
B28	455-469	60	.121	420,000	131 (40)	20.6 (987)	47 (8.3)	1	B*	RO_A60_V40	No #7 & #8 Pressure Modules
B29	471-485	60	.151	521,000	164 (50)	32.0 (1530)	47 (8.3)	1	B*	RO_A60_V50	No #7 & #8 Pressure Modules
B30	487-501	60	.181	628,000	197 (60)	46.1 (2210)	47 (8.3)	1	B**	RO_A60_V60	No #7 & #8 Pressure Modules
F38	574-588	60	.210	692,000	230 (70)	64.7 (3098)	79 (26.3)	1	B	RO6070P1	
F35	526-540	60	.105	713,000	115 (35)	33.1 (1585)	78 (25.6)	2	A	RO6035P2	
B32	516-531	60	.210	730,000	230 (70)	62.7 (3000)	52 (10.9)	1	B w/o +.15	RO_A60_V70	No #7 & #8 Pressure Modules
F33	494-508	60	.105	1,080,000	115 (35)	49.6 (2375)	79 (25.9)	3	A	RO6035P3	
F36	542-556	60	.210	1,400,000	230 (70)	129.6 (6205)	80 (26.7)	2	B	RO6070P2	
F34	510-524	60	.210	2.090.000	230 (70)	195.6 (9365)	82 (27.9)	3	B	RO6070P3	

TABLE I.- Continued.
e) Circular Hemisphere (α=90°)

Run No.	Tunnel Serial No.	α deg	Mach No.	Reynolds No.	V ft/s (m/s)	q lb/ft² (N/m²)	Temp °F (°C)	p atm	Ωb/2V Schedule	Pressure File Name	Remarks
B48	774-786	90	.024	87,000	26 (8)	0.9 (41)	46 (7.5)	1	C	CH_A90_V8	No #7 & #8 Pressure Modules
B47	758-772	90	.060	207,000	66 (20)	5.1 (243)	46 (7.5)	1	A	CH_A90_V20	No #7 & #8 Pressure Modules
B46	742-756	90	.090	323,000	98 (30)	11.9 (568)	46 (7.5)	1	A	CH_A90_30R	No #7 & #8 Pressure Modules
F55	839-853	90	.105	350,000	115 (35)	16.1 (771)	79 (25.9)	1	A	CH9035P1	Pressure Module #8 Bad
B42	679-693	90	.120	424,000	131 (40)	20.8 (995)	46 (7.5)	1	B* w/o +.15	CH_A90_V40	No #7 & #8 Pressure Modules
B43	695-709	90	.150	521,000	164 (50)	32.0 (1530)	46 (7.5)	1	B*	CH_A90_V50	No #7 & #8 Pressure Modules
B44	711-724	90	.180	636,000	197 (60)	46.8 (2240)	46 (7.5)	1	B** w/o -.025	CH_A90_V60	No #7 & #8 Pressure Modules
F53	806-821	90	.105	704,000	115 (35)	32.6 (1561)	79 (26.3)	2	A	CH9035P2	Pressure Module #8 Bad
B45	726-740	90	.210	730,000	230 (70)	62.7 (3000)	46 (7.5)	1	B	CH_A90_V70	No #7 & #8 Pressure Modules
F56	855-869	90	.210	758,000	230 (70)	63.3 (3031)	81 (27.1)	1	B	CH9070P1	Pressure Module #8 Bad
F51	776-790	90	.105	1,060,000	115 (35)	49.2 (2356)	79 (26.1)	3	A	CH9035P3	Pressure Module #8 Bad
F54	823-837	90	.210	1,380,000	230 (70)	127.8 (6119)	82 (27.6)	2	B	CH9070P2	Pressure Module #8 Bad
F52	791-804	90	.210	2,075,000	230 (70)	192.0 (9193)	82 (28.0)	3	B	CH9070P3	Pressure Module #8 Bad

TABLE I.- Continued.
f) Circular Hemisphere (α=60°)

Run No.	Tunnel Serial No.	α deg	Mach No.	Reynolds No.	V ft/s (m/s)	q lb/ft² (N/m²)	Temp °F (°C)	p atm	Ωb/2V Schedule	Pressure File Name	Remarks
B57	925-937	60	.024	96,000	26 (8)	0.9 (41)	51 (10.6)	1	A*	CH_A60_V8	No #7 & #8 Pressure Modules
B56	908-922	60	.060	207,000	66 (20)	5.2 (248)	51 (10.6)	1	A	CH_A60_V20	No #7 & #8 Pressure Modules
B51	828-842	60	.090	323,000	98 (30)	11.8 (566)	48 (8.8)	1	A	CH_A60_V30	No #7 & #8 Pressure Modules
F47	716-730	60	.105	350,000	115 (35)	16.3 (780)	79 (26.2)	1	A		No Pressure Data Taken
B52	844-858	60	.120	424,000	131 (40)	20.8 (995)	48 (8.8)	1	B*	CH_A60_V40	No #7 & #8 Pressure Modules
B53	860-874	60	.151	525,000	164 (50)	32.1 (1535)	48 (8.8)	1	B*	CH_A60_V50	No #7 & #8 Pressure Modules
B54	876-890	60	.181	636,000	197 (60)	47.0 (2248)	48 (8.8)	1	B** w/o +.15	CH_A60_V60	No #7 & #8 Pressure Modules
F48	732-746	60	.210	687,000	230 (70)	64.3 (3078)	81 (27.4)	1	B		No Pressure Data Taken
F45	683-698	60	.105	712,000	115 (35)	32.7 (1565)	79 (26.2)	2	A		No Pressure Data Taken
B55	892-906	60	.210	730,000	230 (70)	62.7 (3000)	51 (10.6)	1	B	CH_A60_V70	No #7 & #8 Pressure Modules
F43	650-663	60	.105	1,065,000	115 (35)	49.4 (2365)	78 (25.3)	3	A	CH6035P3	
F46	700-714	60	.210	1,350,000	230 (70)	129.0 (6176)	82 (27.8)	2	B		No Pressure Data Taken
F44	666-682	60	.210	2,070,000	230 (70)	194.2 (9298)	83 (28.1)	3	B w/-.036	CH6070P3	

TABLE I.- Continued.
g) Circular Ogive (α=90°)

Run No.	Tunnel Serial No.	α deg	Mach No.	Reynolds No.	V ft/s (m/s)	q lb/ft² (N/m²)	Temp °F (°C)	p atm	Ωb/2V Schedule	Pressure File Name	Remarks
B67	1090-1104	90	.090	321.000	98 (30)	11.9 (568)	49 (9.5)	1	A	CO_A90_V30	No #7 & #8 Pressure Modules
F63	963-977	90	.105	350,000	115 (35)	16.0 (766)	78 (25.4)	1	A	CO9035P1	
B68	1106-1120	90	.120	423,000	131 (40)	20.8 (994)	49 (9.5)	1	B* w/o -.3	CO_A90_V40	No #7 & #8 Pressure Modules
B69	1123-1137	90	.150	526,000	164 (50)	32.2 (1543)	49 (9.5)	1	B*	CO_A90_V50	No #7 & #8 Pressure Modules
F64	979-993	90	.210	690,000	230 (70)	62.8 (3007)	77 (25.0)	1	B	CO9070P1	
F61	931-945	90	.105	710,000	115 (35)	33.1 (1585)	78 (25.6)	2	A	CO9035P2	
F59	899-913	90	.105	1,060,000	115 (35)	49.3 (2361)	78 (25.4)	3	A	CO9035P3	
F62	947-961	90	.210	1,380,000	230 (70)	129.1 (6181)	79 (26.0)	2	B	CO9070P2	
F60	915-929	90	.210	2,080,000	230 (70)	193.0 (9241)	79 (26.3)	3	B	CO9070P3	

TABLE I.- Continued.
h) Circular Ogive (α=70°, 60°)

Run No.	Tunnel Serial No.	α deg	Mach No.	Reynolds No.	V ft/s (m/s)	q lb/ft² (N/m²)	Temp °F (°C)	P atm	Ωb/2V Schedule	Pressure File Name	Remarks
F91	1402-1416	70	.105	350,000	115 (35)	16.7 (800)	68 (20.2)	1	A	CO7035P1	
F92	1418-1432	70	.210	710,000	230 (70)	63.0 (3016)	70 (21.0)	1	B	CO7070P1	
B65	1056-1068	60	.024	89,000	26 (8)	0.9 (42)	52 (11.3)	1	A*	CO_A60_V8	No #7 & #8 Pressure Modules
B64	1040-1054	60	.060	211,000	66 (20)	5.2 (248)	54 (12.0)	1	A	CO_A60_V20	No #7 & #8 Pressure Modules
B58	939-953	60	.090	323,000	98 (30)	11.9 (568)	48 (11.2)	1	A	CO_A60_V30	No #7 & #8 Pressure Modules
F71	1087-1101	60	.105	350,000	115 (35)	16.0 (766)	73 (23.0)	1	A	CO6035P1	
B59	955-969	60	.120	423,000	131 (40)	20.7 (993)	52 (11.3)	1	B*	CO_A60_V40	No #7 & #8 Pressure Modules
B60	971-985	60	.150	523,000	164 (50)	32.1 (1535)	52 (11.3)	1	B*	CO_A60_V50	No #7 & #8 Pressure Modules
B61	987-1001	60	.180	638,000	197 (60)	47.0 (2248)	53 (11.6)	1	B**	CO_A60_V60	No #7 & #8 Pressure Modules
F72	1103-1117	60	.210	690,000	230 (70)	62.3 (2983)	75 (24.0)	1	B	CO6070P1	
F69	1054-1069	60	.105	703,000	115 (35)	33.2 (1590)	73 (23.0)	2	A	CO6035P2	
B62	1003-1017	60	.210	730,000	230 (70)	62.7 (3000)	54 (12.0)	1	B	CO_A60_V70	No #7 & #8 Pressure Modules
F67	1023-1037	60	.105	1,080,000	115 (35)	49.7 (2380)	75 (24.0)	3	A	CO6035P3	
F70	1071-1085	60	.210	1,400,000	230 (70)	129.0 (6176)	75 (24.0)	2	B	CO6070P2	
F68	1039-1053	60	.210	2,080,000	230 (70)	191.0 (9145)	79 (26.0)	3	B	CO6070P3	

TABLE I.- Continued.
i) Circular Ogive + Trip Strips (α=60°)

Run No.	Tunnel Serial No.	α deg	Mach No.	Reynolds No.	V ft/s (m/s)	q lb/ft² (N/m²)	Temp °F (°C)	p atm	Ωb/2V Schedule	Pressure File Name	Remarks
F73	1119-1133	60	.105	350,000	115 (35)	16.1 (770)	72 (22.0)	1	A	COt60351	
F77	1183-1197	60	.105	703,000	115 (35)	32.8 (1571)	70 (21.1)	2	A	COt60352	
F74	1135-1149	60	.210	736,000	230 (70)	63.0 (3016)	73 (23.0)	1	B	COt60701	
F76	1167-1181	60	.105	1,070,000	115 (35)	47.6 (2279)	74 (23.1)	3	A	COt60353	
F78	1199-1213	60	.210	1,410,000	230 (70)	128.2 (6138)	73 (23.0)	2	B	COt60702	
F75	1151-1165	60	.210	2,100,000	230 (70)	193.5 (9264)	75 (24.0)	3	B	COt60703	

TABLE I.- Concluded.
j) Circular Ogive + Strakes (α=70°, 60°)

Run No.	Tunnel Serial No.	α deg	Mach No.	Reynolds No.	V ft/s (m/s)	q lb/ft² (N/m²)	Temp °F (°C)	p atm	Ωb/2V Schedule	Pressure File Name	Remarks
F89	1370-1384	70	.105	350,000	115 (35)	16.8 (804)	68 (20.0)	1	A	COs70351	
F90	1386-1400	70	.210	700,000	230 (70)	64.2 (3074)	70 (21.0)	1	B	COs70701	
F85	1310-1323	60	.105	180,000	115 (35)	8.2 (393)	70 (21.0)	.5	A w/o -.2	COs60355	
F86	1326-1339	60	.210	350,000	230 (70)	31.7 (1518)	70 (21.0)	.5	B w/o -.22	COs60705	
F83	1278-1292	60	.105	360,000	115 (35)	15.9 (761)	70 (21.0)	1	A	COs60351	
F81	1246-1260	60	.105	700,000	115 (35)	34.0 (1628)	70 (21.1)	2	A	COs60352	
F84	1294-1308	60	.210	710,000	230 (70)	63.9 (3059)	72 (22.0)	1	B	COs60701	
F79	1215-1229	60	.105	1,070,000	115 (35)	49.5 (2370)	70 (21.3)	3	A	COs60353	
F82	1262-1276	60	.210	1,400,000	230 (70)	129.8 (6215)	73 (22.6)	2	B	COs60702	
F80	1231-1244	60	.210	2,100,000	230 (70)	195.8 (9375)	72 (22.4)	3	B	COs60703	

Ωb/2V Schedules:
A: 0.0, ±.050, ±.075, ±.100, ±.150, ±.200, ±.300, ±.400
A*: 0.0, ±.100, ±.150, ±.200, ±.250, ±.300, ±.400
B: 0.0, ±.025, ±.050, ±.075, ±.100, ±.150, ±.200, ±.225
B*: 0.0, ±.025, ±.050, ±.075, ±.100, ±.150, ±.200, ±.300
B**: 0.0, ±.025, ±.050, ±.075, ±.100, ±.150, ±.200, ±.250
C: 0.0, ±.100, ±.200, ±.250, ±.300, ±.350, ±.480
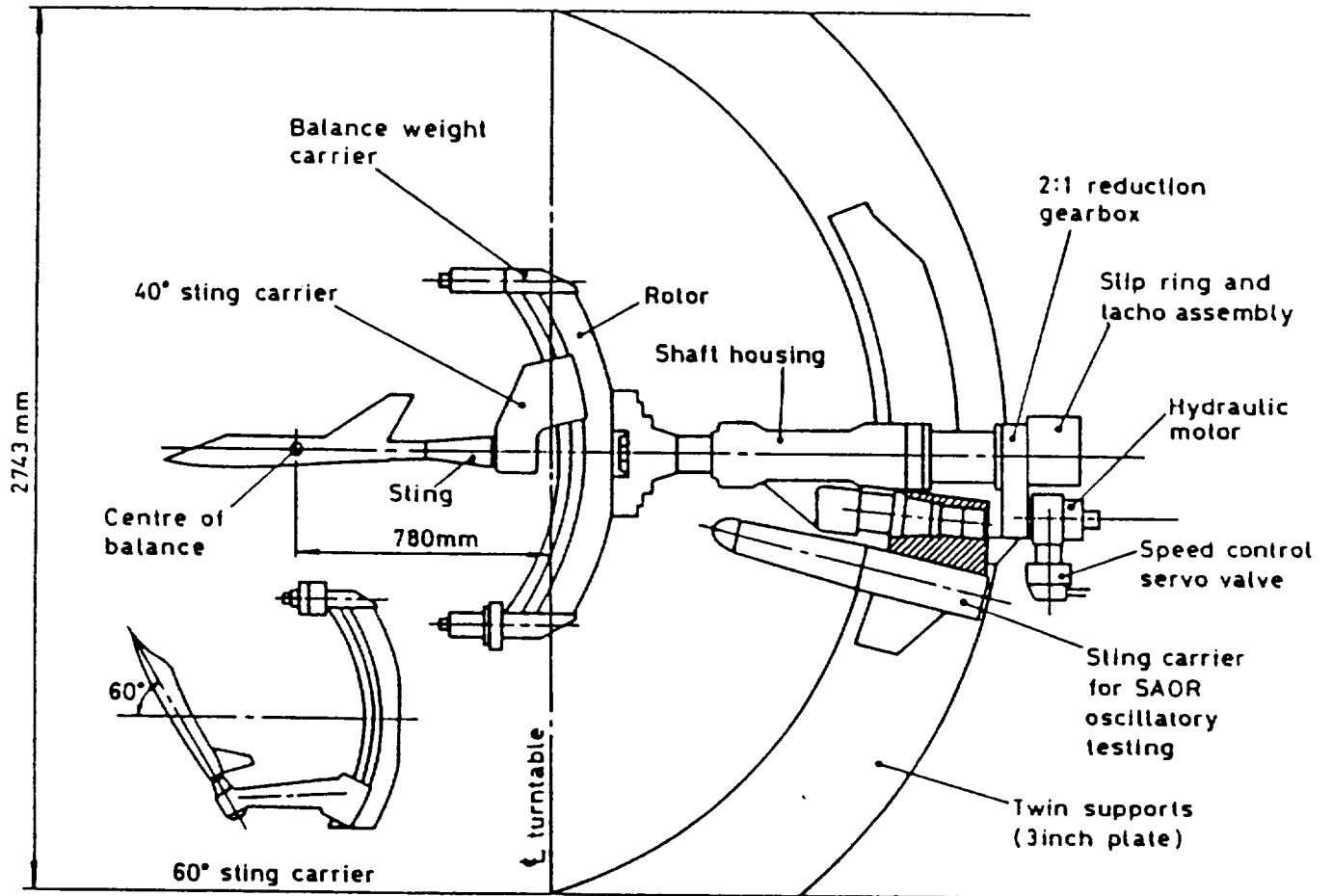
Figure 1. Diagram of rotary balance apparatus.
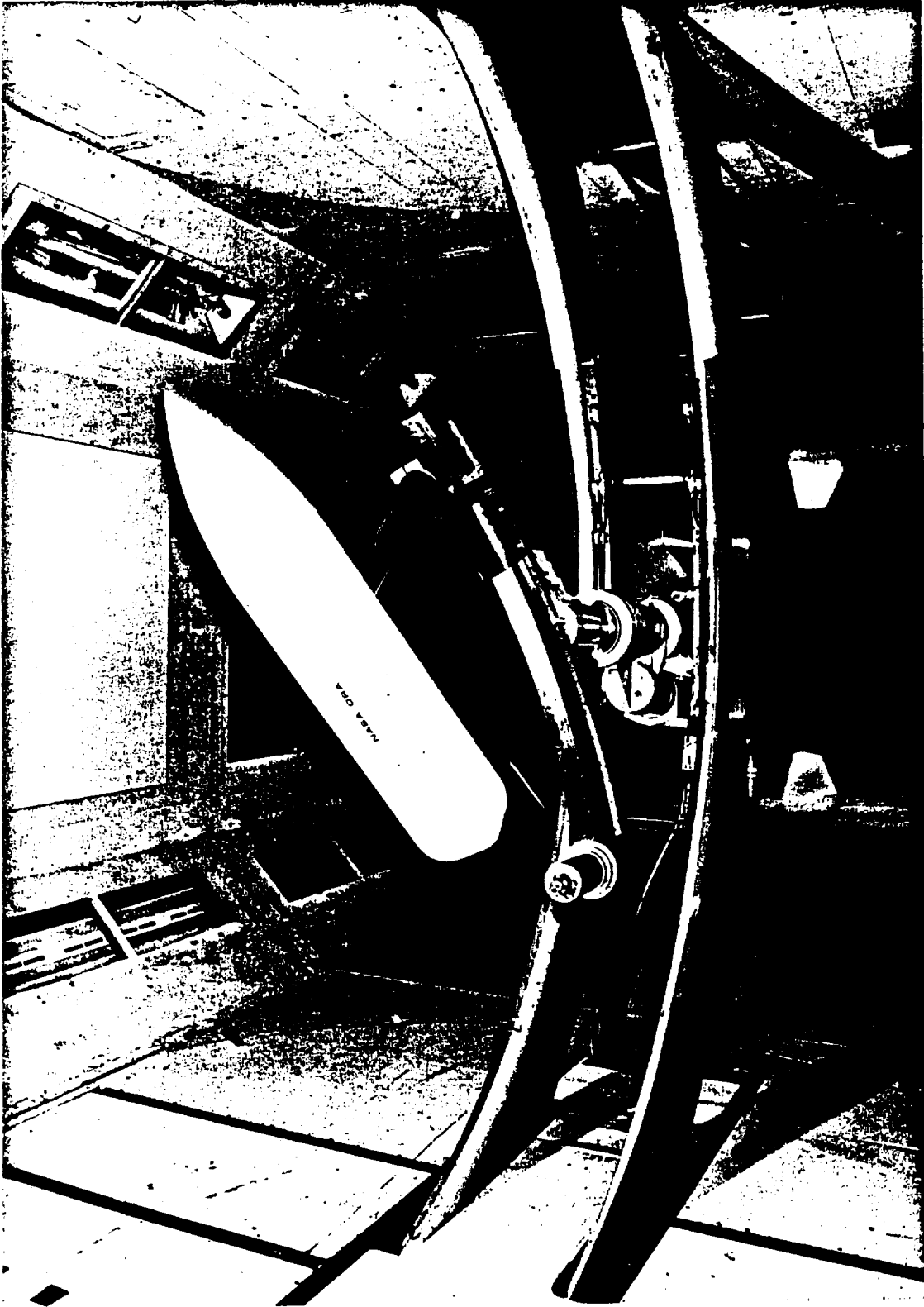
Figure 2. Photograph of rectangular ogive forebody mounted on rotary rig in DRA 13-ft x 9 ft wind tunnel.

F-2
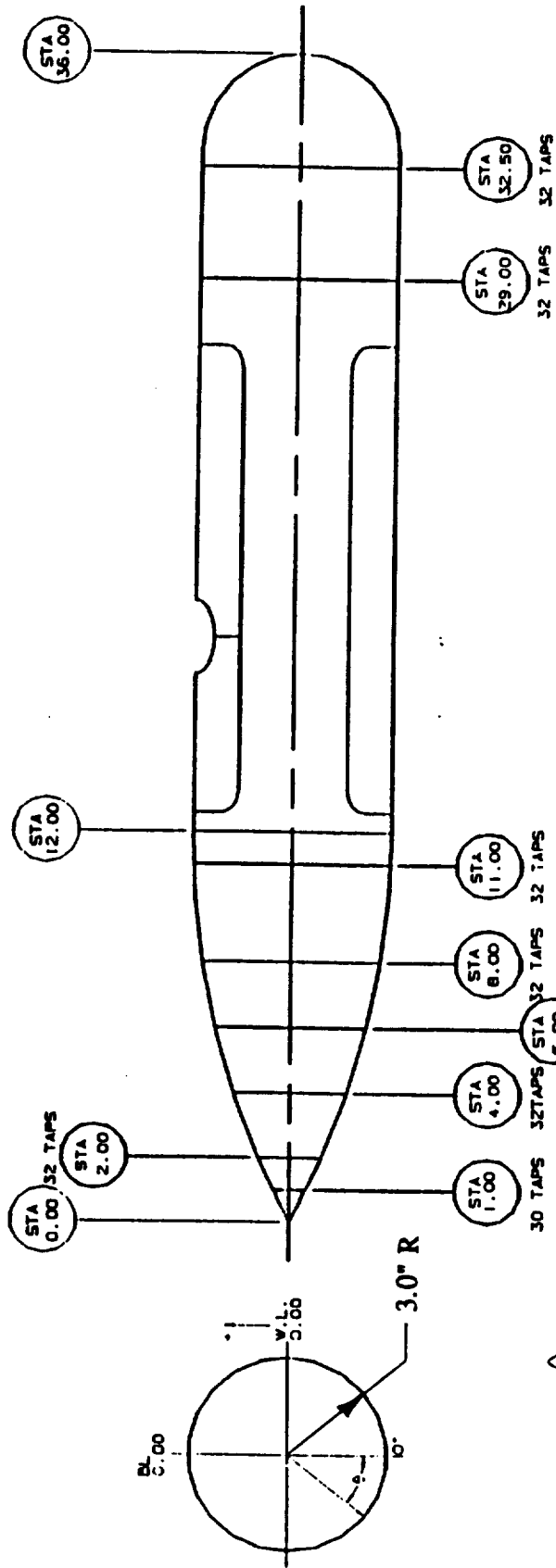
INSTRUMENTED CIRCULAR OGIVE (SHOWN)
-2 INSTRUMENTED CIRCULAR HEMISPHERE (SIMILAR)

STA 36.00

STA 32.50 — 32 TAPS

STA 29.00 — 32 TAPS

STA 12.00

STA 11.00 — 32 TAPS

STA 8.00 — 32 TAPS

STA 6.00 — 32 TAPS

STA 4.00 — 32 TAPS

STA 2.00 — 32 TAPS

STA 1.00 — 30 TAPS

STA 0.00

3.0" R

W.L. 0.00

BL 0.00

DETAIL
TYPICAL TUBE INSTALLATION

STATION 2.00, 4.00, 6.00, 8.00, 11.00, 29.00, 32.50

TAP #	THETA
31	0.000
32	11.250
33	22.500
34	33.750
35	45.000
36	56.250
37	67.500
38	78.750
39	90.000
40	101.250
41	112.500
42	123.750
43	135.000
44	146.250
45	157.500
46	168.750
47	180.000
48	191.250
49	202.500
50	213.750
51	225.000
52	236.250
53	247.500
54	258.750
55	270.000
56	281.250
57	292.500
58	303.750
59	315.000
60	326.250
61	337.500
62	348.750

STATION 1.00

TAP #	THETA
1	0.000
2	12.000
3	24.000
4	36.000
5	48.000
6	60.000
7	72.000
8	84.000
9	96.000
10	108.000
11	120.000
12	132.000
13	144.000
14	156.000
15	168.000
16	180.000
17	192.000
18	204.000
19	216.000
20	228.000
21	240.000
22	252.000
23	264.000
24	276.000
25	288.000
26	300.000
27	312.000
28	324.000
29	336.000
30	348.000

a) Circular ogive and hemisphere shapes.
Figure 3. Location of pressure ports on the models.

F-3

-3 INSTRUMENTED RECTANGULAR OGIVE (SHOWN)

-4 INSTRUMENTED RECTANGULAR HEMISPHERE (SIMILAR)

b) Rectangular ogive and hemisphere shapes.
Figure 3. Location of pressure ports on the models.

STATION 2.00, 4.00, 6.00, 8.00, 11.00, 29.00, 32.50	
TAP #	THETA
1	0.000
2	14.306
3	27.022
4	34.124
5	41.361
6	45.000
7	48.639
8	55.876
9	62.978
10	72.986
11	84.176
12	101.530
13	117.022
14	128.940
15	141.060
16	152.978
17	165.694
18	180.000
19	194.306
20	207.022
21	218.940
22	231.060
23	242.978
24	258.470
25	275.824
26	287.014
27	297.022
28	304.124
29	311.361
30	318.639
31	325.876
32	332.978
	345.694

STATION 1.00	
TAP #	THETA
1	0.000
2	14.306
3	27.022
4	35.925
5	45.000
6	54.075
7	62.978
8	72.986
9	84.176
10	101.530
11	117.022
12	128.940
13	141.060
14	152.978
15	165.694
16	180.000
17	194.306
18	207.022
19	218.940
20	231.060
21	242.978
22	258.470
23	275.824
24	287.014
25	297.022
26	305.925
27	315.000
28	324.075
29	332.978
30	345.694

0.014" dia.

0.001" shim stock

0.1"

0.007"

F-5

0°

80°

33.0 "
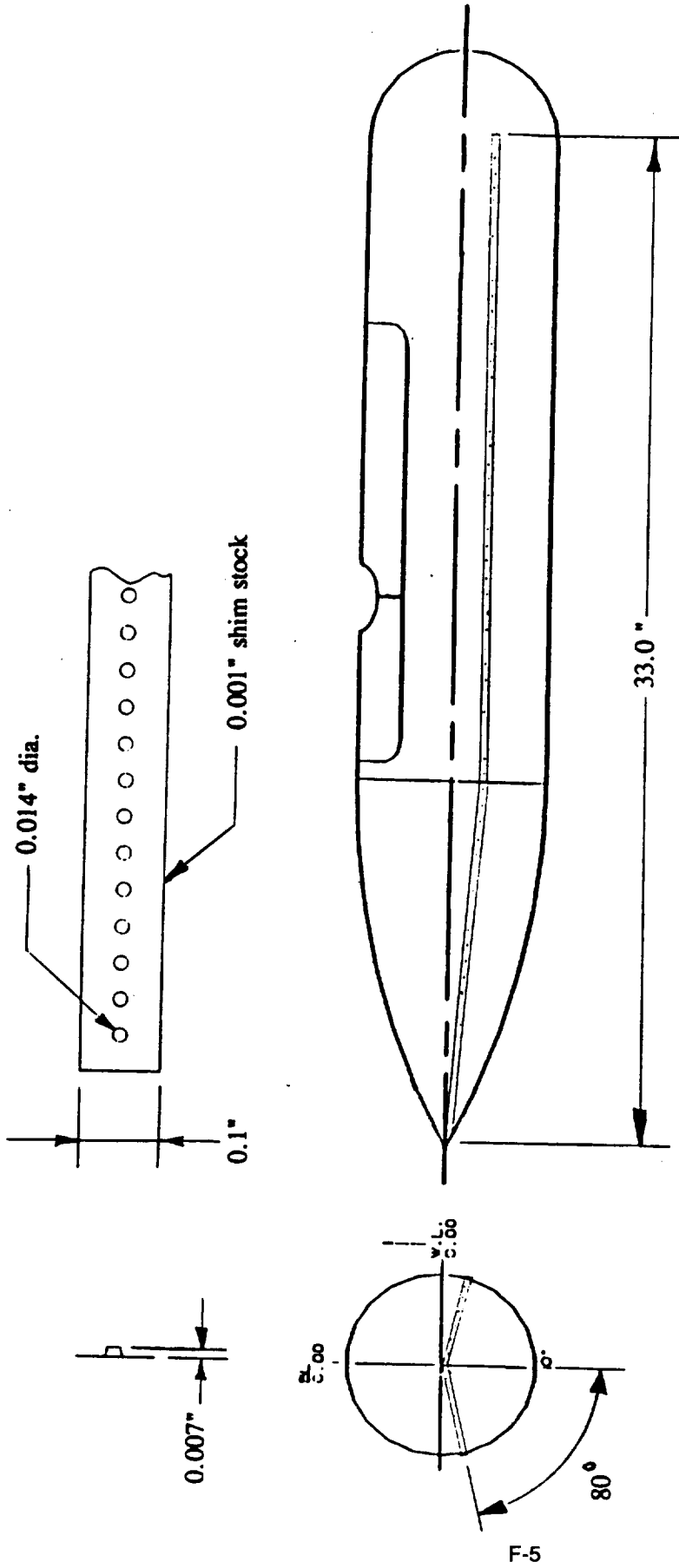
a) Trip Strips

Figure 4. Modifications made to the circular ogive model.

0.5"

4.0"

F-6

100°
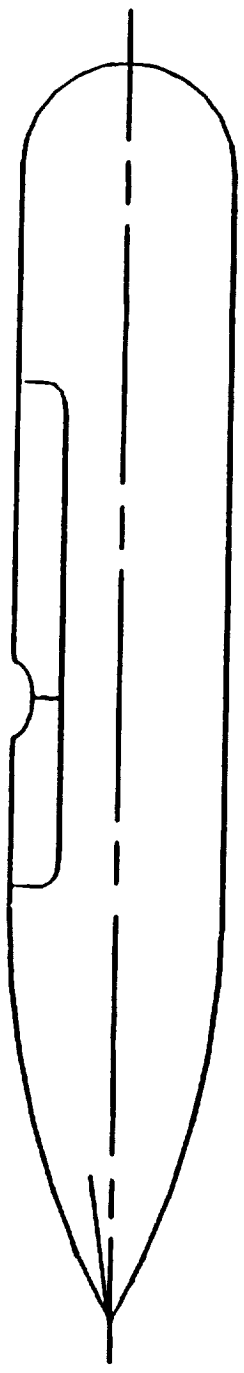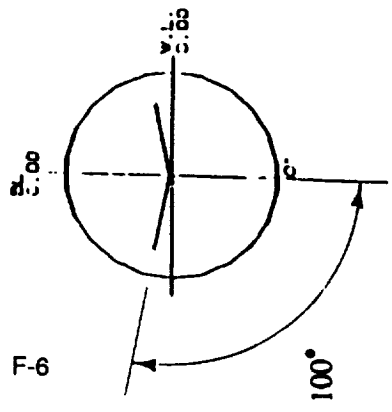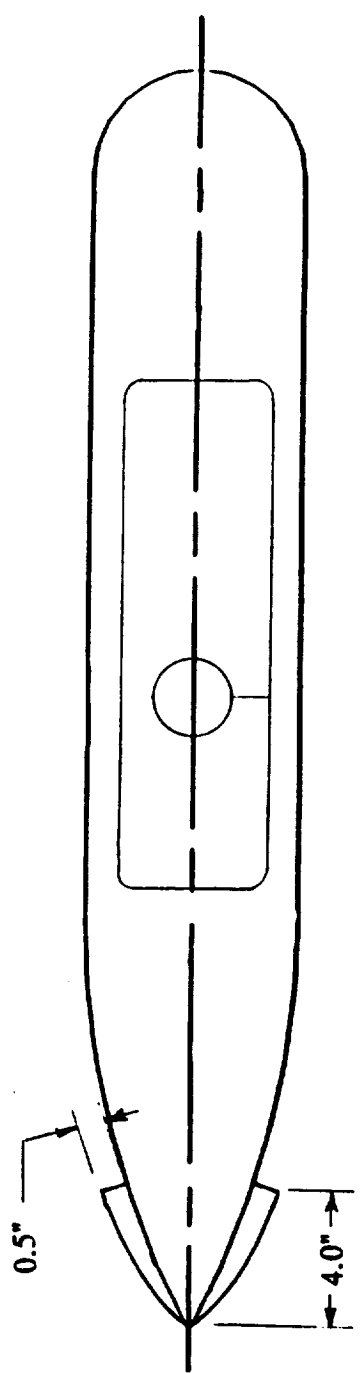
b) Strakes

Figure 4. Modifications made to the circular ogive model.
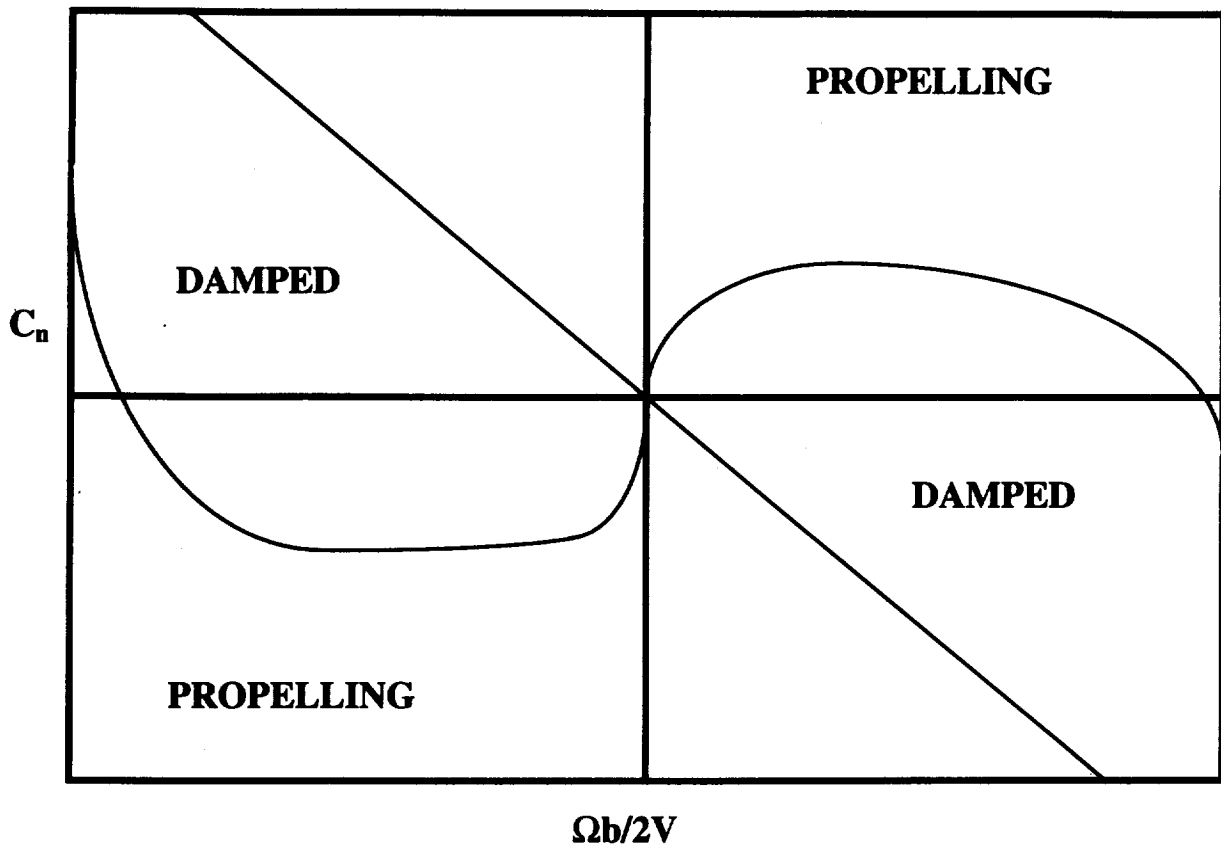
Figure 5. Illustration of damped and propelling quadrants for rotational yawing moments.
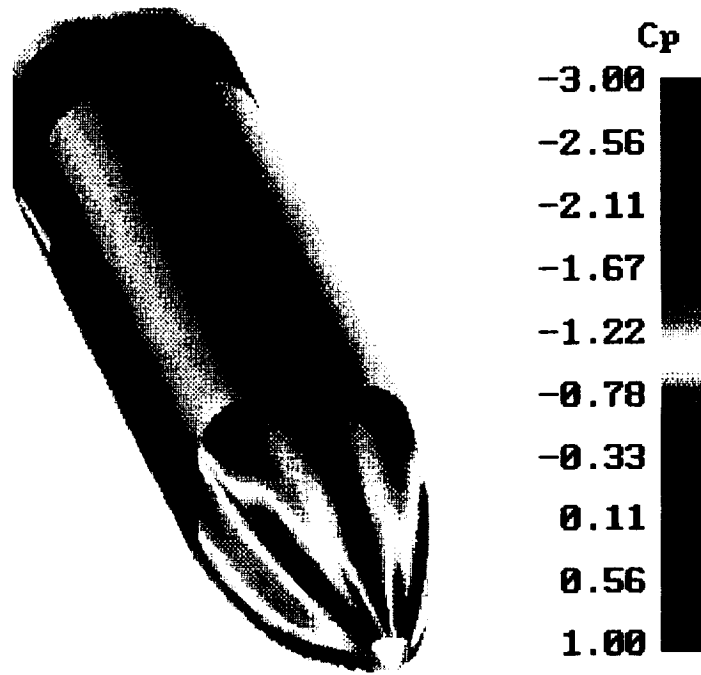
Figure 6. Color mapping of pressure data onto rectangular ogive model with surface shading.
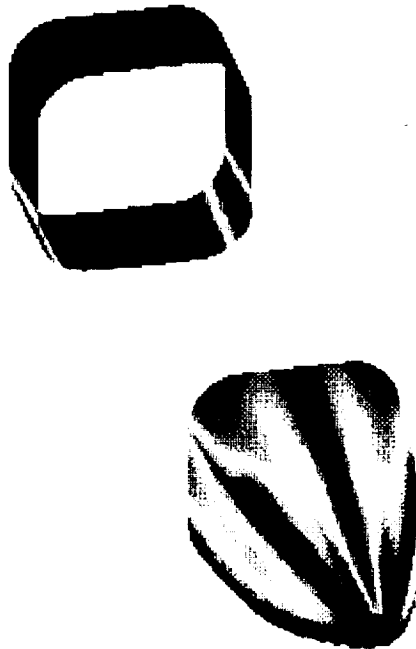
Figure 7. Color mapping of pressure data onto rectangular ogive with surface shading turned off.
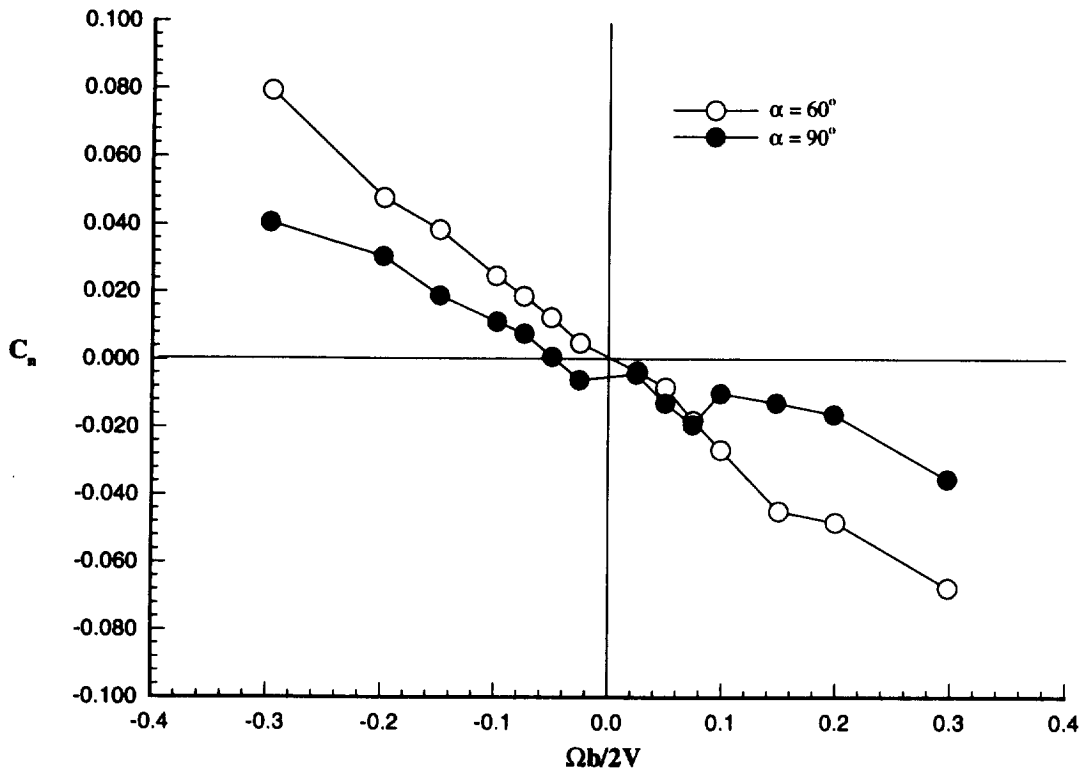
a) Yawing moment

Figure 8. Comparison of aerodynamic characteristics for rectangular ogive at $\alpha=60^{\circ}$ and $\alpha=90^{\circ}$
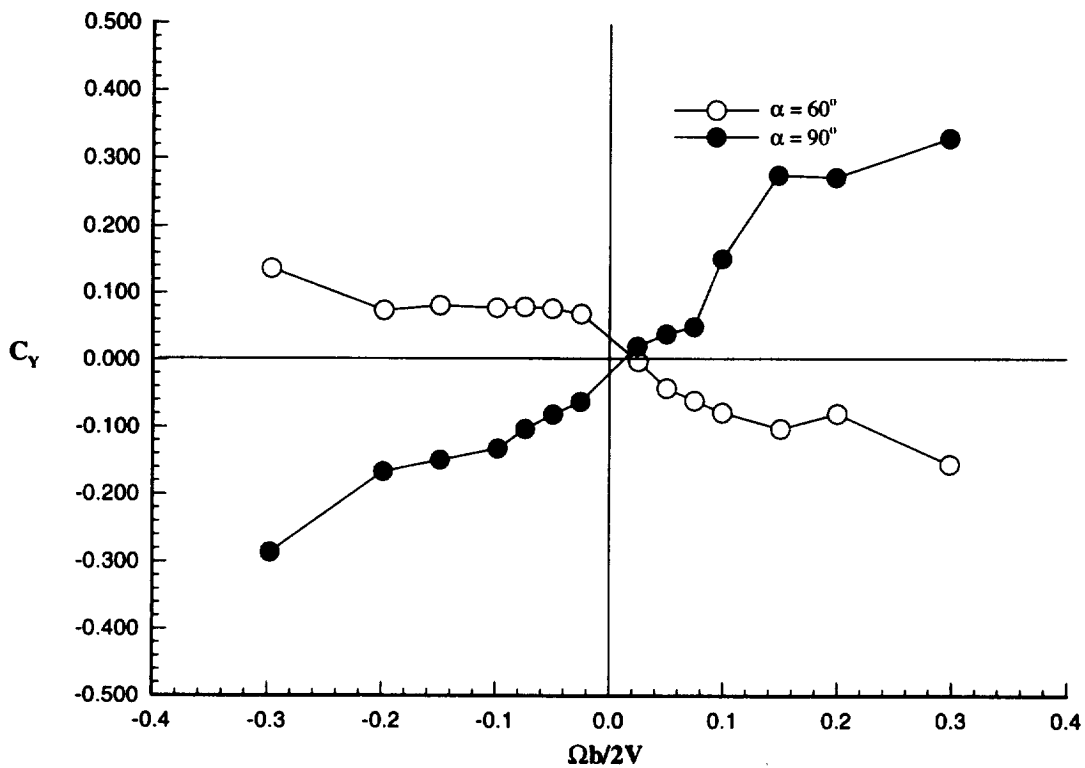
b) Side Force

Figure 8. Comparison of aerodynamic characteristics for rectangular ogive at $\alpha=60^{\circ}$ and $\alpha=90^{\circ}$
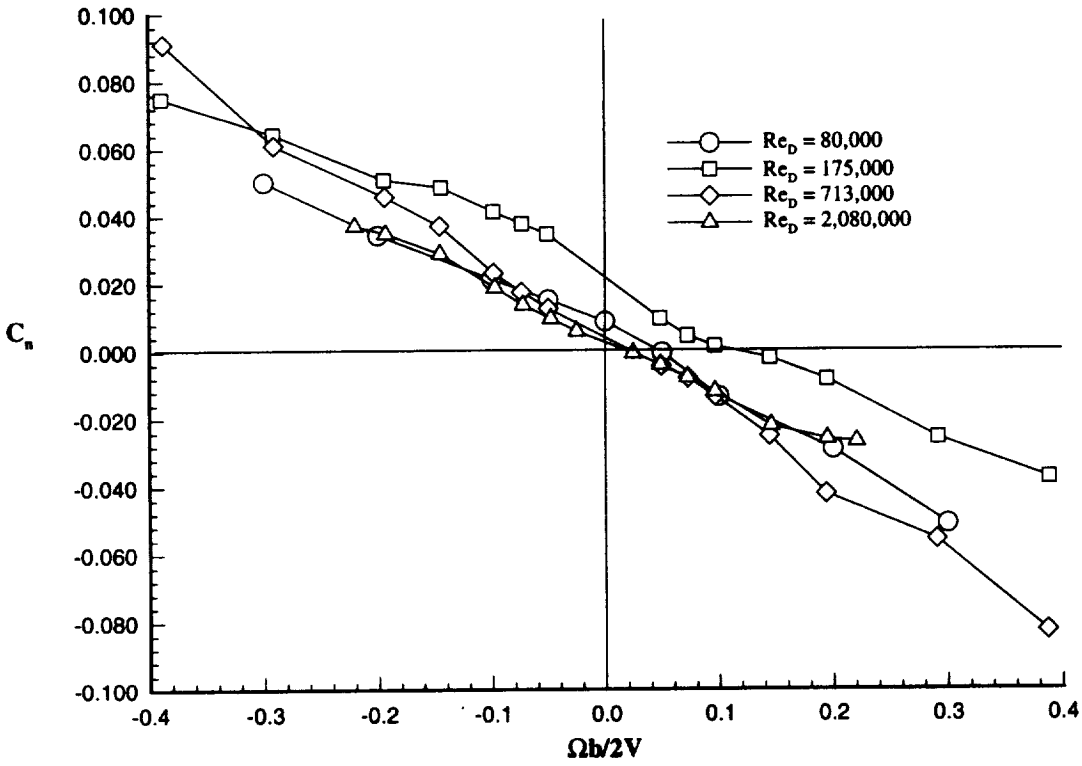
a) Yawing moment

Figure 9. Effect of rotation rate and Reynolds number on aerodynamic characteristics for rectangular ogive at 60° angle of attack
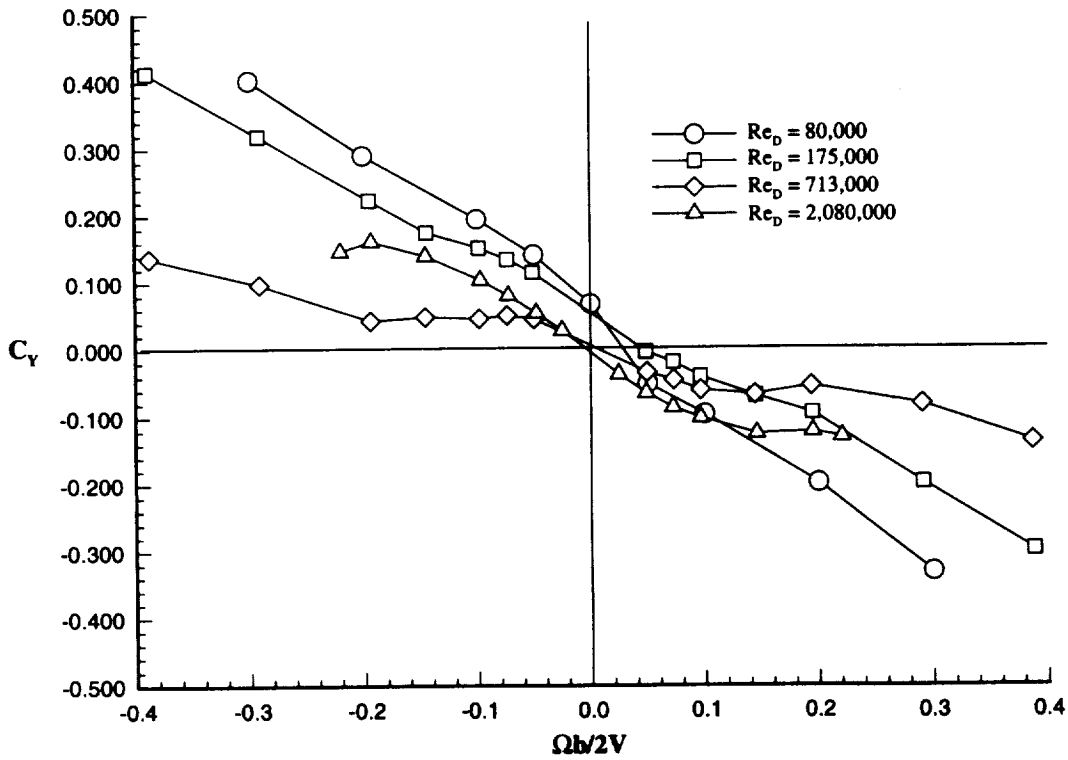
b) Side Force

Figure 9. Effect of rotation rate and Reynolds number on aerodynamic characteristics for rectangular ogive at 60° angle of attack

Cp
-3.00
-2.56
-2.11
-1.67
-1.22
-0.78
-0.33
0.11
0.56
1.00

a) $Re_D = 175,000$

b) $Re_D = 350,000$

c) $Re_D = 713,000$
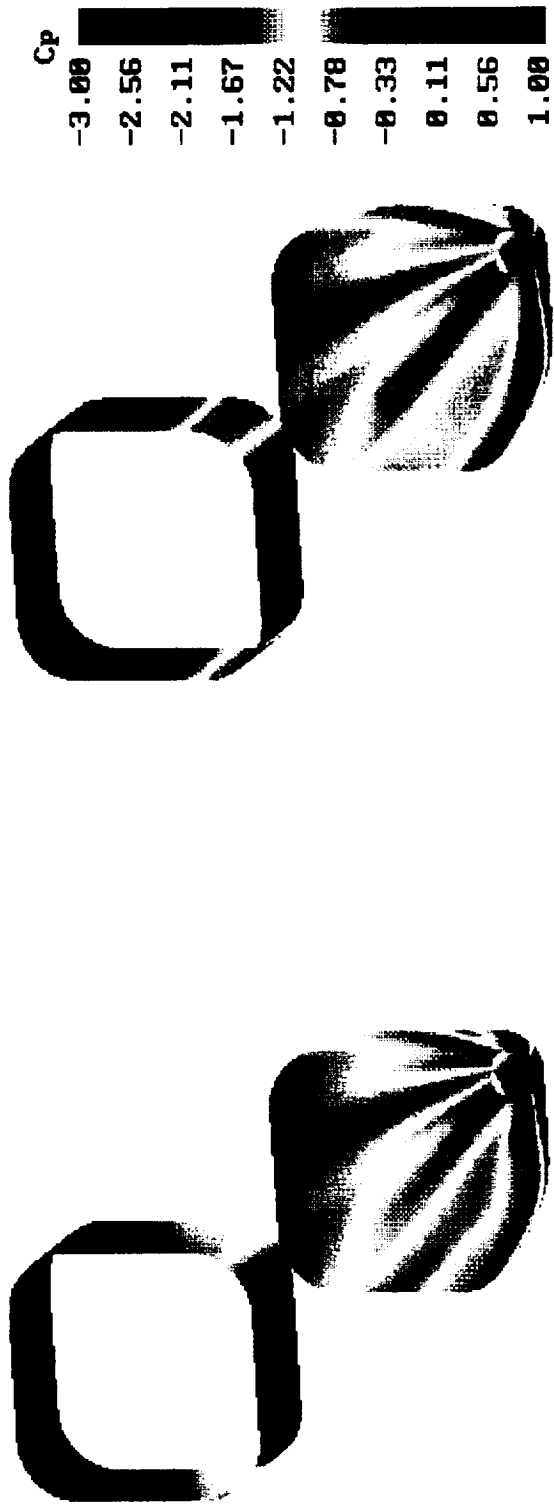
d) $Re_D = 2,090,000$

Figure 10. Pressure distribution for the rectangular ogive at 60° angle of attack for $\Omega b/2V=0.0$.
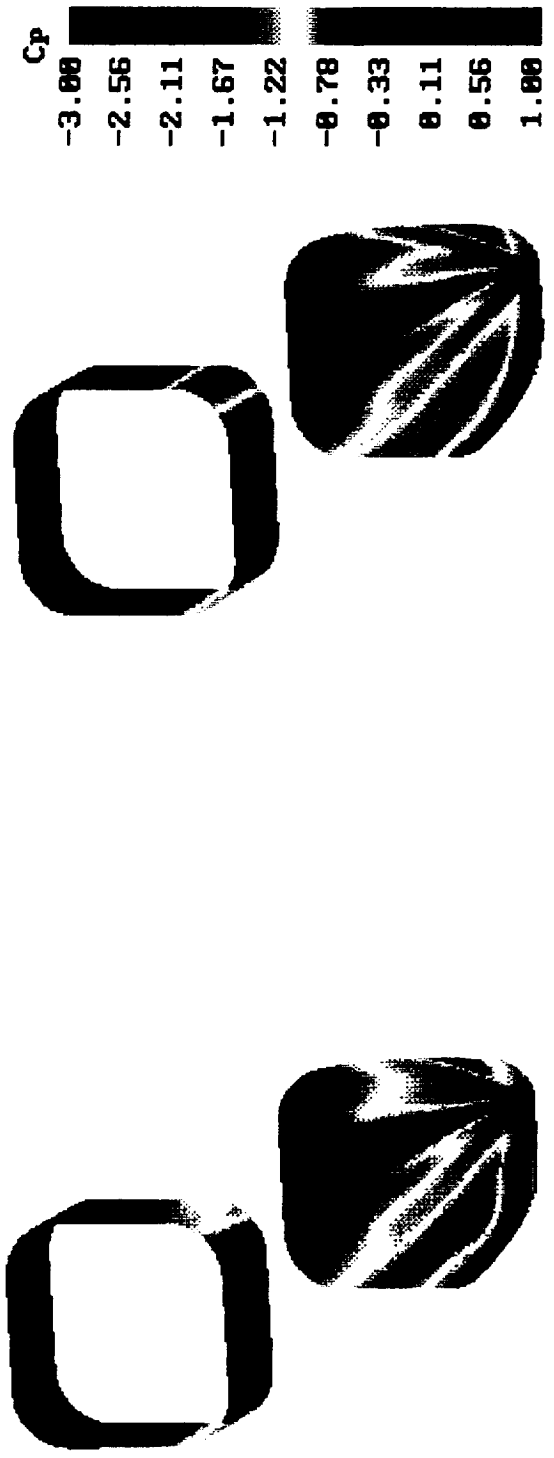
a) $Re_D = 175,000$

b) $Re_D = 350,000$
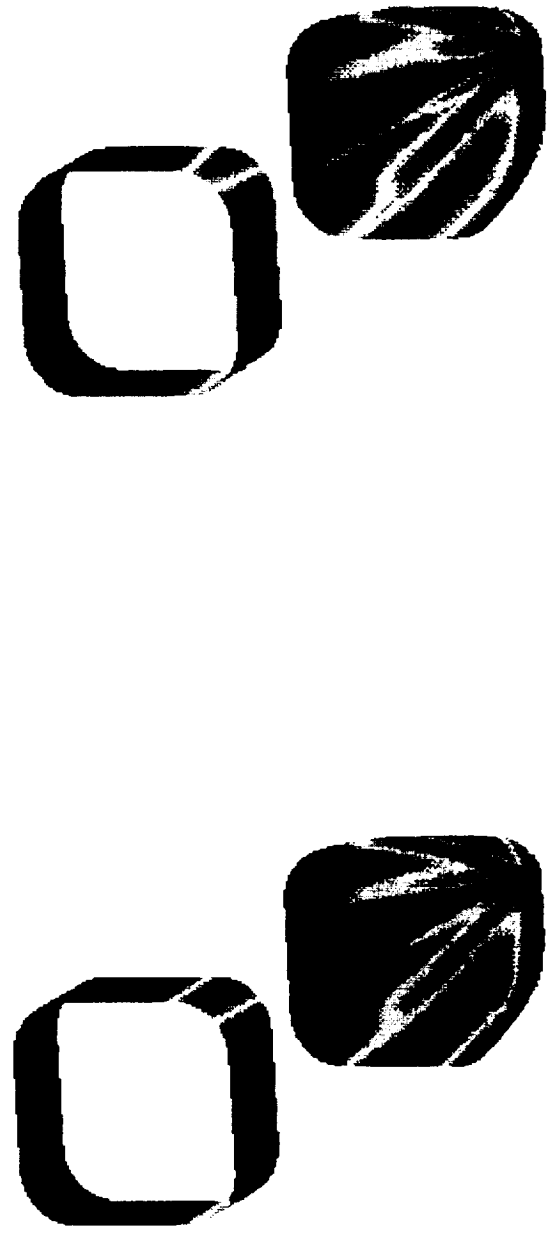
c) $Re_D = 713,000$

d) $Re_D = 2,090,000$

Figure 11. Pressure distribution for the rectangular ogive at 60° angle of attack for $\Omega b/2V = -0.1$.

Cp

-3.00
-2.56
-2.11
-1.67
-1.22
-0.78
-0.33
0.11
0.56
1.00

a) $Re_D = 175,000$

b) $Re_D = 350,000$

c) $Re_D = 713,000$

d) $Re_D = 2,090,000$

Figure 12. Pressure distribution for the rectangular ogive at 60° angle of attack for $\Omega b/2V = +0.1$.
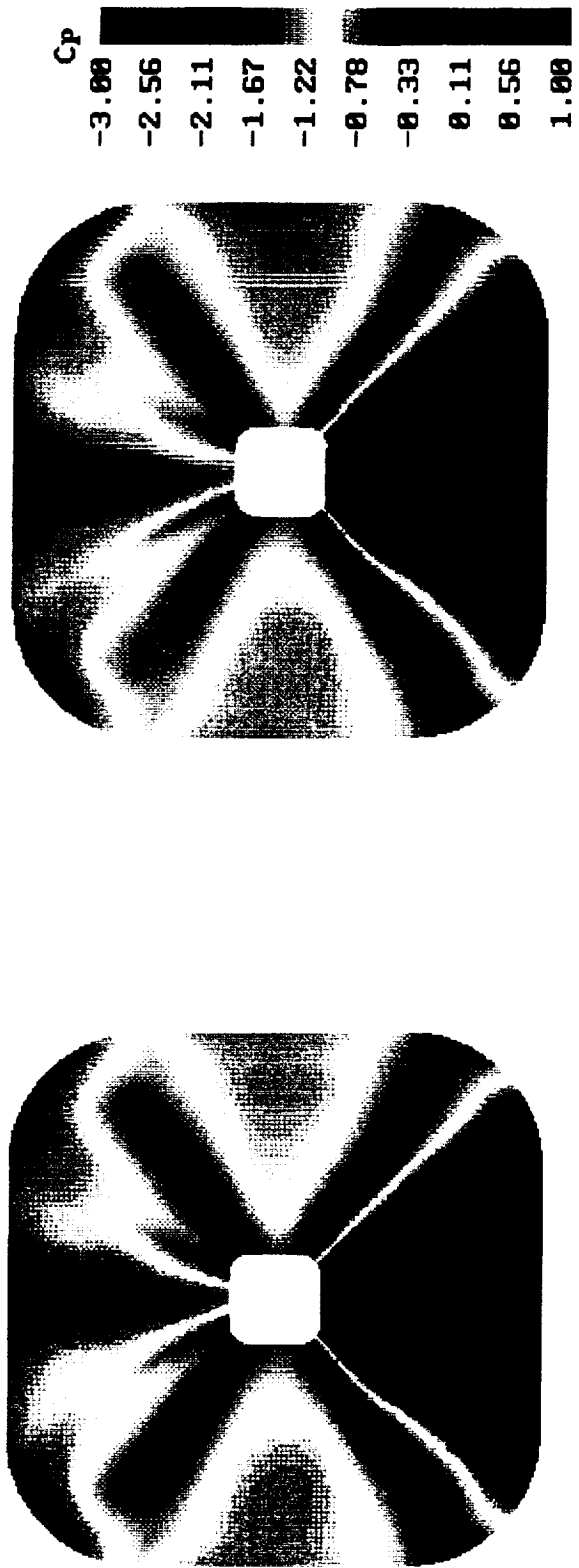
Figure 13. Effect of rotation on the pressure distribution for the rectangular ogive at 60° angle of attack and $Re_D = 2,090,000$.
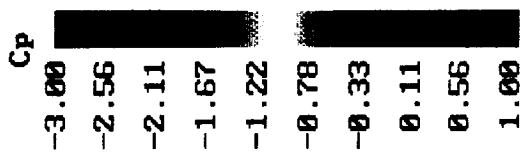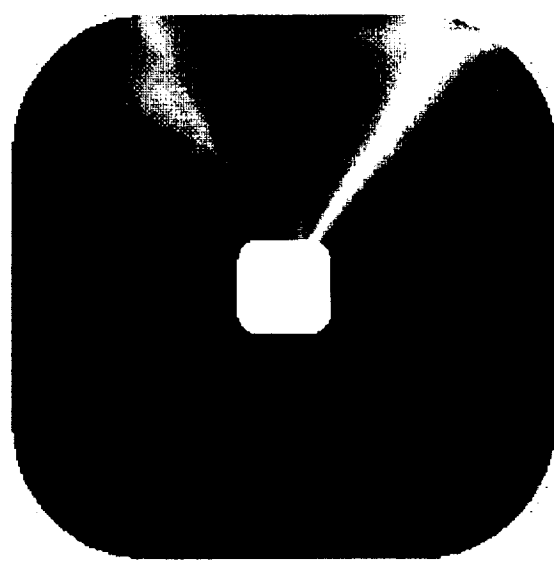
a) $\Omega b/2V = 0.0$

b) $\Omega b/2V = -.05$

c) $\Omega b/2V = -0.1$

d) $\Omega b/2V = -0.2$
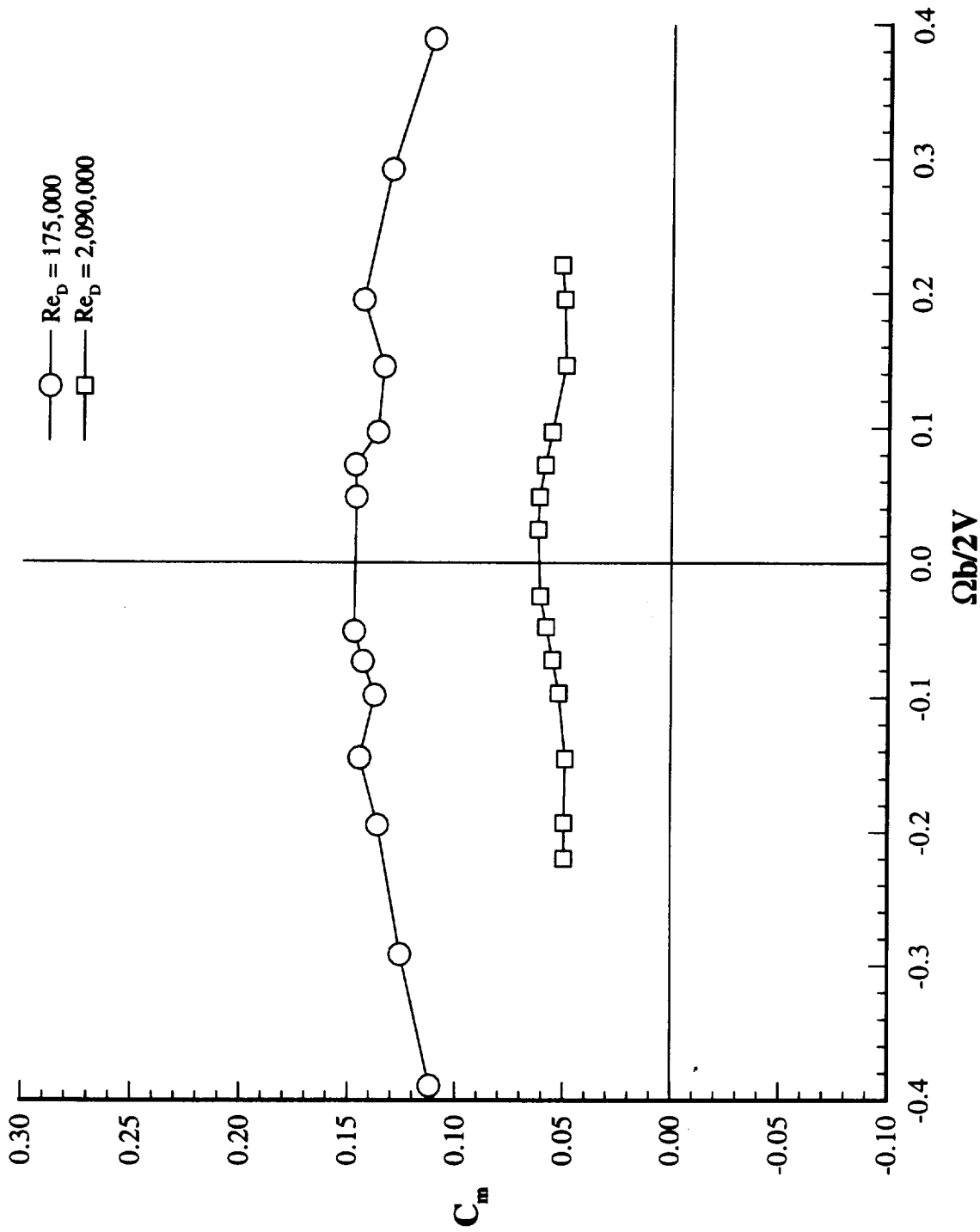
Figure 14. Effect of rotation rate and Reynolds number on pitching moment characteristics for the rectangular ogive at 60° angle of attack
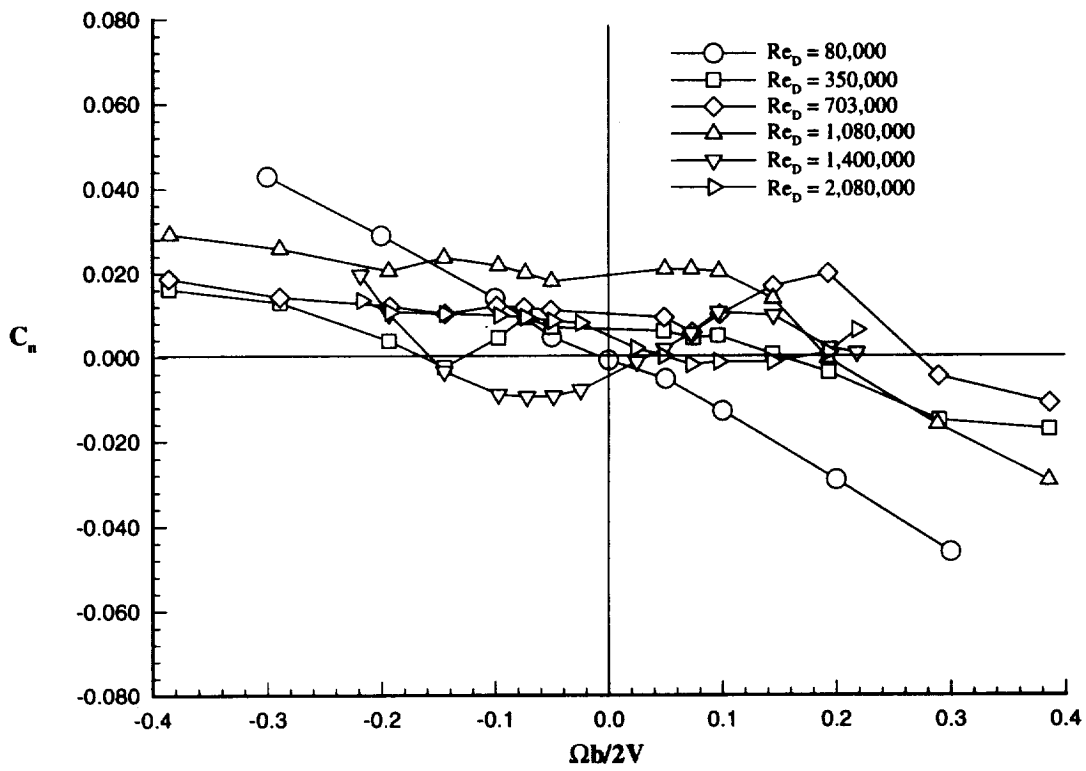
a) Yawing moment

Figure 15. Effect of rotation rate and Reynolds number on aerodynamic characteristics for circular ogive at 60° angle of attack
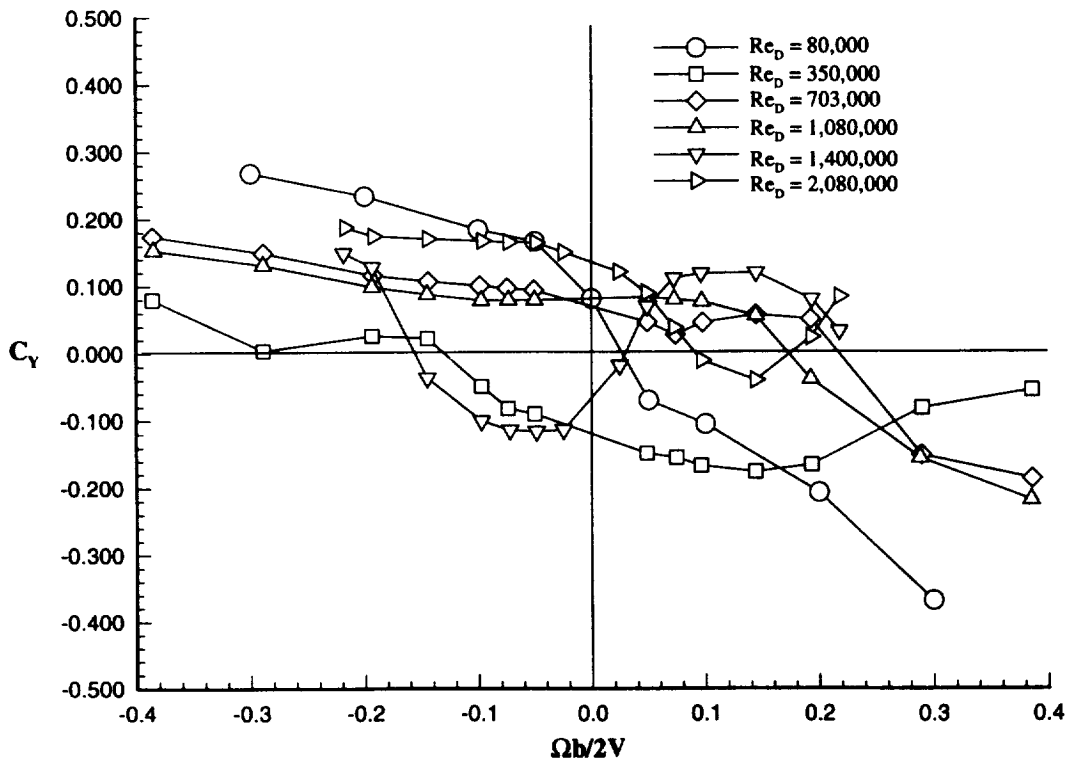
b) Side Force

Figure 15. Effect of rotation rate and Reynolds number on aerodynamic characteristics for circular ogive at 60° angle of attack

Cp
-3.00
-2.56
-2.11
-1.67
-1.22
-0.78
-0.33
0.11
0.56
1.00
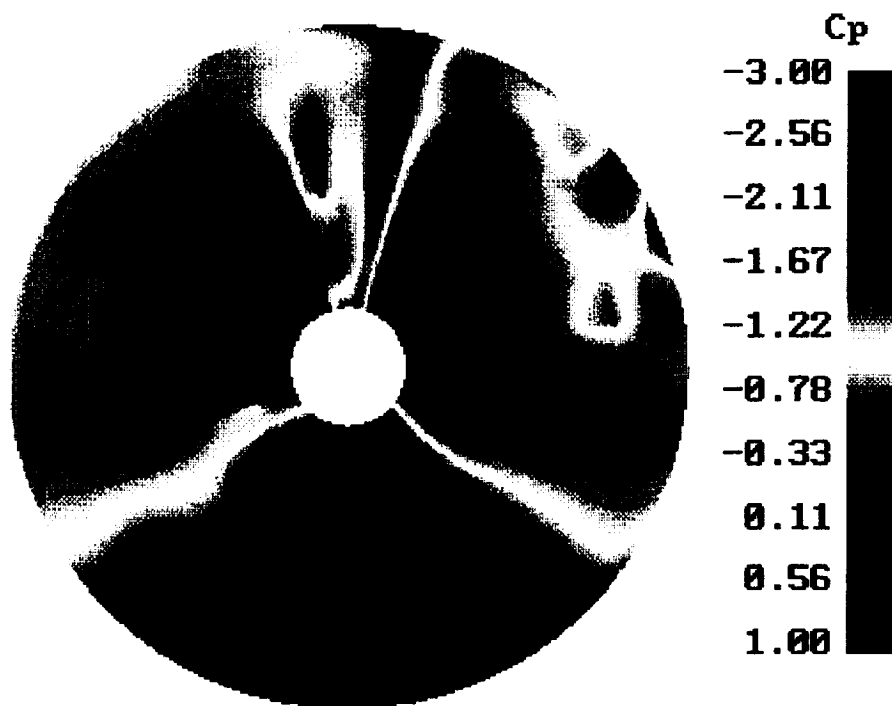
a) Re$_D$ = 89,000
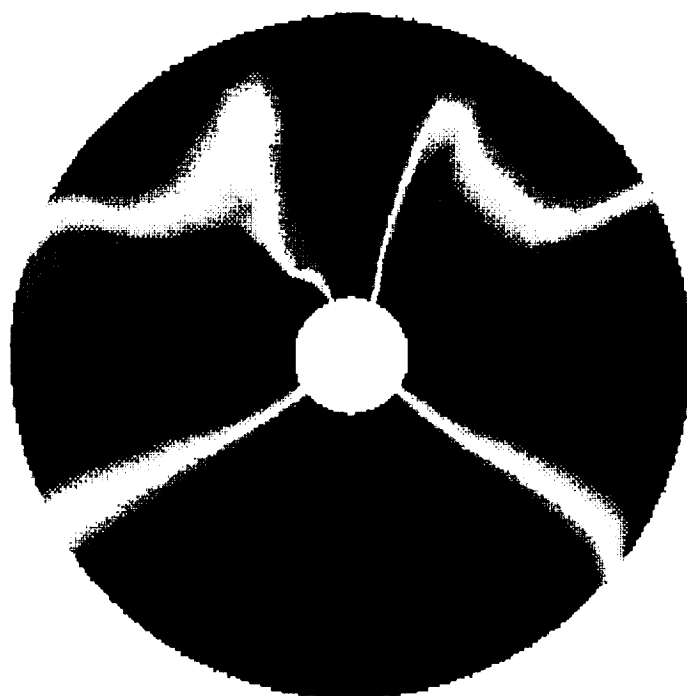
b) Re$_D$ = 350,000

Figure 16. Pressure distribution for the circular ogive at 60° angle of attack for $\Omega b/2V$=0.0.
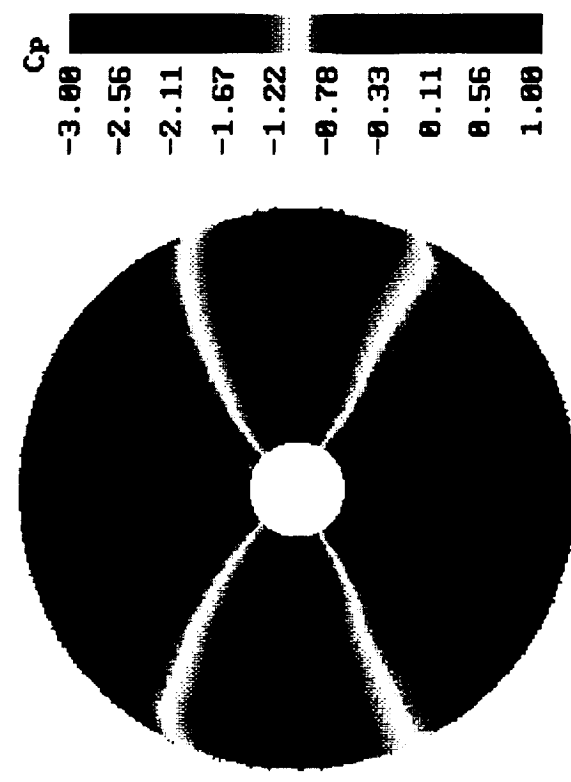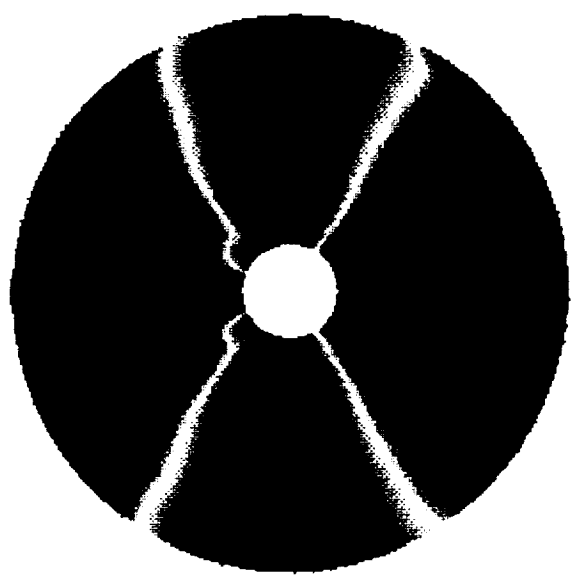
c) $Re_D = 703,000$

d) $Re_D = 1,400,000$
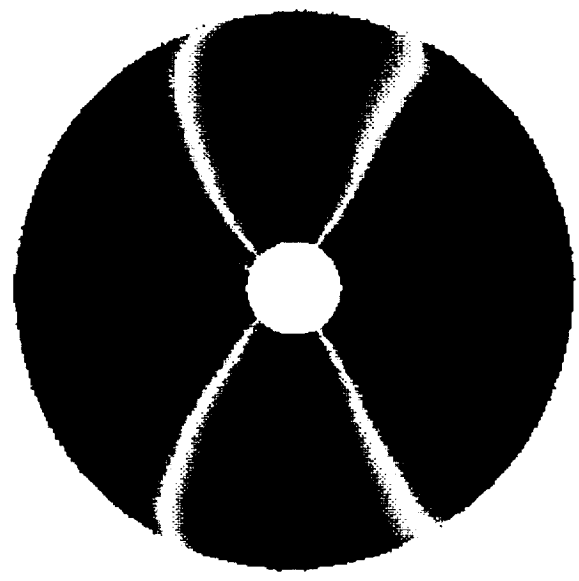
e) $Re_D = 2,080,000$

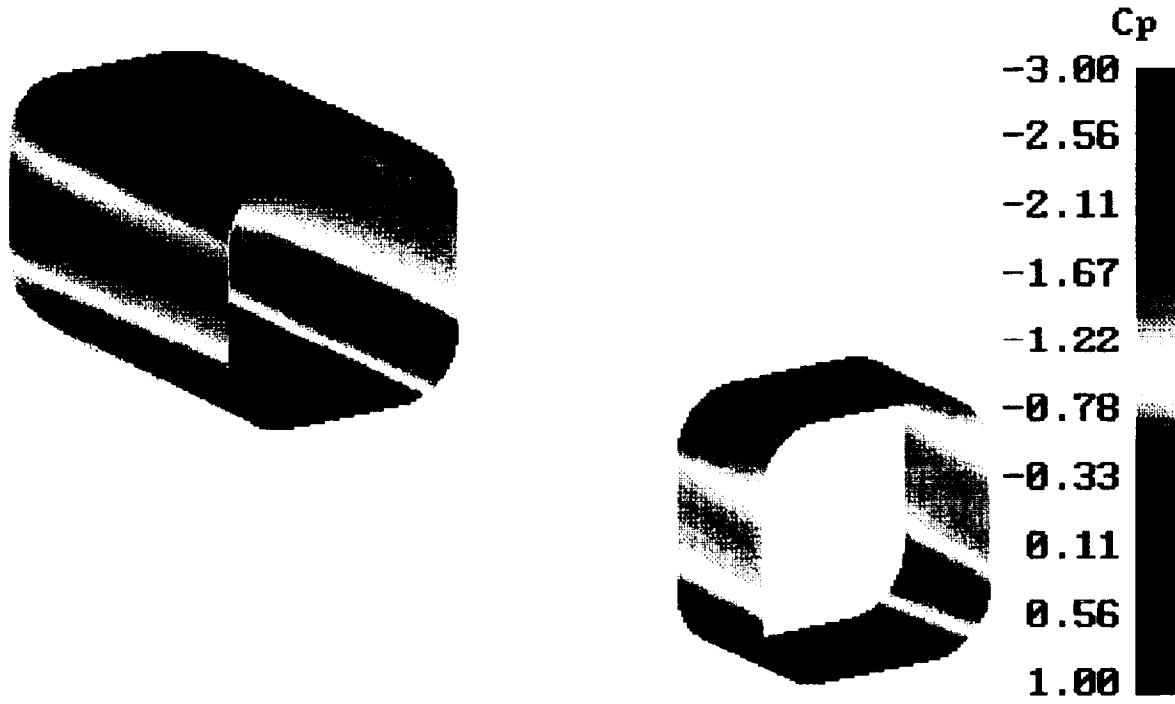Figure 16. Pressure distribution for the circular ogive at 60° angle of attack for $\Omega b/2V = 0.0$.

Cp

-3.00
-2.56
-2.11
-1.67
-1.22
-0.78
-0.33
0.11
0.56
1.00
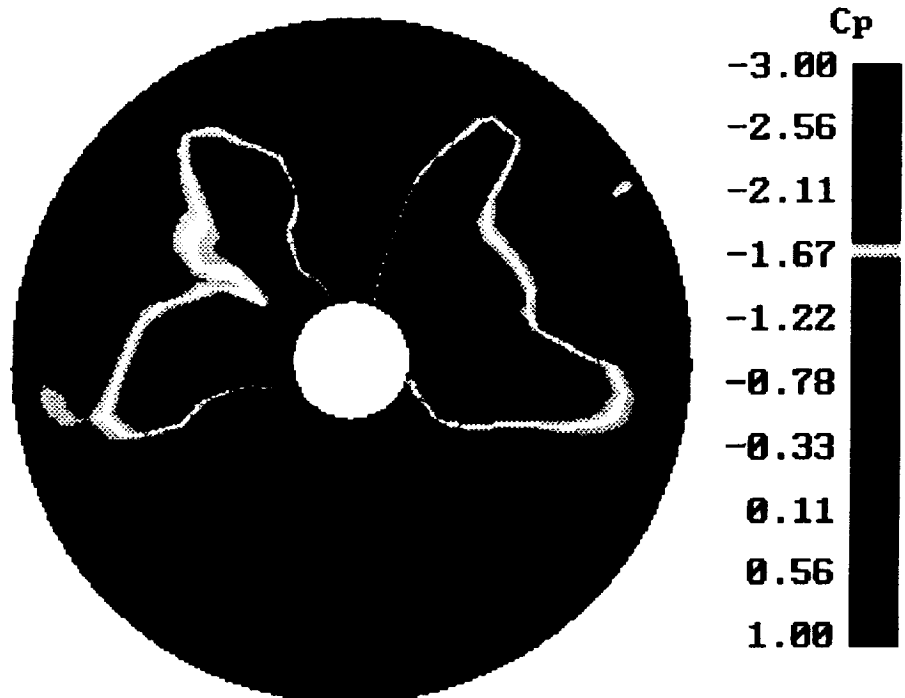
a) $\Omega b/2V = 0.0$

b) $\Omega b/2V = -0.2$

Figure 17. Highlighted pressure distribution for the circular ogive at 60° angle of attack at $Re_D = 89,000$.
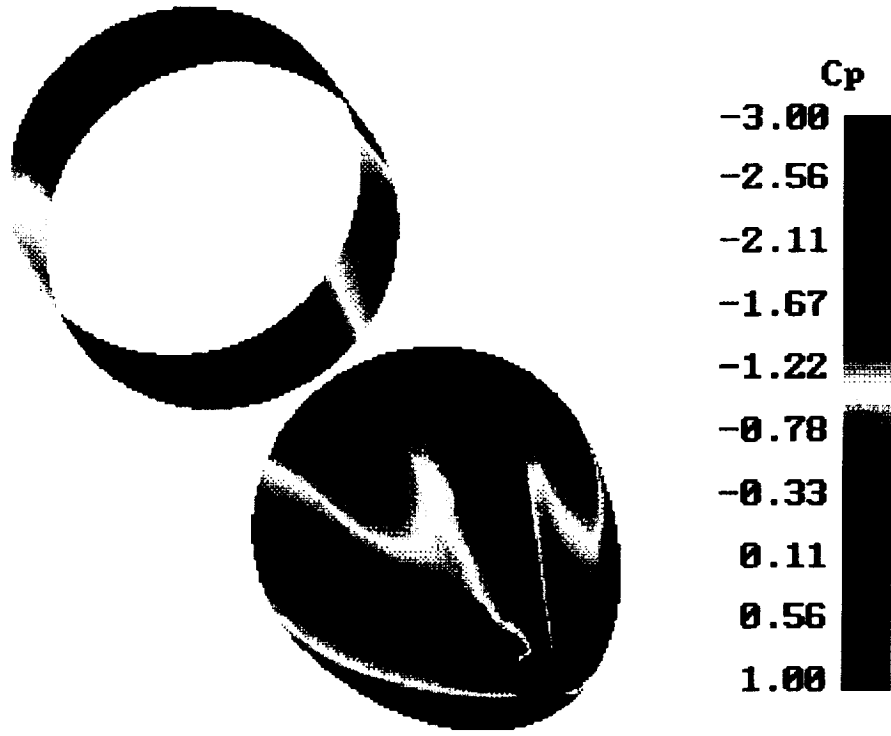
a) $\Omega b/2V=0.0$
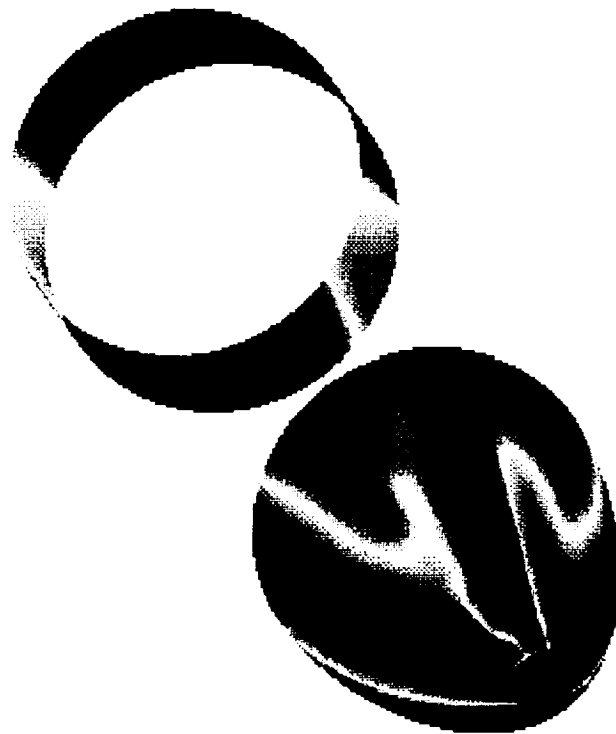
b) $\Omega b/2V=-0.2$

Figure 18. Effect of rotation on the pressure distribution for the circular ogive at 60° angle of attack and $Re_D = 350,000$.

$Re_D = 1,400,000$
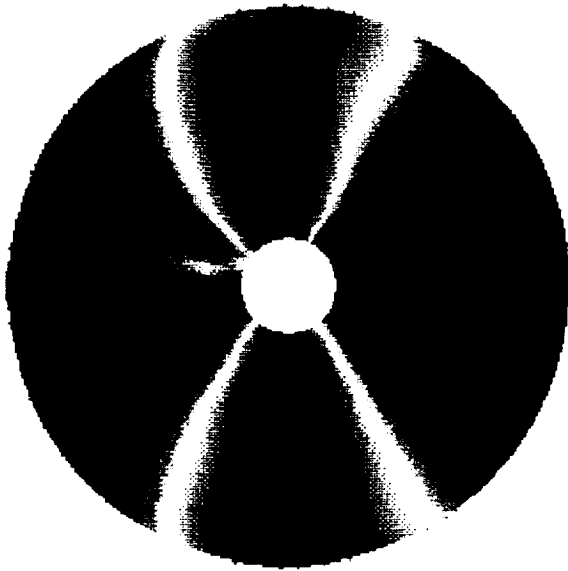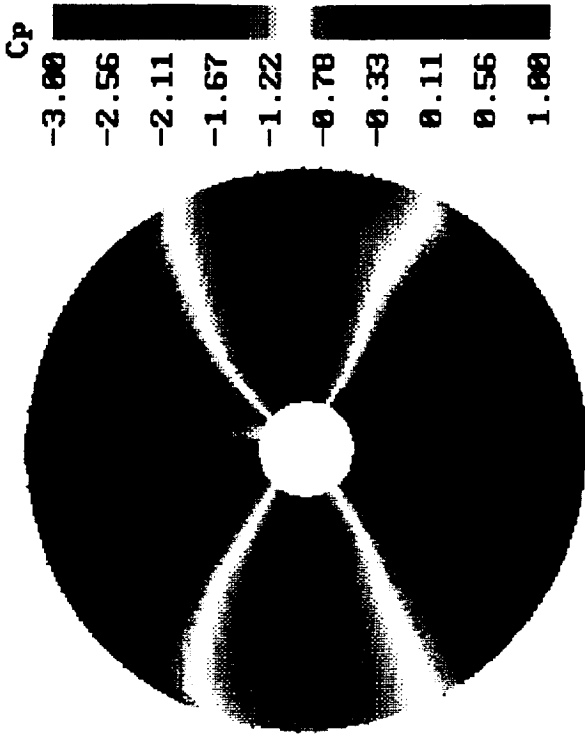
$Re_D = 2,080,000$

Incremental Effects
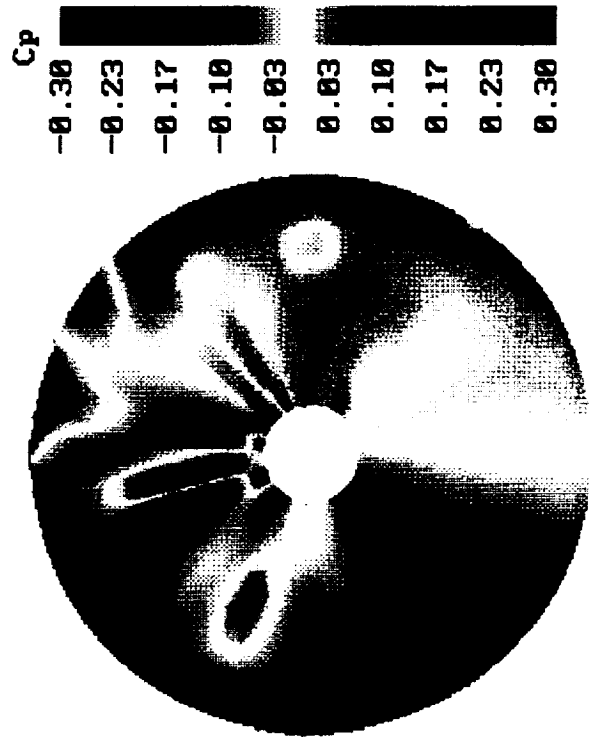
a) $\Omega b/2V = -0.1$

Figure 19. Comparison of the pressure distribution at rotation for the circular ogive at 60° angle of attack for $Re_D = 1,400,000$ and 2,080,000.

$Re_D = 1,400,000$
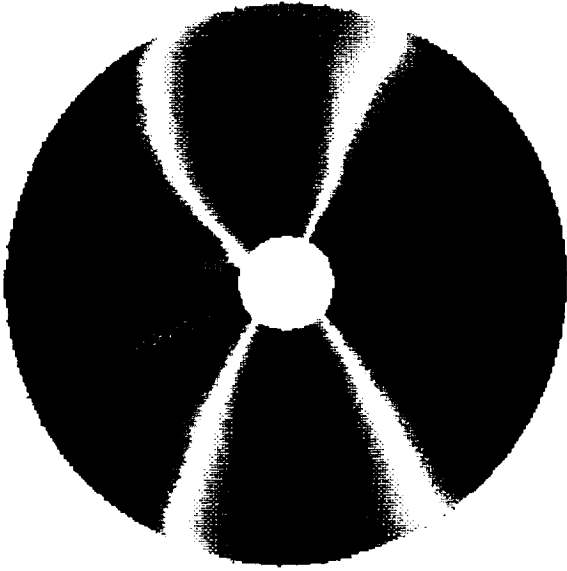
$Re_D = 2,080,000$

Incremental Effects

Cp
-3.00
-2.56
-2.11
-1.67
-1.22
-0.78
-0.33
0.11
0.56
1.00
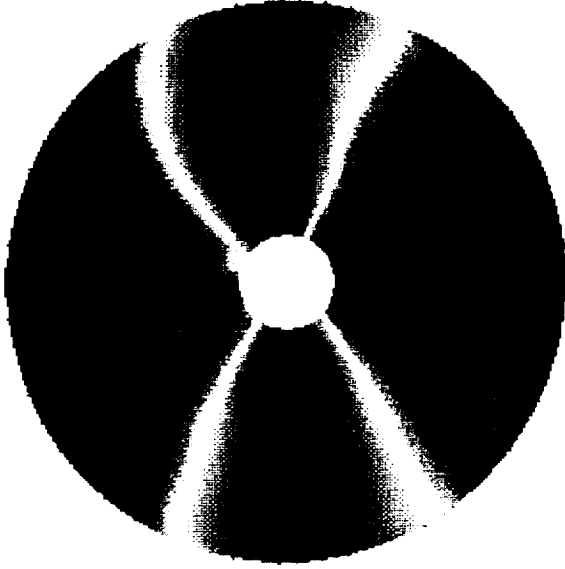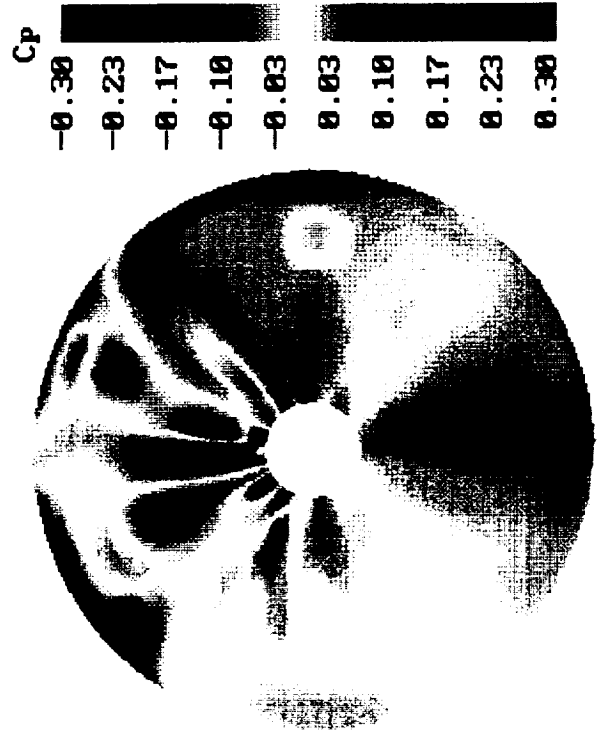
Cp
-0.30
-0.23
-0.17
-0.10
-0.03
0.03
0.10
0.17
0.23
0.30

b) $\Omega b/2V = -0.2$

Figure 19. Comparison of the pressure distribution at rotation for the circular ogive at 60° angle of attack for $Re_D = 1,400,000$ and 2,080,000.

Cp
-3.00
-2.56
-2.11
-1.67
-1.22
-0.78
-0.33
0.11
0.56
1.00
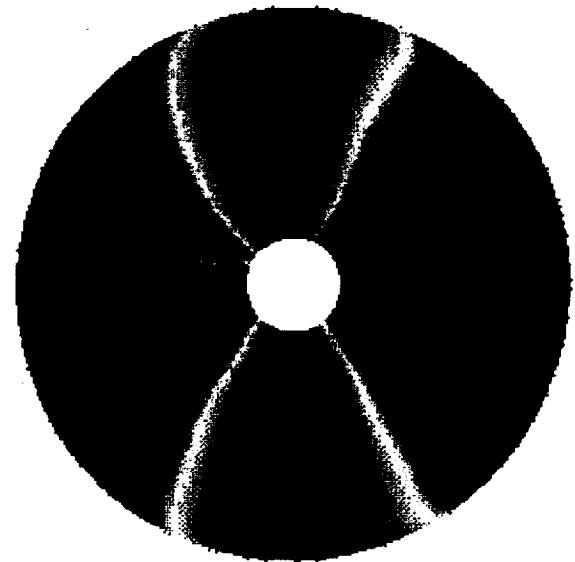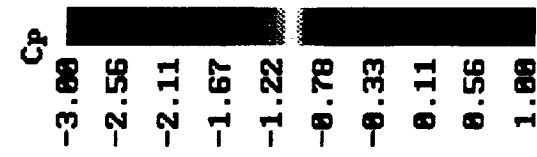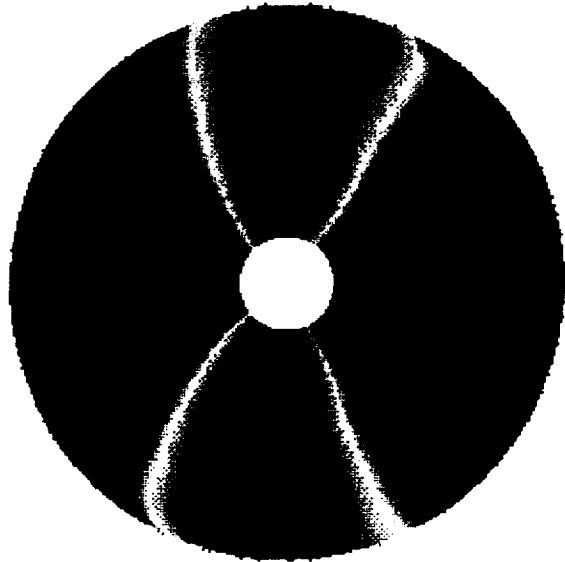
a) $\Omega b/2V = 0.0$

b) $\Omega b/2V = -0.1$

c) $\Omega b/2V = -0.2$

d) $\Omega b/2V = +0.1$
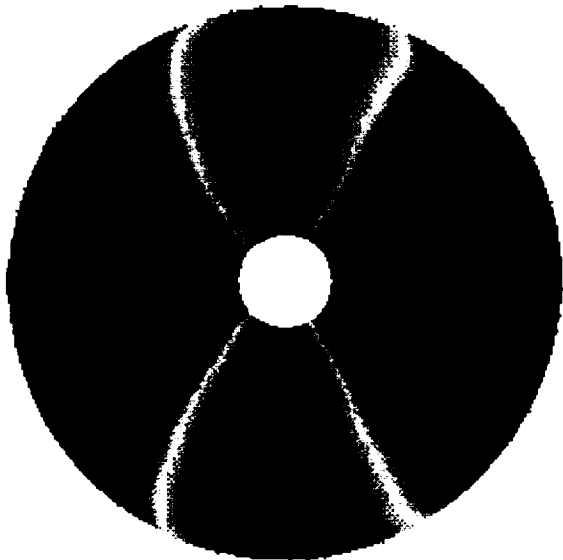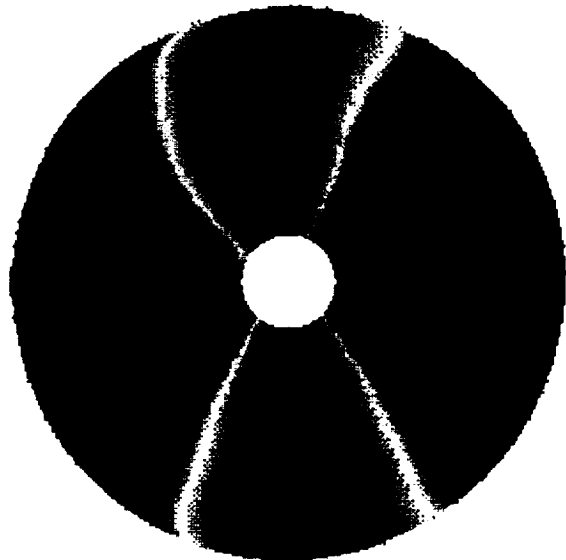
Figure 20. Effect of rotation on the pressure distribution for the circular ogive at 60° angle of attack and $Re_D = 2,080,000$.
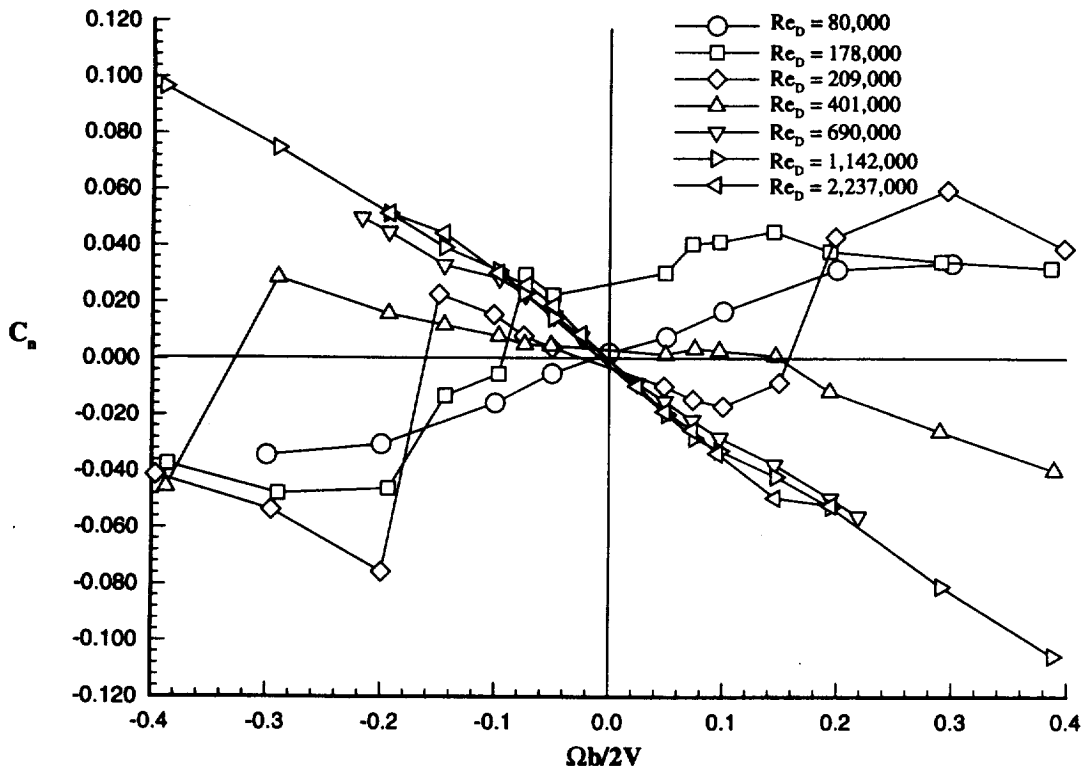
a) Yawing moment

Figure 21. Effect of rotation rate and Reynolds number on aerodynamic characteristics for rectangular ogive at 90° angle of attack
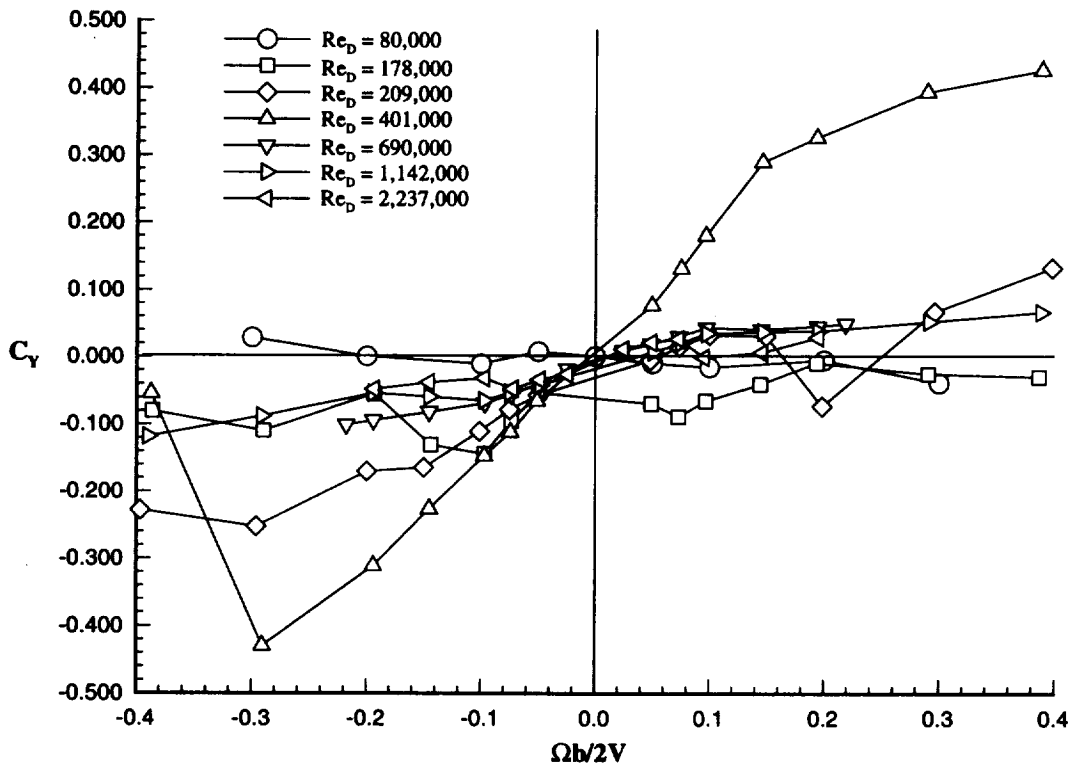
b) Side Force

Figure 21. Effect of rotation rate and Reynolds number on aerodynamic characteristics for rectangular ogive at 90° angle of attack

Cp

3.00
2.56
2.11
1.67
1.22
0.78
0.33
0.11
0.56
1.00
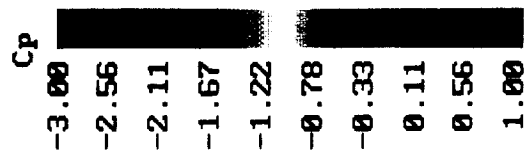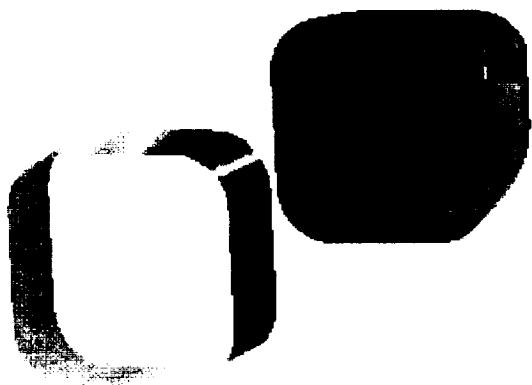
a) Re_D = 178,000

b) Re_D = 401,000

c) Re_D = 2,237,000

Figure 22. Pressure distribution for the the rectangular ogive at 90° angle of attack and $\Omega b/2V$=0.0.
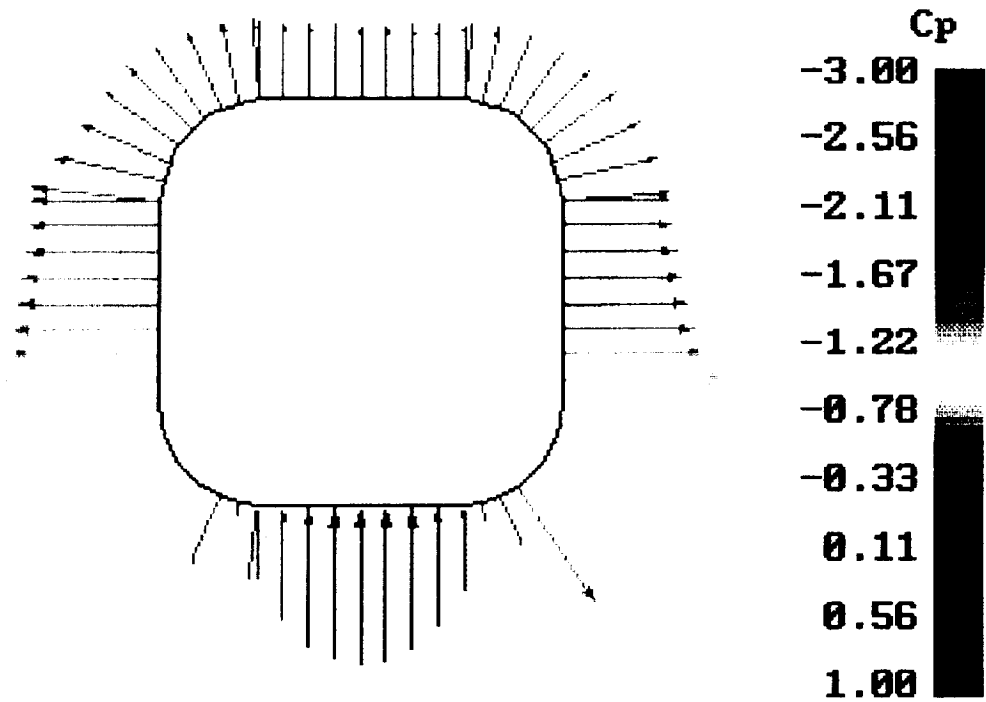
a) Re$_D$ = 401,000
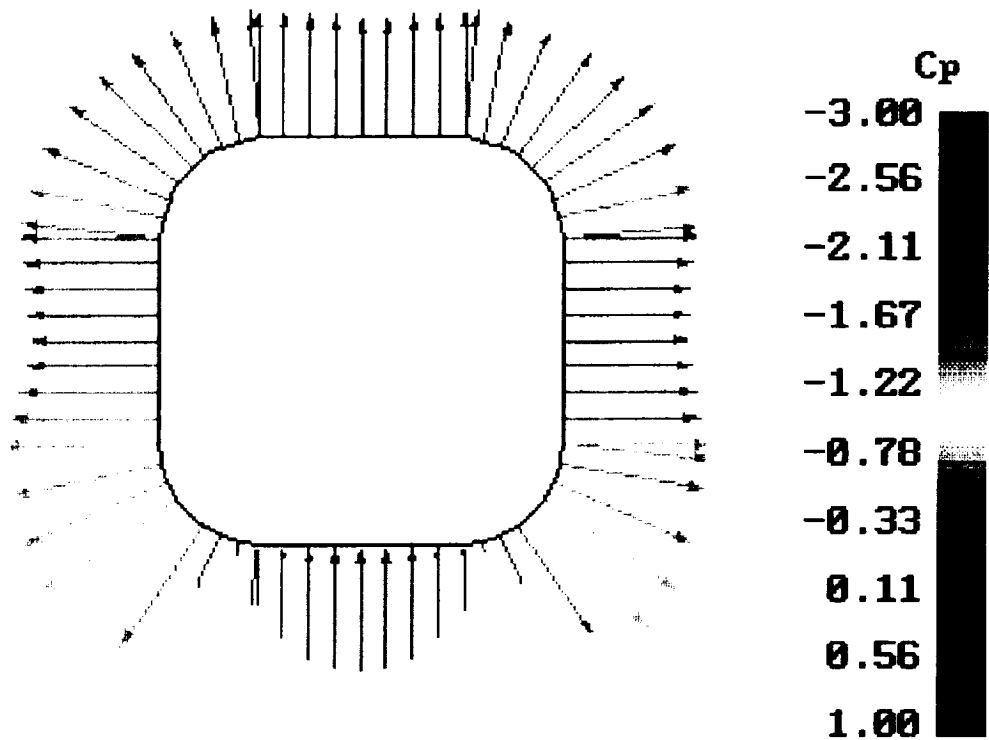
b) Re$_D$ = 178,000

Figure 23. Local pressure distribution at forebody station 0.67x/D and Ωb/2V=0.0.
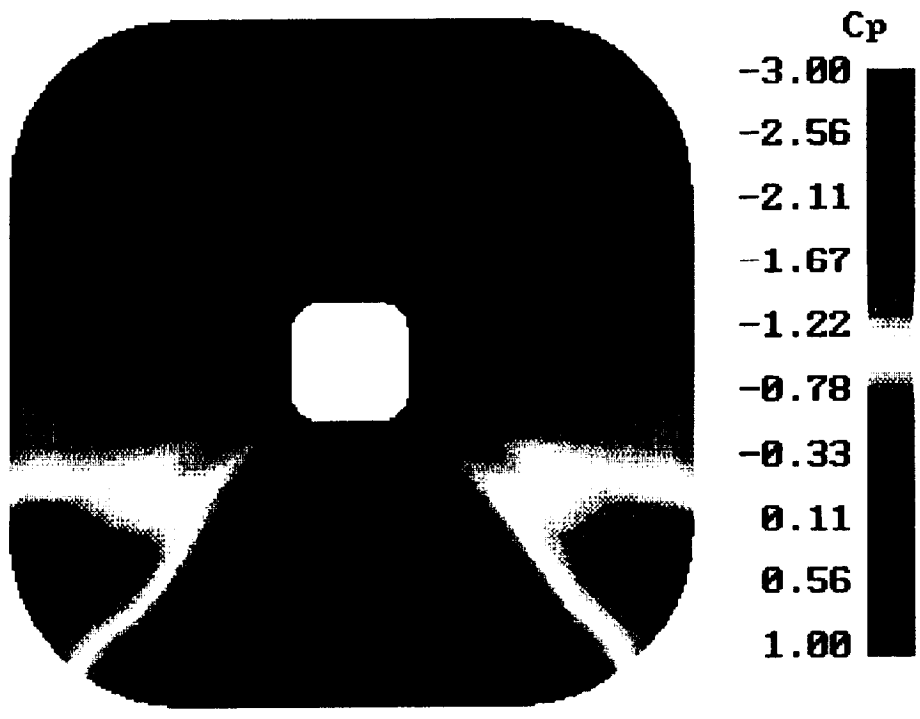
a) $Re_D = 401,000$
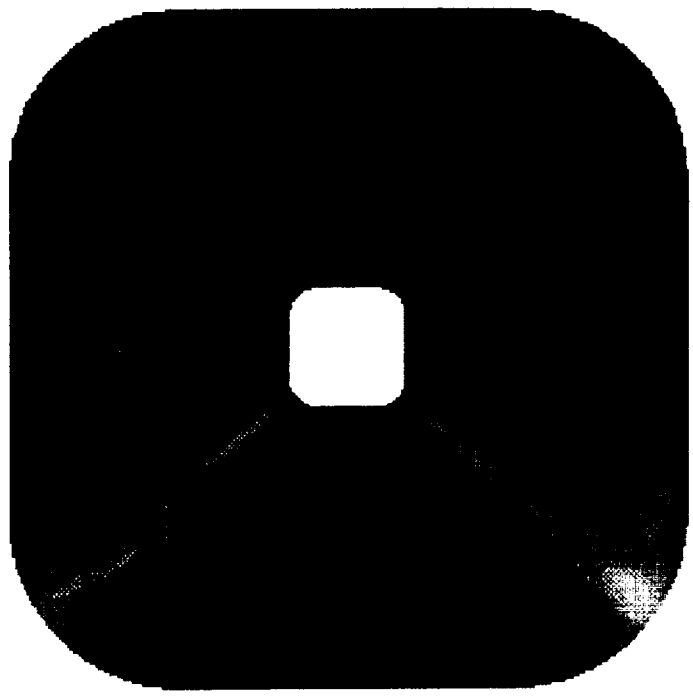
b) $Re_D = 178,000$

Figure 24. Frontal view of pressure distribution for the rectangular ogive at 90° angle of attack and $\Omega b/2V=0.0$.

Cp

-3.00
-2.56
-2.11
-1.67
-1.22
-0.78
-0.33
0.11
0.56
1.00
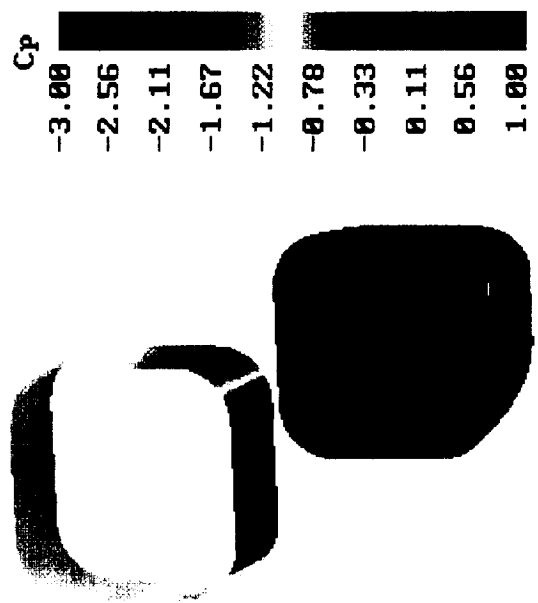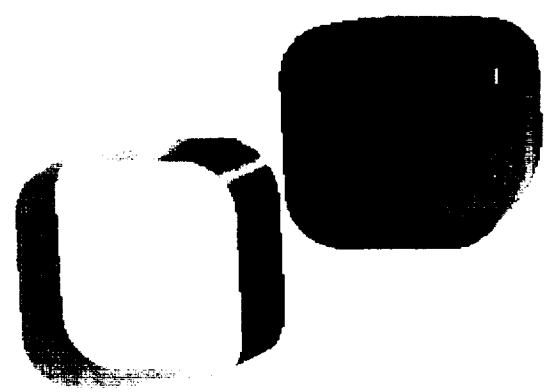
a) $\Omega b/2V = -0.4$

b) $\Omega b/2V = -0.05$

c) $\Omega b/2V = +0.05$

Figure 25. Effect of rotation on pressure distribution for the rectangular ogive at 90° angle of attack and $Re_D = 178,000$.
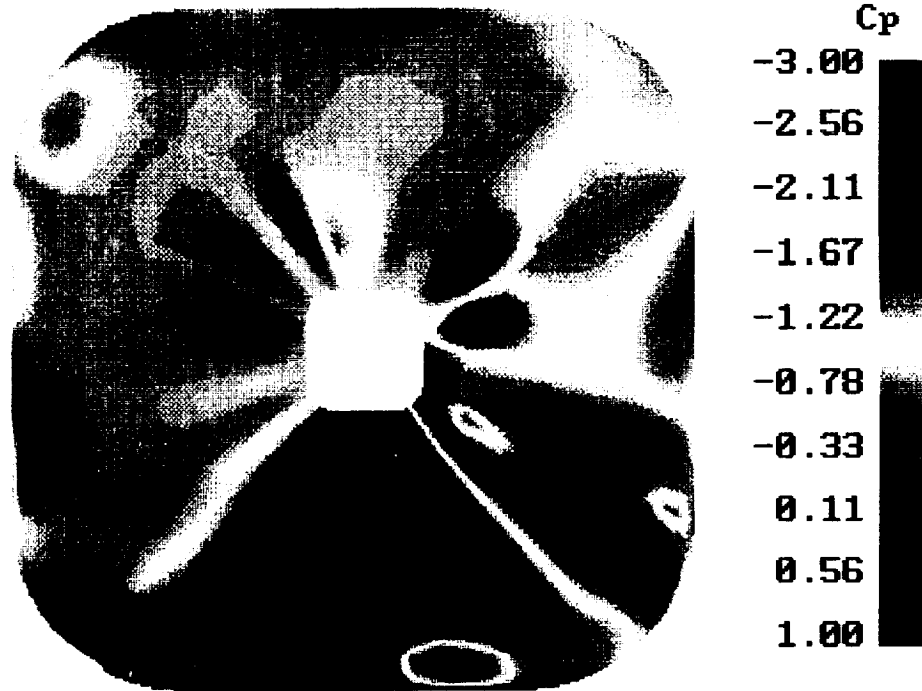
a) $\Omega b/2V = -0.2$
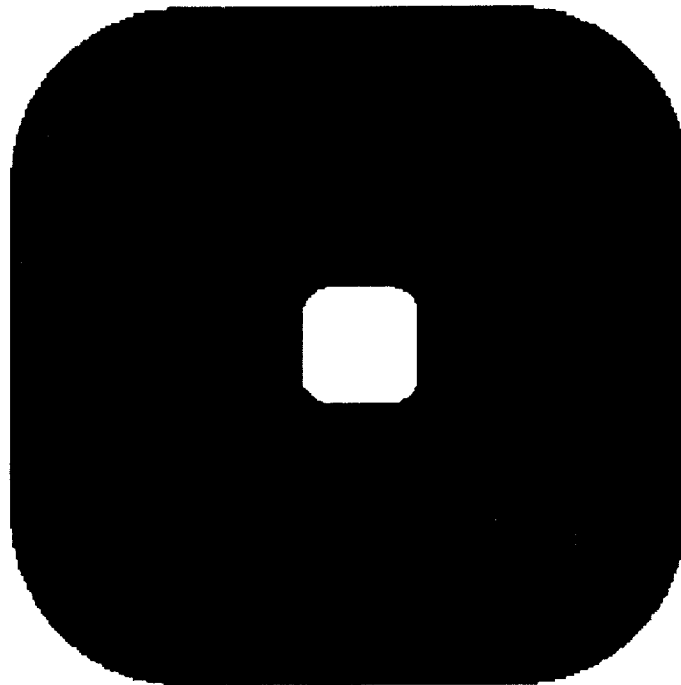
b) $\Omega b/2V = -0.1$

Figure 26. Transition effects on the pressure distribution for the rectangular ogive at 90° angle of attack and $Re_D = 209,000$.

Cp

-3.00
-2.56
-2.11
-1.67
-1.22
-0.78
-0.33
0.11
0.56
1.00

a) $\Omega b/2V = -0.4$ (Head-on view)

b) $\Omega b/2V = -0.4$ (Full view)
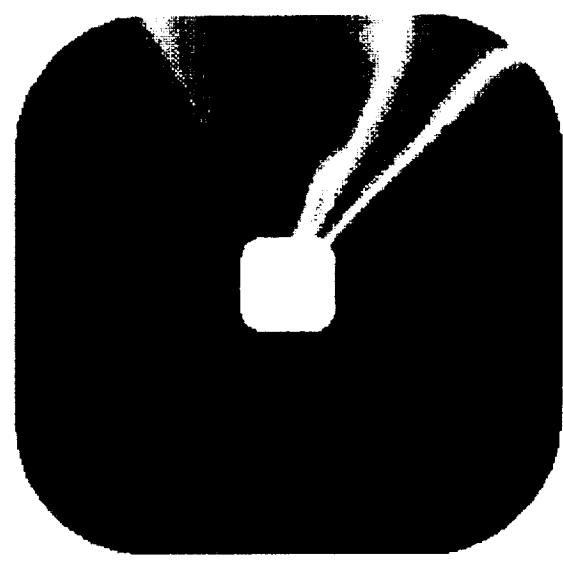
c) $\Omega b/2V = -0.3$ (Head-on view)

d) $\Omega b/2V = -0.3$ (Full view)

Figure 27. Transition effects on the pressure distribution for the rectangular ogive at 90° angle of attack and $Re_D = 401,000$.
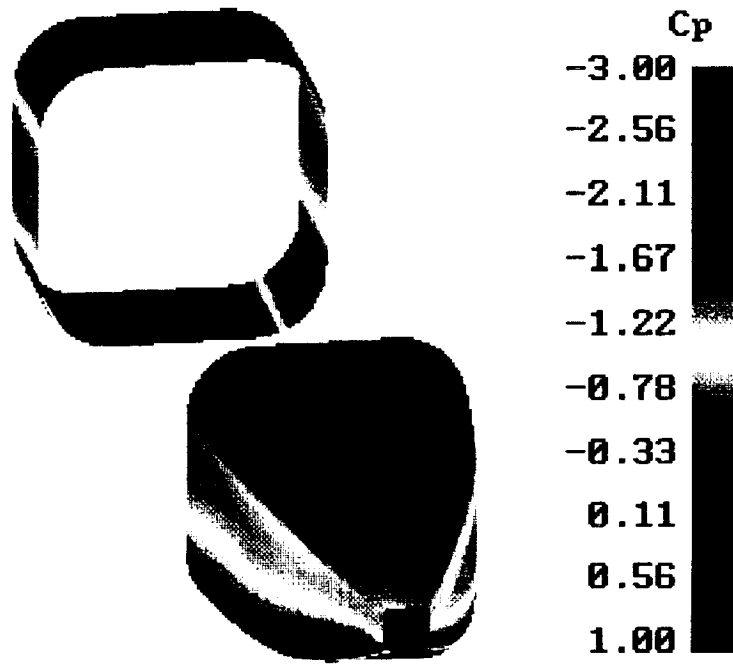
a) $Re_D = 1,142,000$

b) $Re_D = 2,237,000$

Figure 28. Pressure distribution for the rectangular ogive at 90° angle of attack and $\Omega b/2V = -0.2$.
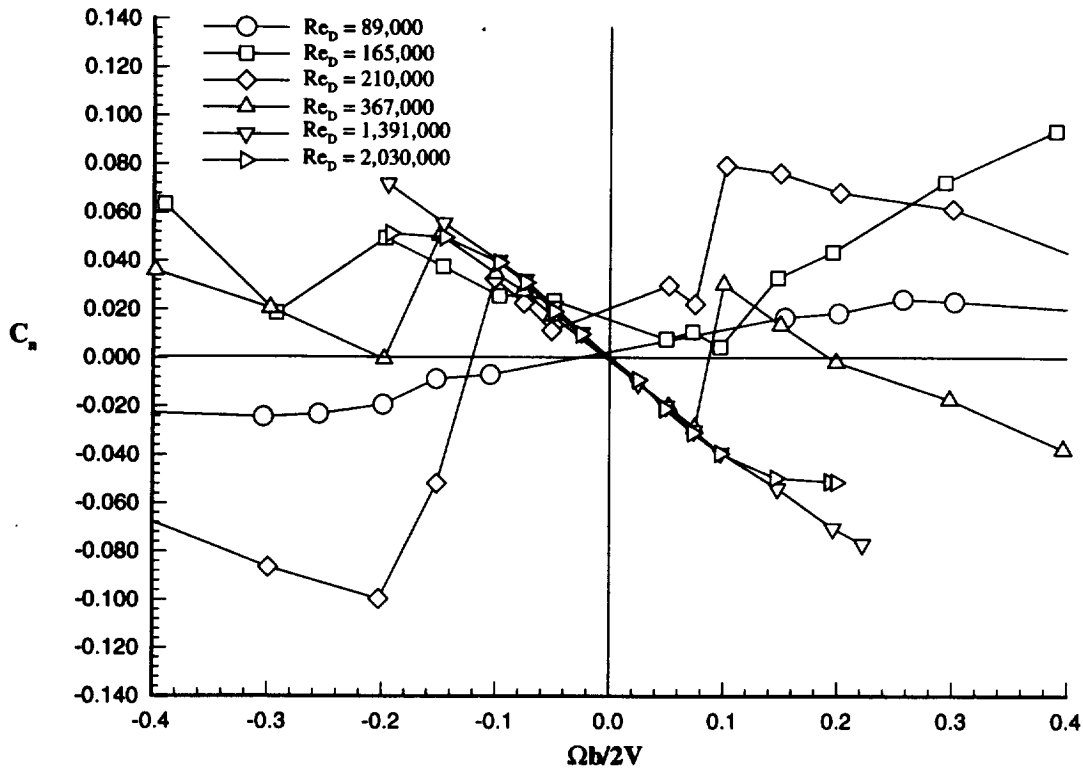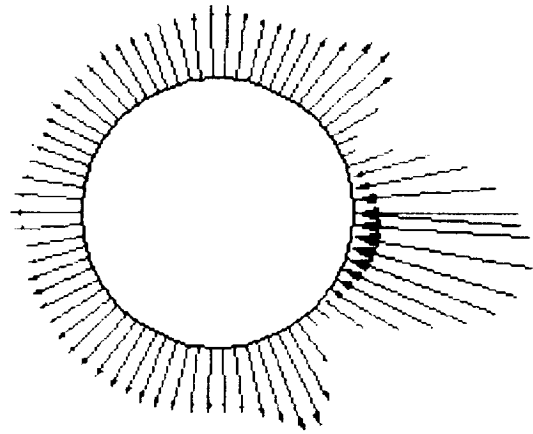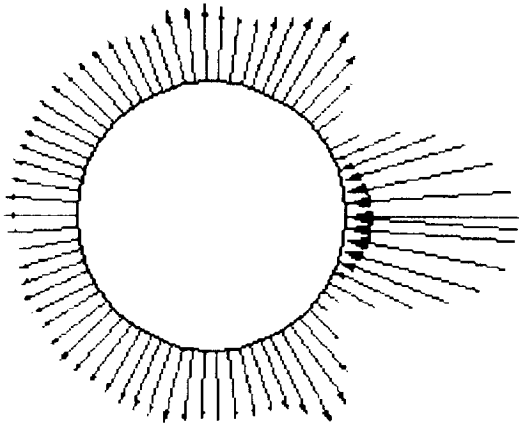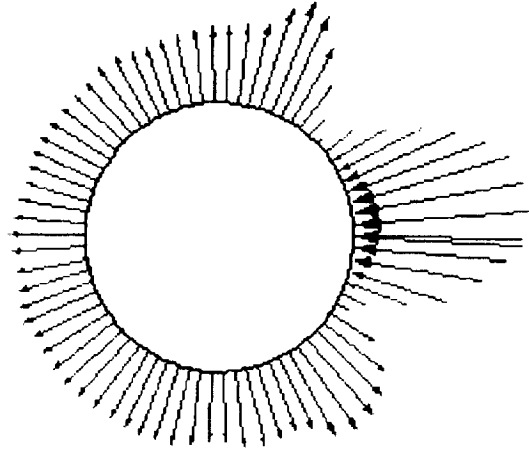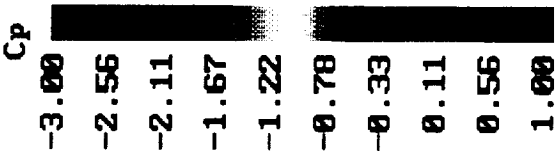
a) Yawing moment

Figure 29. Effect of rotation rate and Reynolds number on aerodynamic characteristics for rectangular hemisphere at 90° angle of attack
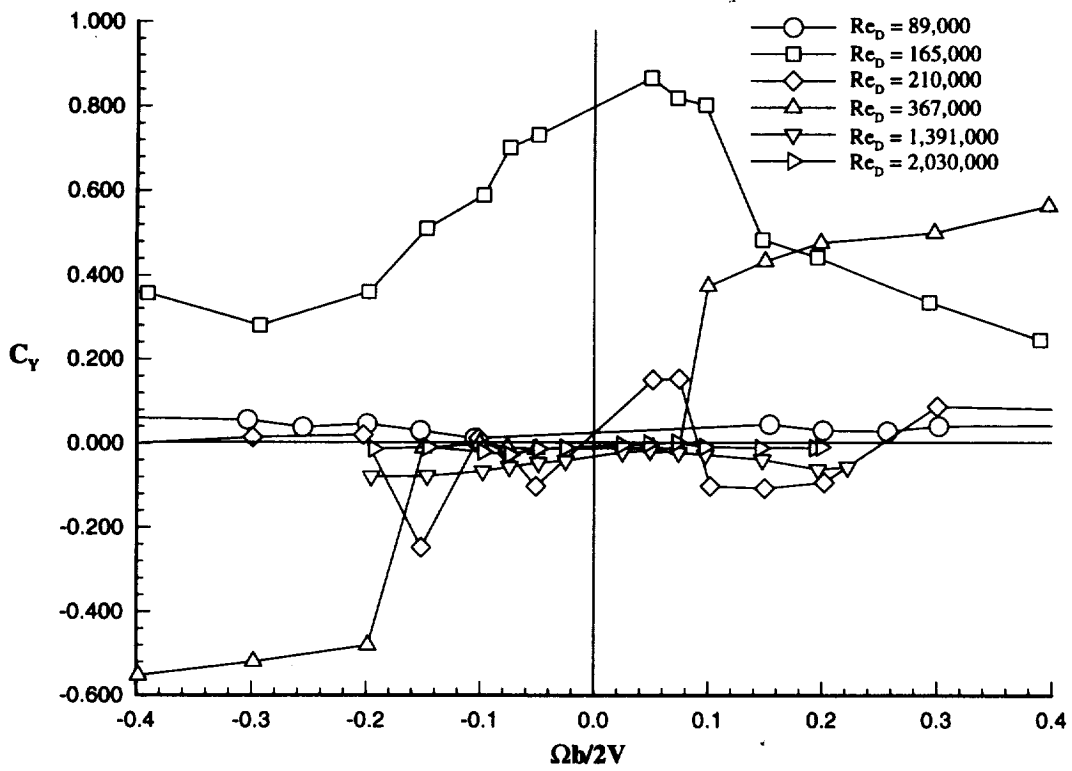
b) Side Force

Figure 29. Effect of rotation rate and Reynolds number on aerodynamic characteristics for rectangular hemisphere at 90" angle of attack

Cp
-3.00
-2.56
-2.11
-1.67
-1.22
-0.78
-0.33
0.11
0.56
1.00

a) Rectangular Hemisphere; Re_D = 350,000
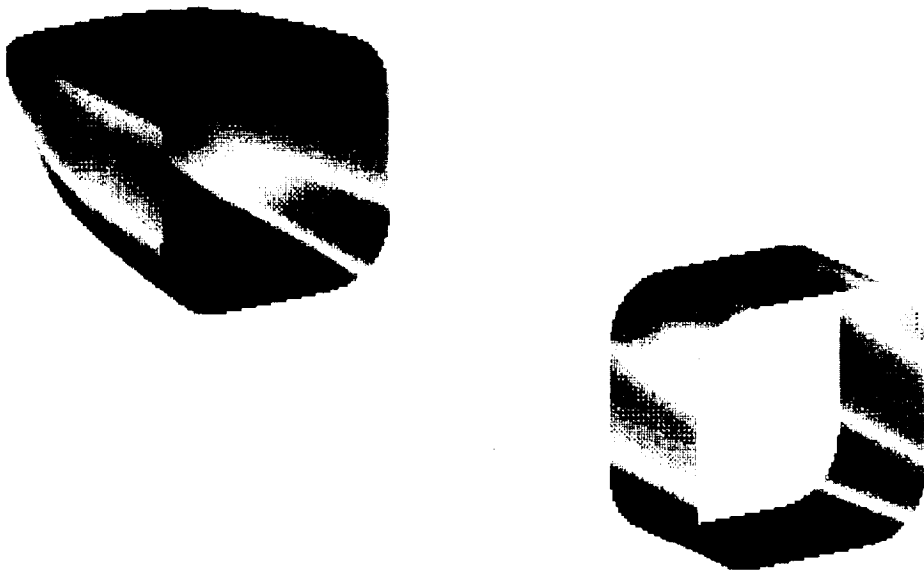
b) Rectangular Ogive; Re_D = 350,000

Figure 30. Comparison of the pressure distribution for rectangular cross-section aftbodies at low Reynolds numbers and $\Omega b/2V$=-0.1.
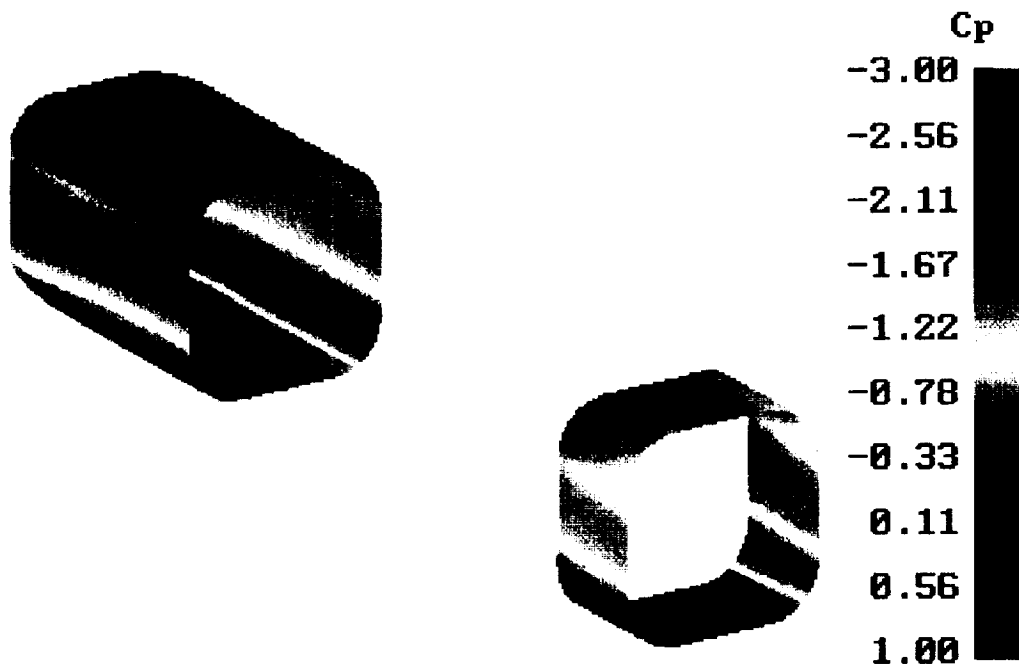
a) Rectangular Hemisphere; $Re_D = 2,030,000$
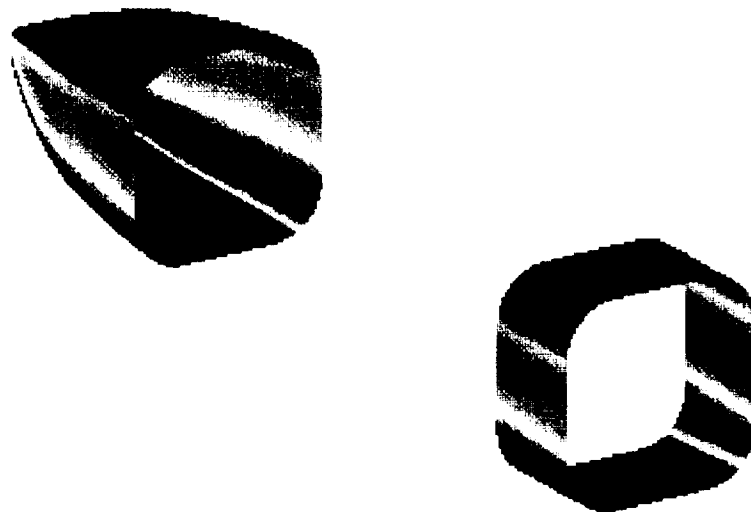
b) Rectangular Ogive; $Re_D = 2,237,000$

Figure 31. Comparison of the pressure distribution for rectangular cross-section aftbodies at high Reynolds numbers and $\Omega b/2V = -0.1$.
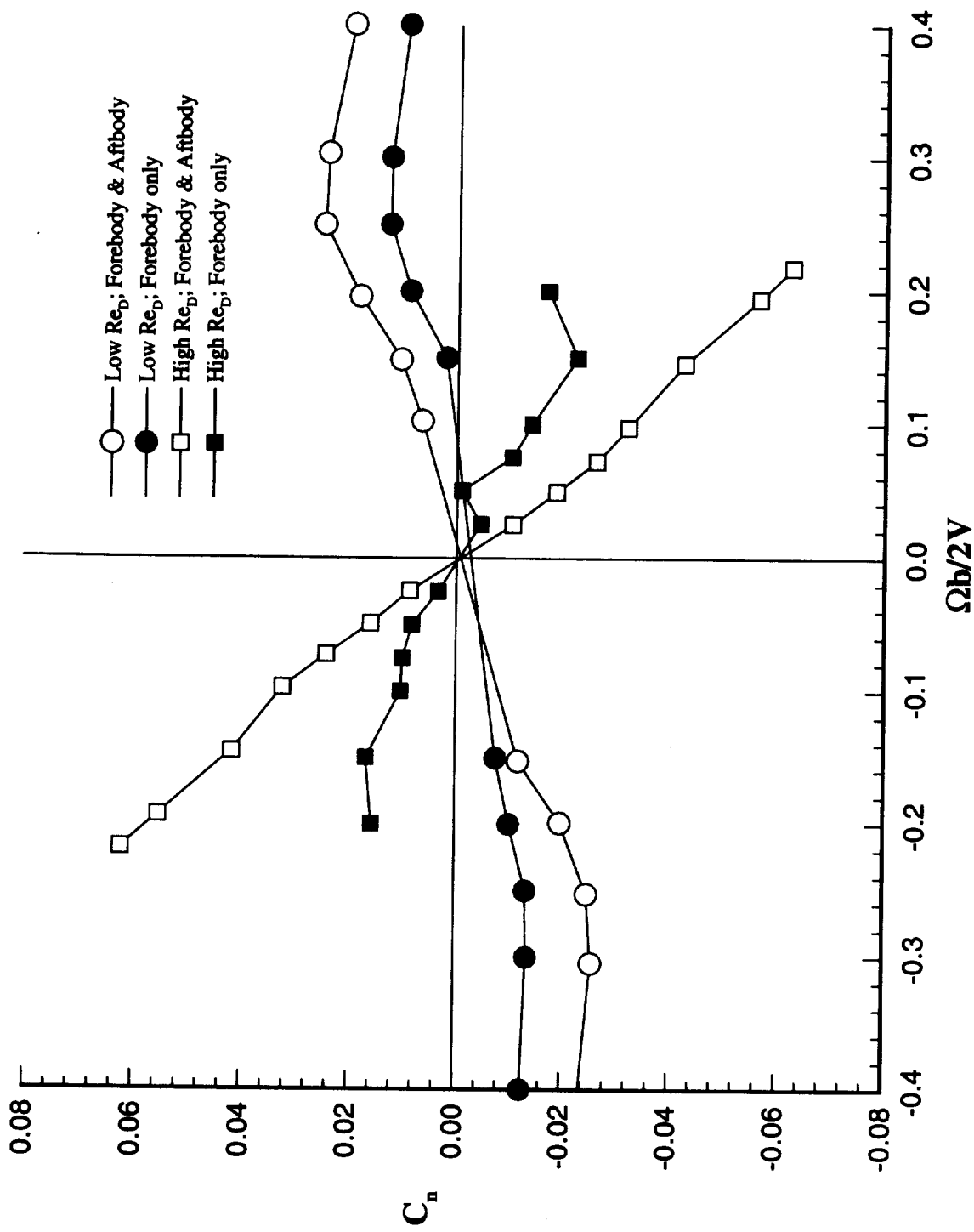
Figure 32. Effect of aftbody on overall yawing moment characteristics for rectangular ogive at 90° angle of attack
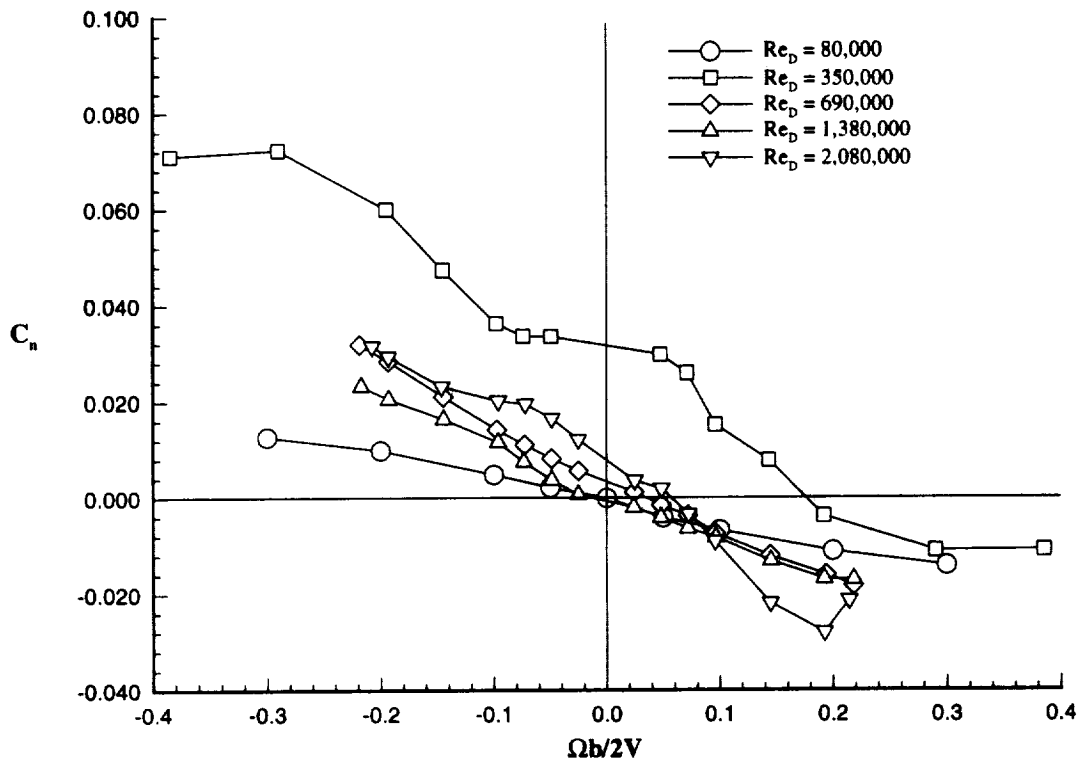
a) Yawing moment

Figure 33. Effect of rotation rate and Reynolds number on aerodynamic characteristics for circular ogive at 90° angle of attack
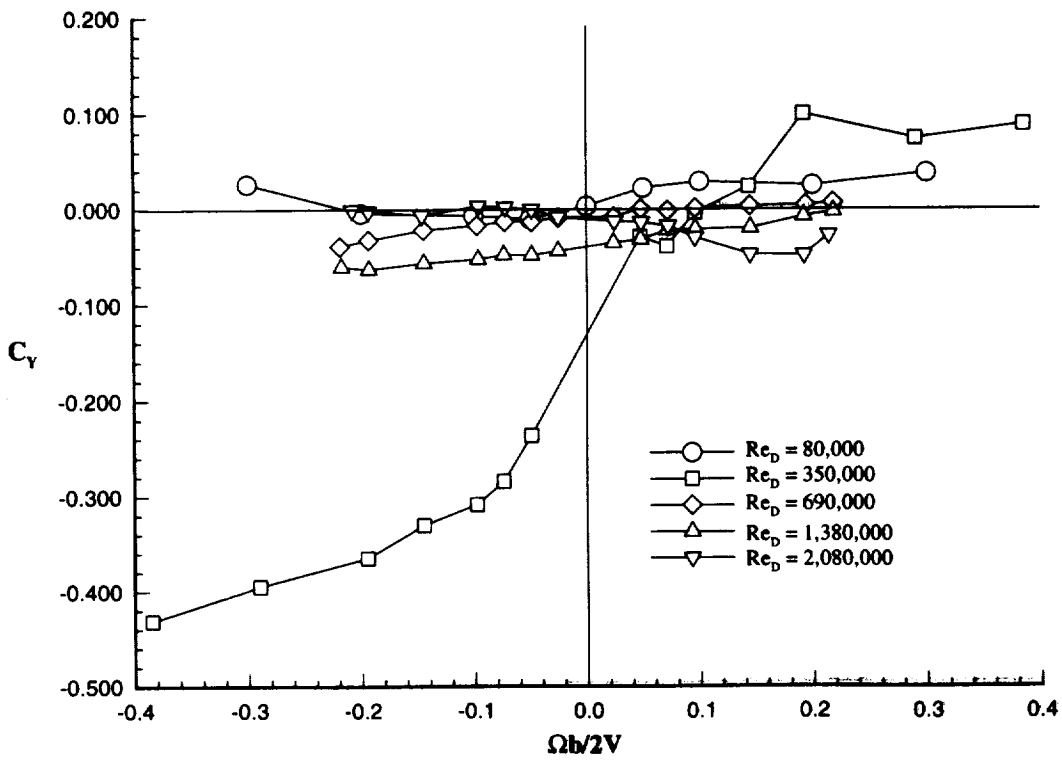
b) Side Force

Figure 33. Effect of rotation rate and Reynolds number on aerodynamic characteristics for circular ogive at 90° angle of attack

Cp

-3.00
-2.56
-2.11
-1.67
-1.22
-0.78
-0.33
0.11
0.56
1.00
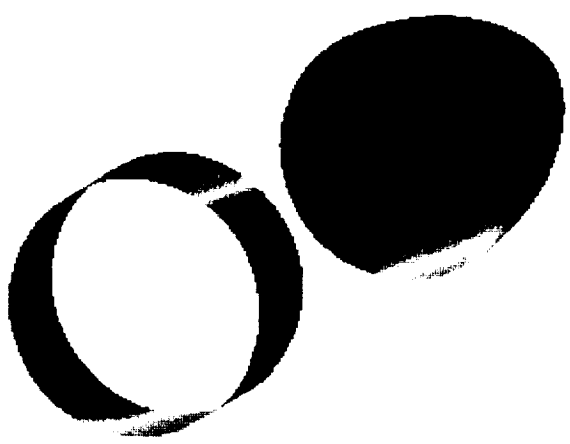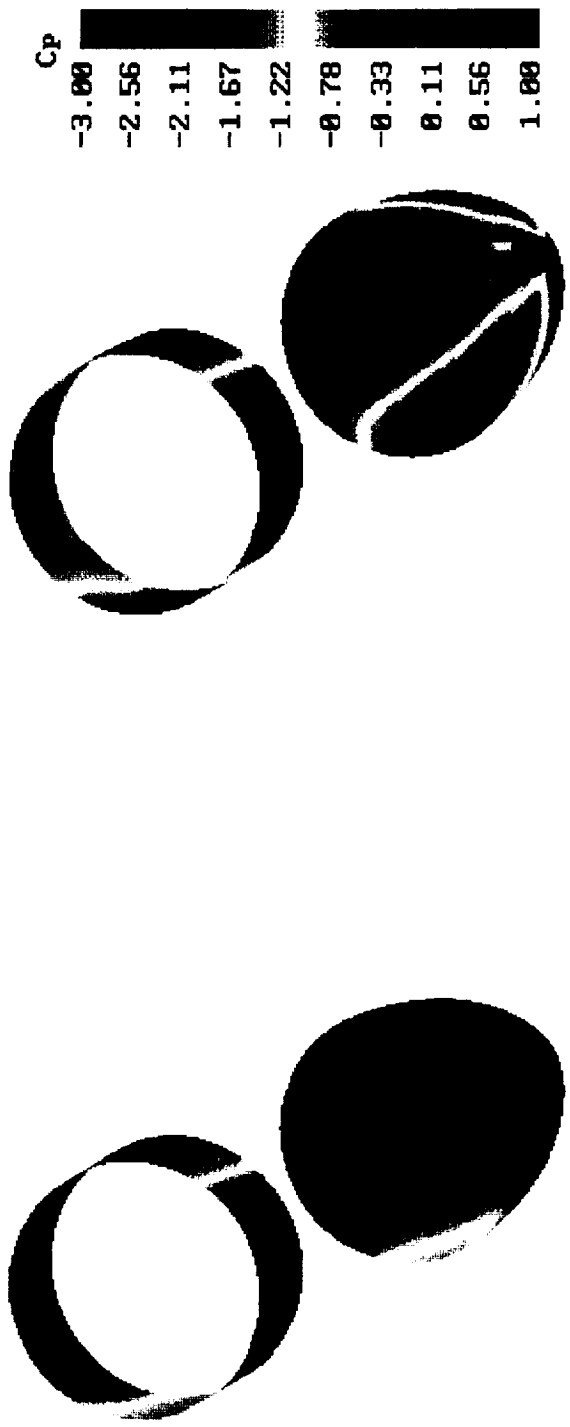
a) $Re_D = 350{,}000$

b) $Re_D = 690{,}000$

c) $Re_D = 1{,}380{,}000$
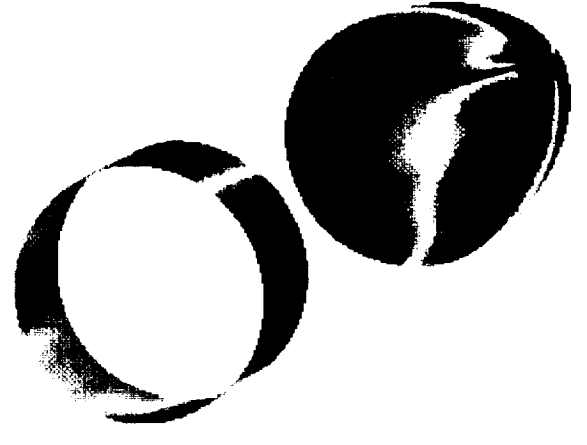
d) $Re_D = 2{,}080{,}000$

Figure 34. Pressure distribution for the circular ogive at 90° angle of attack and $\Omega b/2V = 0.0$.

C_p

-3.00
-2.56
-2.11
-1.67
-1.22
-0.78
-0.33
0.11
0.56
1.00

a) $\Omega b/2V = 0.0$

b) $\Omega b/2V = -0.2$

c) $\Omega b/2V = +0.2$

Figure 35. Effect of rotation rate on the local pressure distribution for the circular ogive at 90° angle of attack; $Re_D = 350,000$ $x/D=0.333$.

a) $Re_D = 350,000$

b) $Re_D = 690,000$

c) $Re_D = 1,380,000$

d) $Re_D = 2,080,000$
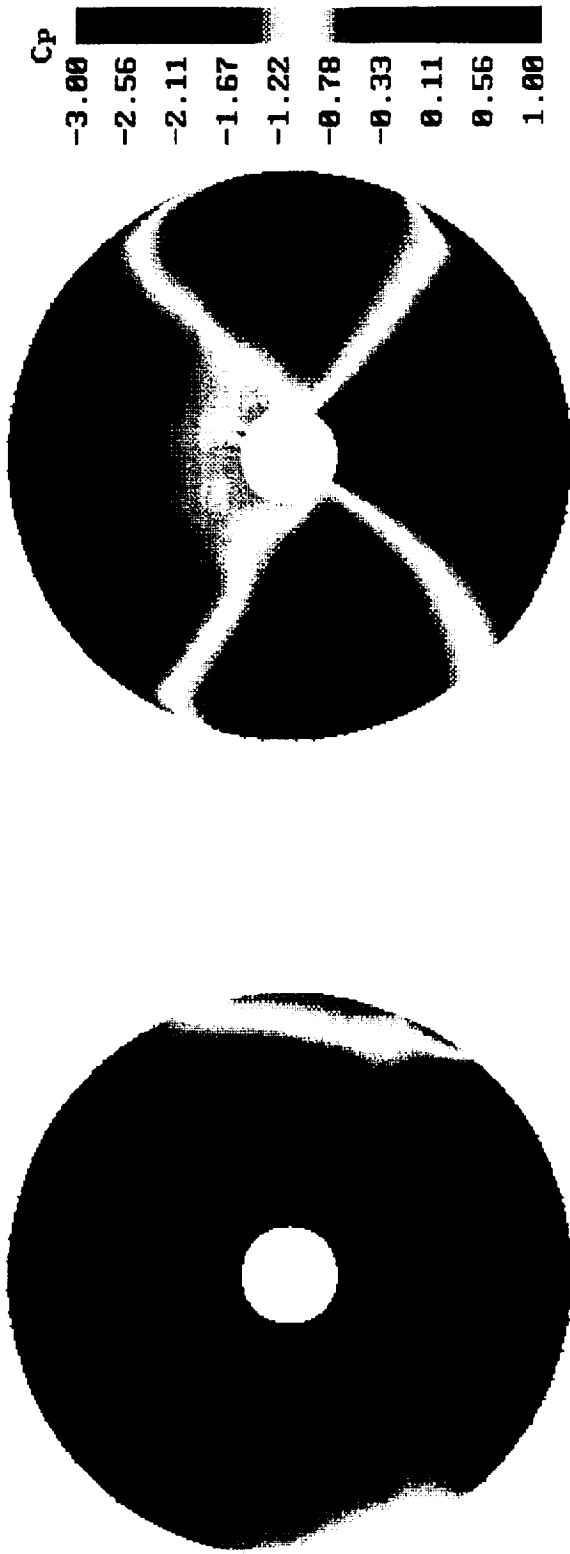
Figure 36. Frontal view of pressure distribution for the circular ogive at 90° angle of attack; $\Omega b/2V = -0.2$.

a) $Re_D = 350{,}000$

b) $Re_D = 690{,}000$

c) $Re_D = 1{,}380{,}000$

d) $Re_D = 2{,}080{,}000$

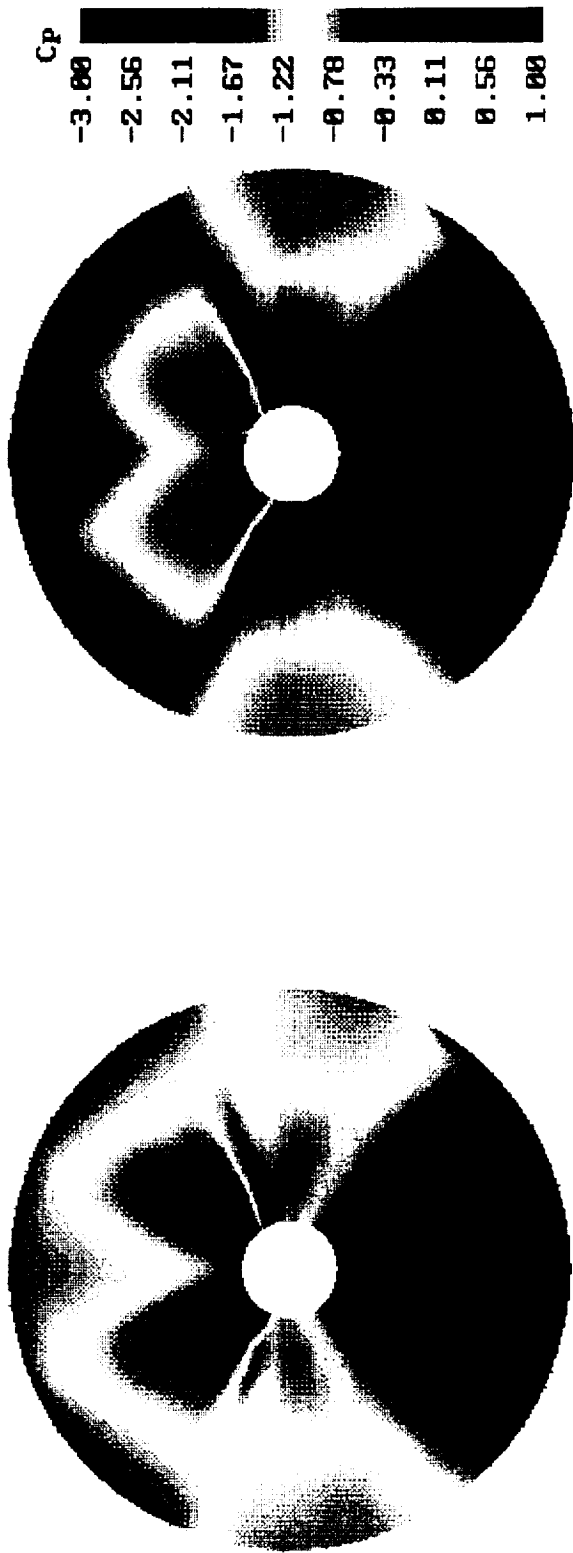Figure 37. Full view of pressure distribution for the circular ogive at 90° angle of attack; $\Omega b/2V = -0.2$.
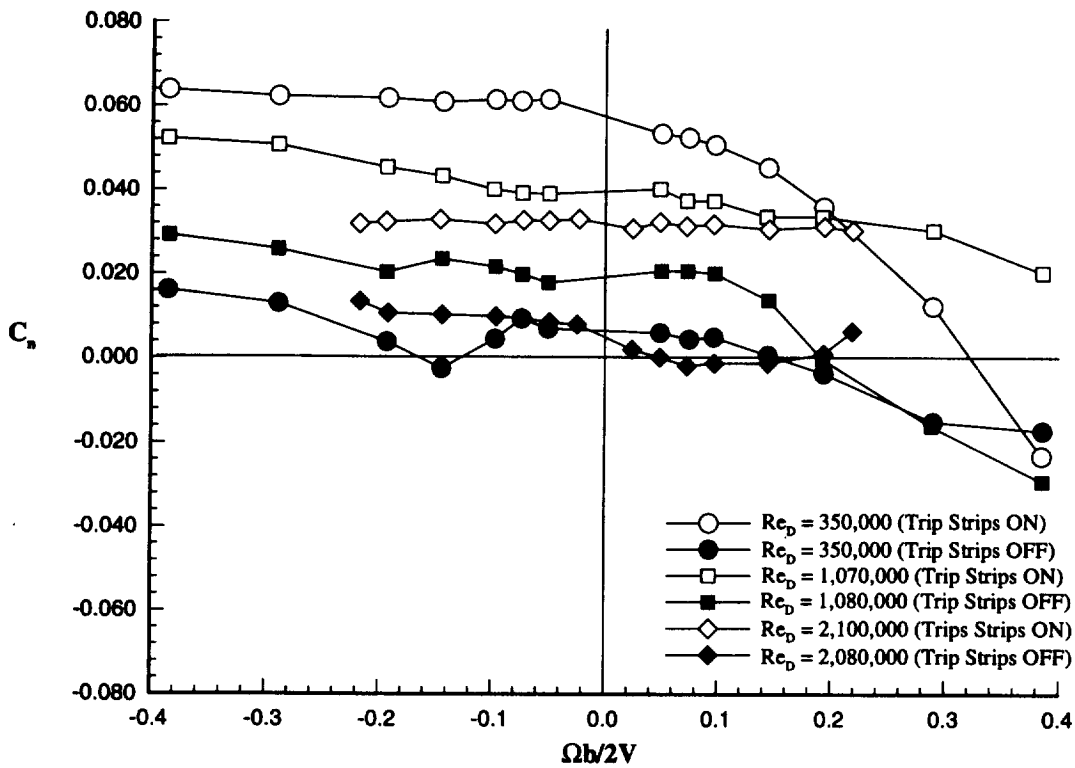
a) Yawing moment

Figure 38. Effect of trip strips on rotational aerodynamic characteristics at selected Reynolds numbers for the circular ogive at 60° angle of attack
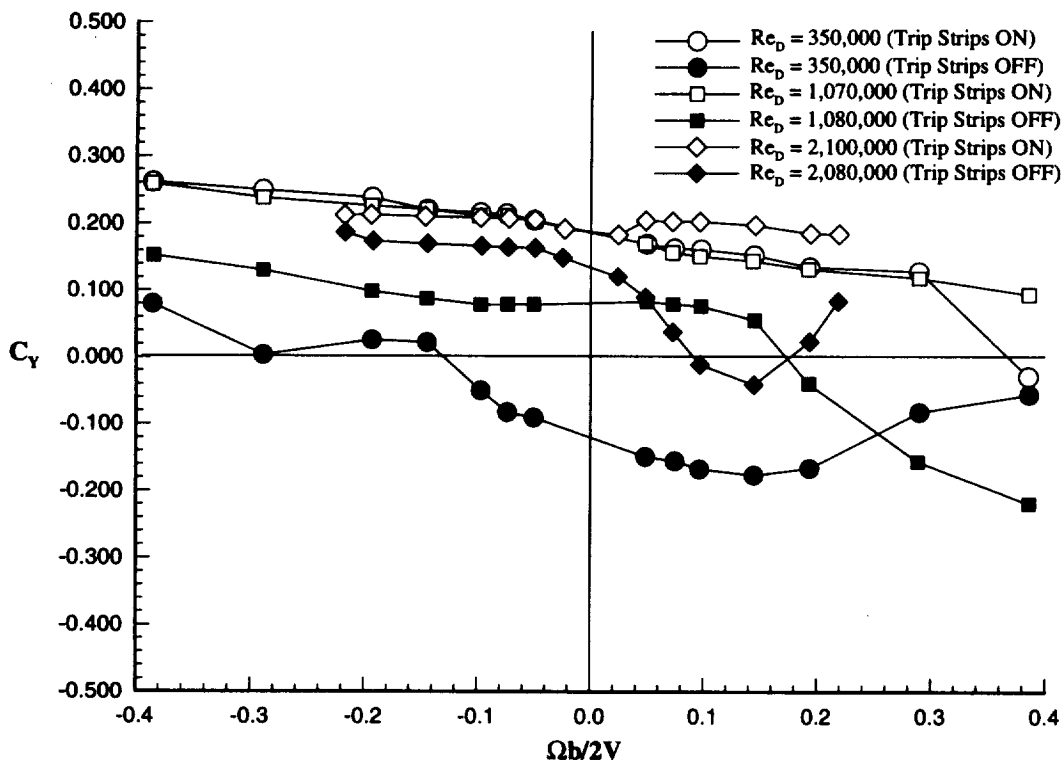
b) Side Force

Figure 38. Effect of trip strips on rotational aerodynamic characteristics at selected Reynolds numbers for the circular ogive at 60° angle of attack

Figure 39. Effect of trip strips on forebody pressure distribution at selected Reynolds numbers for the circular ogive at 60° angle of attack and $\Omega b/2V=0.0$.
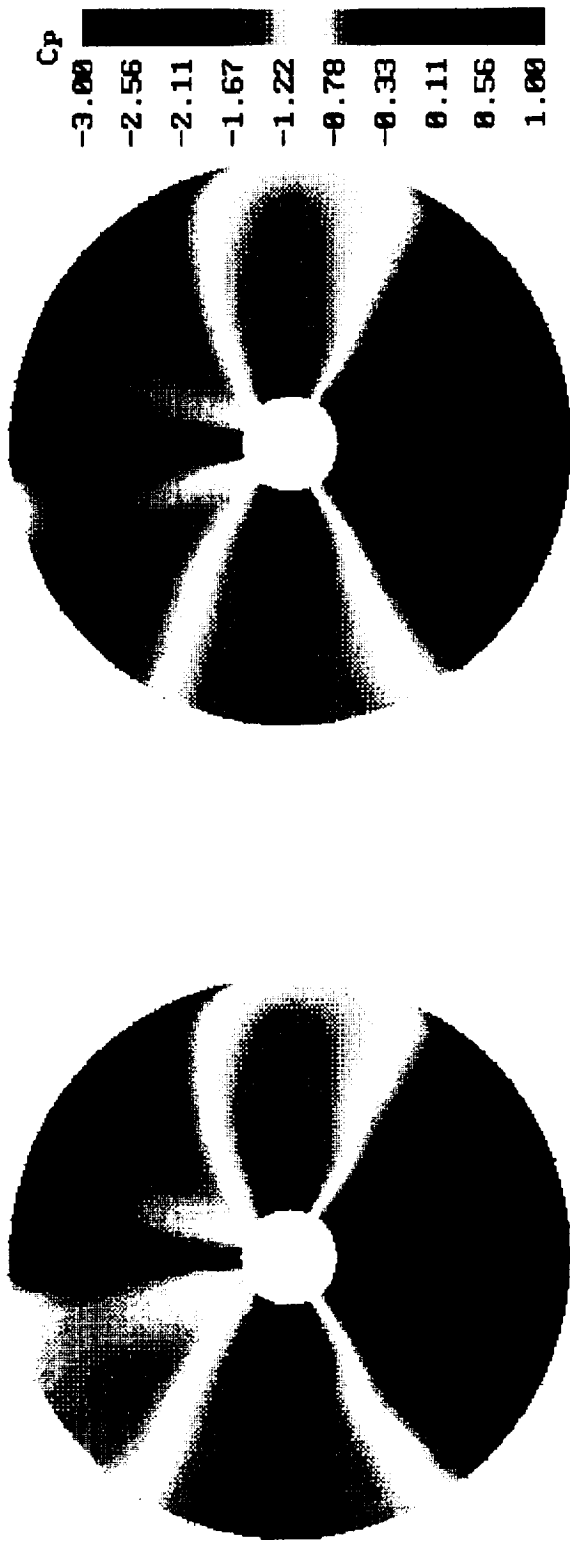
a) $Re_D = 350,000$

b) $Re_D = 700,000$

c) $Re_D = 1,070,000$

d) $Re_D = 2,100,000$
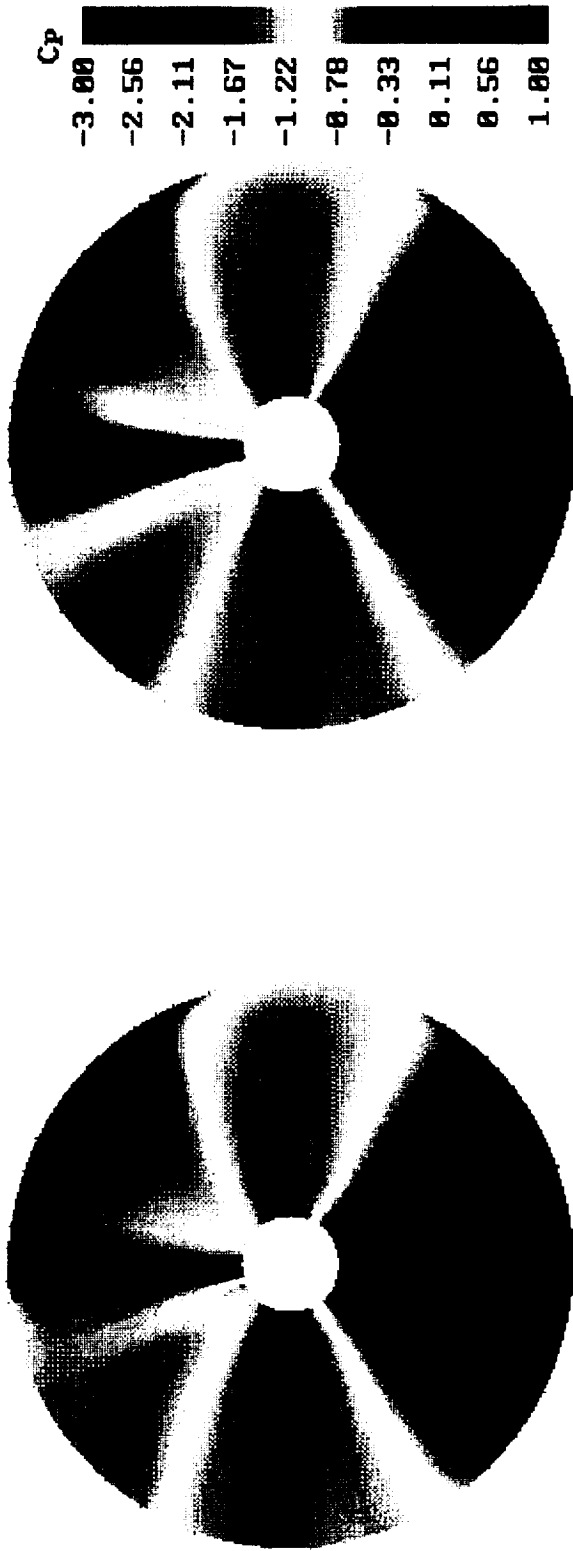
b) $\Omega b/2V = -0.1$

d) $\Omega b/2V = +0.1$

a) $\Omega b/2V = 0.0$

c) $\Omega b/2V = -0.2$

Figure 40. Effect of rotation rate on forebody pressure distribution for the circular ogive at 60° angle of attack with trip strips at $Re_D = 2,100,000$.
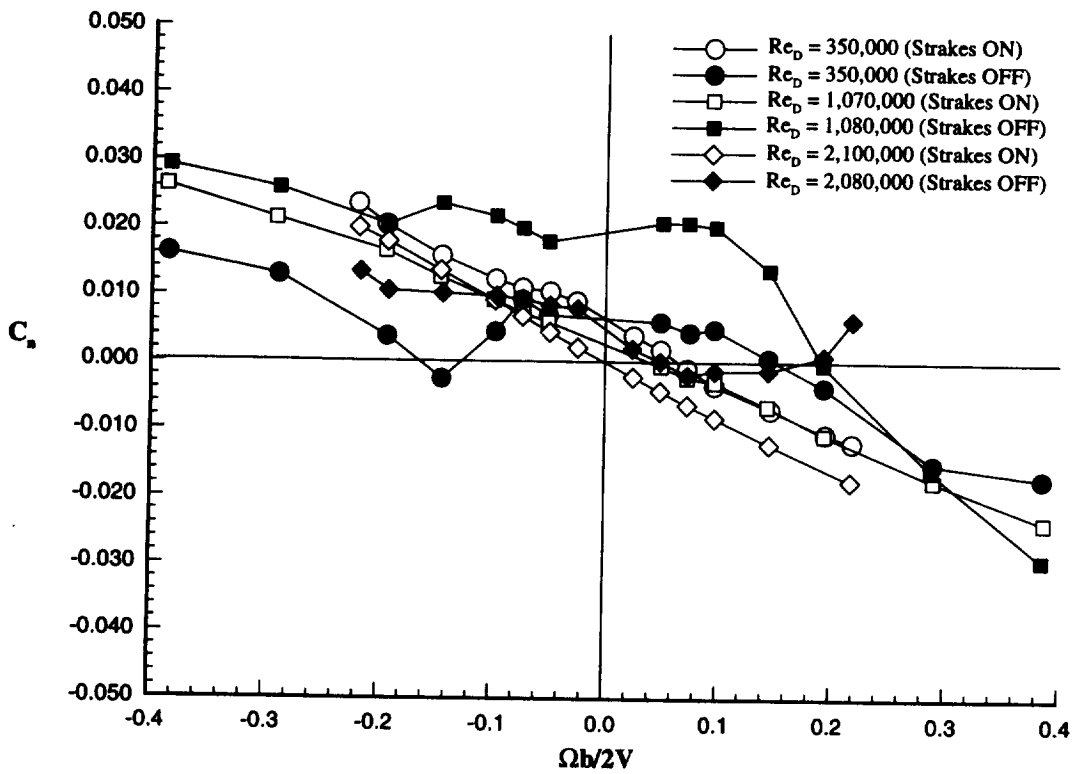
a) Yawing moment

Figure 41. Effect of forebody strakes on rotational aerodynamic characteristics at selected Reynolds numbers for the circular ogive at 60° angle of attack
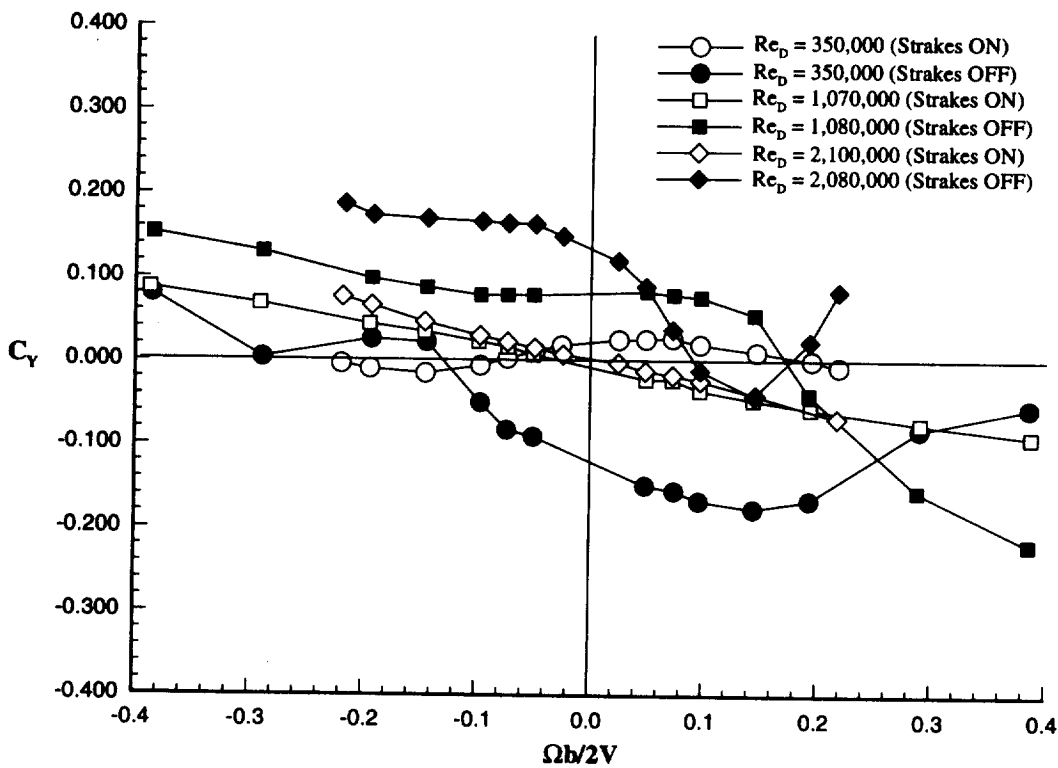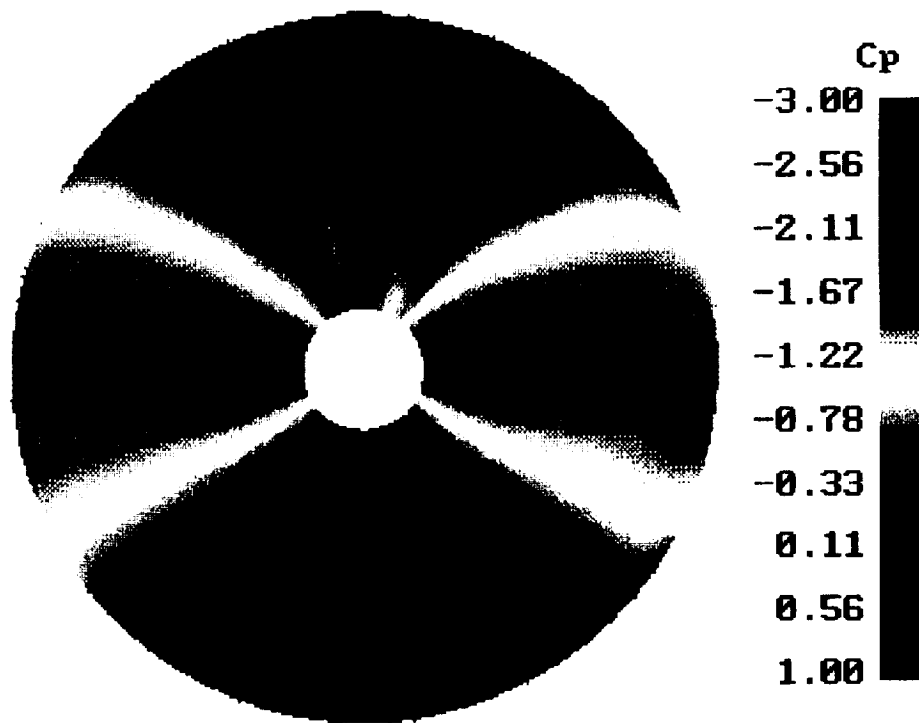

b) Side Force

Figure 41. Effect of forebody strakes on rotational aerodynamic characteristics at selected Reynolds numbers for the circular ogive at 60° angle of attack
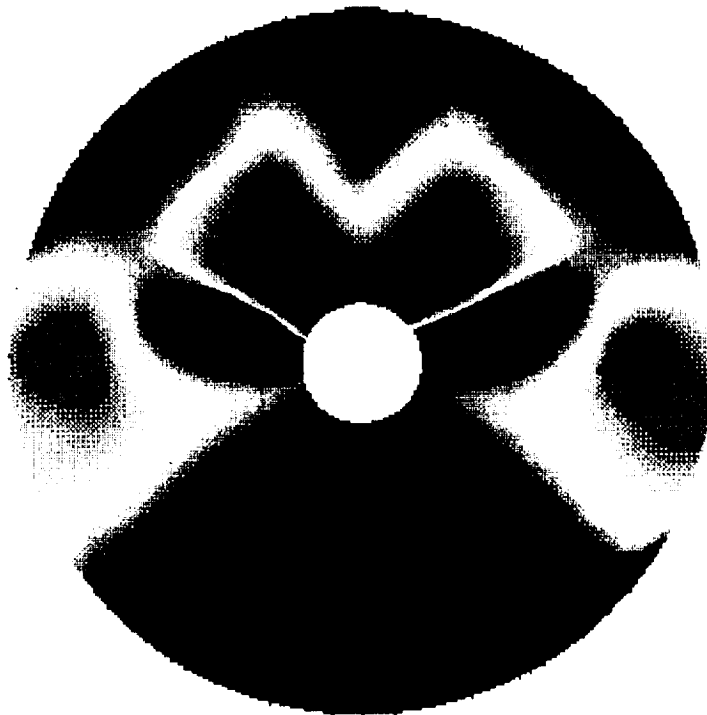
b) $Re_D = 700,000$

d) $Re_D = 2,100,000$

a) $Re_D = 350,000$

c) $Re_D = 1,100,000$

Figure 42. Effect of forebody strakes on forebody pressure distribution at selected Reynolds numbers for the circular ogive at 60° angle of attack and $\Omega b/2V = 0.0$.
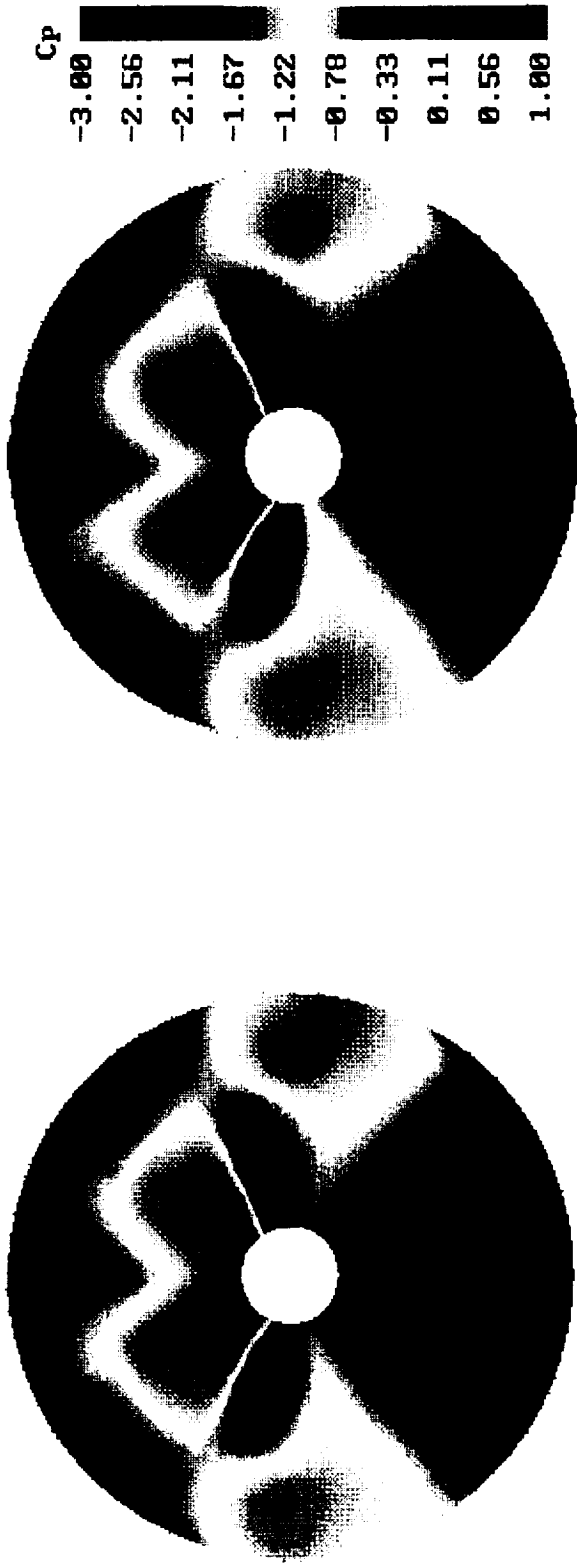
a) Strake off

b) Strake on

Figure 43. Comparison of forebody strakes on and off on forebody pressure distribution for the circular ogive at 60° angle of attack at $Re_D = 2,100,000$.
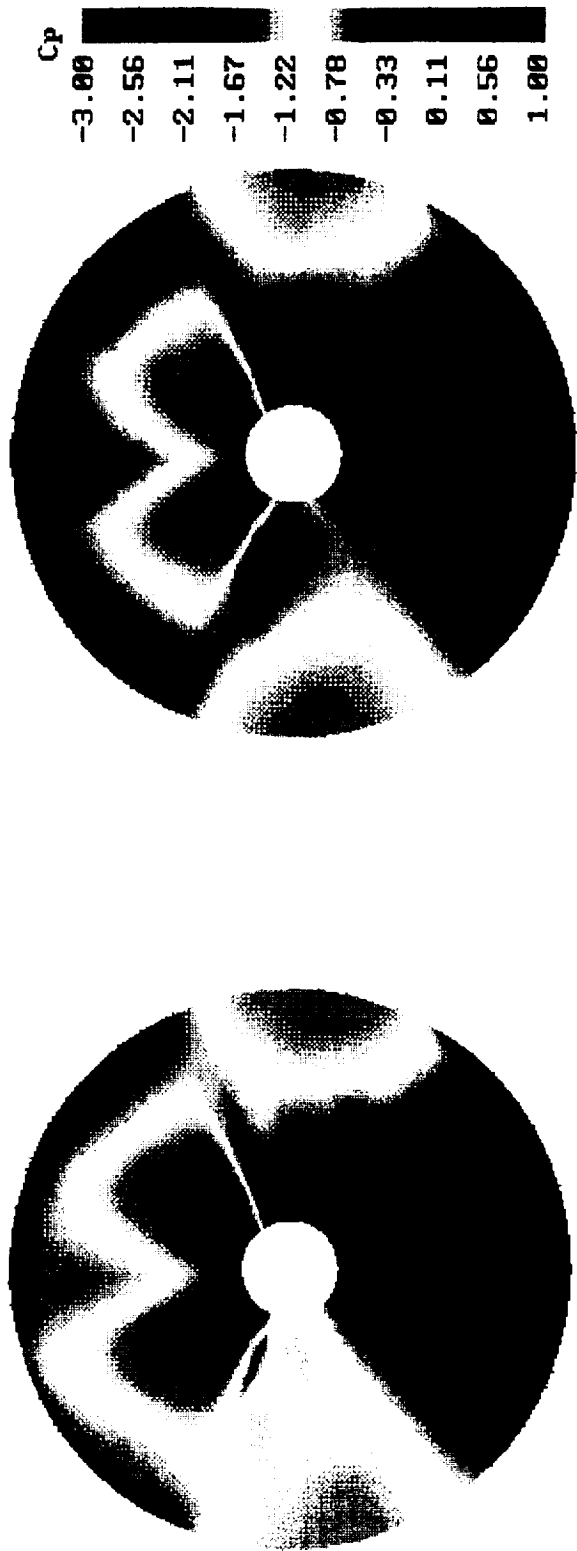
Figure 44. Effect of rotation rate on forebody pressure distribution for the circular ogive at 60° angle of attack with forebody strakes at $Re_D = 2,100,000$.
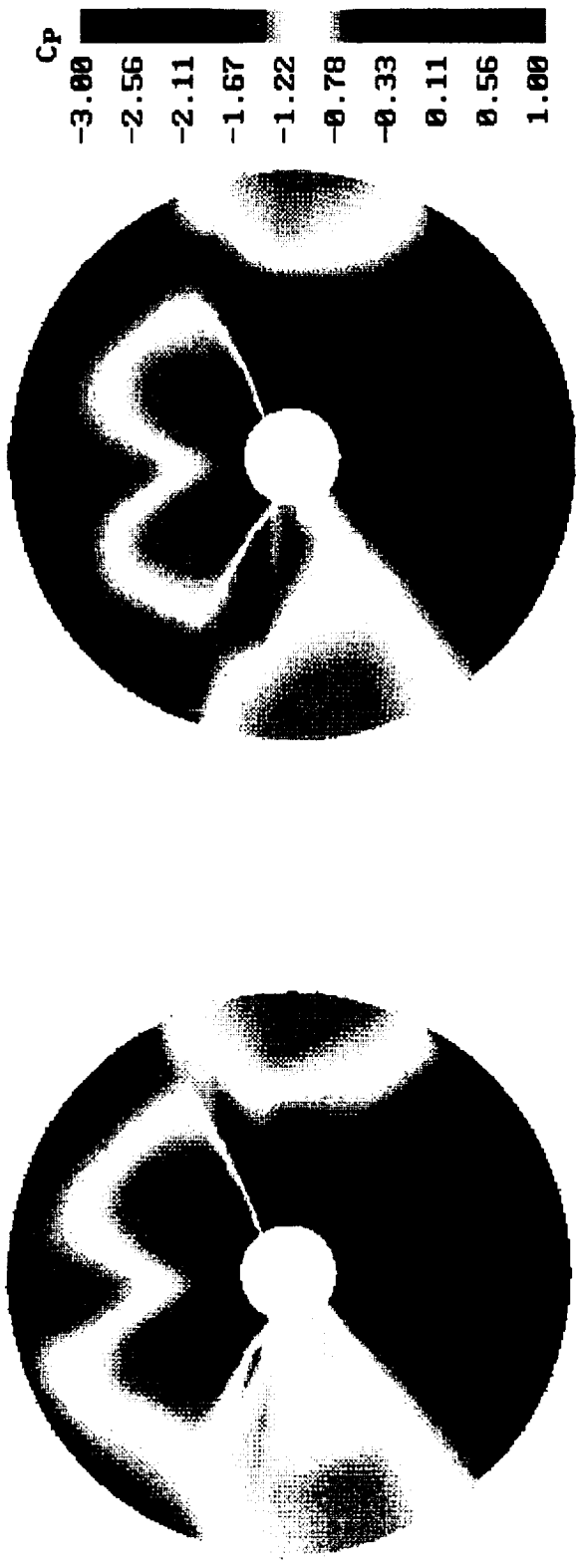
a) $\Omega b/2V = 0.0$

b) $\Omega b/2V = -0.1$

c) $\Omega b/2V = -0.2$

d) $\Omega b/2V = +0.1$

b) $Re_D = 700,000$

d) $Re_D = 2,100,000$

a) $Re_D = 350,000$

c) $Re_D = 1,100,000$

Figure 45. Effect of forebody strakes on forebody pressure distribution at selected Reynolds numbers for the circular ogive at 60° angle of attack and $\Omega b/2V = -0.1$.

b) $Re_D = 700{,}000$

d) $Re_D = 2{,}100{,}000$

a) $Re_D = 350{,}000$

c) $Re_D = 1{,}100{,}000$

Figure 46. Effect of forebody strakes on forebody pressure distribution at selected Reynolds numbers for the circular ogive at 60° angle of attack and $\Omega b/2V = -0.2$.

REPORT DOCUMENTATION PAGE

Form Approved
OMB No. 0704-0188

1. AGENCY USE ONLY *(Leave blank)*	2. REPORT DATE January 1995	3. REPORT TYPE AND DATES COVERED Contractor Report

4. TITLE AND SUBTITLE

EXPERIMENTAL STUDY OF THE EFFECTS OF REYNOLDS NUMBER
ON HIGH ANGLE OF ATTACK AERODYNAMIC CHARACTERISTICS OF
FOREBODIES DURING ROTARY MOTION

5. FUNDING NUMBERS

505-68-30-01

NAS1-20228

6. AUTHOR(S)

H. Pauley, J. Ralston, and E. Dickes

7. PERFORMING ORGANIZATION NAME(S) AND ADDRESS(ES)

Bihrle Applied Research, Inc.
18 Research Drive
Hampton, VA 23666

8. PERFORMING ORGANIZATION REPORT NUMBER

BAR 94-4

9. SPONSORING / MONITORING AGENCY NAME(S) AND ADDRESS(ES)

National Aeronautics and Space Administration
Langley Research Center
Hampton, VA 23681-0001

10. SPONSORING / MONITORING AGENCY REPORT NUMBER

NASA CR-195033

11. SUPPLEMENTARY NOTES

Langley Technical Monitor: Raymond D. Whipple
Final Report

12a. DISTRIBUTION / AVAILABILITY STATEMENT

Unclassified - Unlimited
Subject Category 02

Availability: NASA CASI, (301) 621-0390

12b. DISTRIBUTION CODE

13. ABSTRACT *(Maximum 200 words)*

The National Aeronautics and Space Administration in the United States and the Defense Research Agency in the United Kingdom have ongoing experimental research programs in rotary-flow aerodynamics. A cooperative effort between the two agencies is currently underway to collect an extensive database for the development of high angle of attack computational methods to predict the effects of Reynolds number on the forebody flowfield at dynamic conditions, as well as to study the use of low Reynolds number data for the evaluation of high Reynolds number characteristics. Rotary balance experiments, including force and moment and surface pressure measurements, were conducted on circular and rectangular aftbodies with hemispherical and ogive noses at the Bedford and Farnborough wind tunnel facilities in the United Kingdom. The bodies were tested at 60° and 90° angle of attack for a wide range of Reynolds numbers in order to observe the effects of laminar, transitional, and turbulent flow separation on the forebody characteristics when rolling about the velocity vector.

14. SUBJECT TERMS

High angle of attack; Reynolds number effects; rotary derivatives; pressure data

15. NUMBER OF PAGES

98

16. PRICE CODE

A05

17. SECURITY CLASSIFICATION OF REPORT Unclassified	18. SECURITY CLASSIFICATION OF THIS PAGE Unclassified	19. SECURITY CLASSIFICATION OF ABSTRACT	20. LIMITATION OF ABSTRACT

NSN 7540-01-280-5500

Standard Form 298 (Rev. 2-89)
Prescribed by ANSI Std. Z39-18
298-102